Development and characterisation of silicon microfluidic components and systems

PhD Thesis

Zoltán Fekete

Supervisor: Péter Fürjes, PhD

MEMS Lab, Institute for Technical Physics and Materials Science
Research Centre for Natural Sciences, Hungarian Academy of Sciences,
MTA TTK MFA

2012

Content

1. Preface

1.1 Motivation and goals

Recently, the role of microfluidics in biomedicines is steadily increasing. Due to latest progress in micro- and nanotechnology potential clinical applications are expected to be fulfilled in the near future. In my work, microfluidic research focuses on the areas of neuroscience and medical diagnostics, where my investigation on both microfabrication and physical principles can further improve reliable design of microcomponents and devices in these promising fields.

Neuroprosthetics

By aging of the society, brain-related clinical cases like paralysis, epillepsy or Parkinson diseases are remarkably increasing acting as critical issues to be solved for today medicine. Medical attendance and rehabilitation of such diseases is very challenging for both patients and their relatives. The aim of modern neurophysiology is to improve their quality of life. Processing of signals generated by brain neurons is of great importance in neurophysiology, since a large amount of information can be gained about the dynamics of the nervous system and the relationship between brain and motor function activity [1.1]. As a result of efforts in this field, a wide range of structural material like silicon has been used to fabricate probes, which is applicable to record the activity of brain cells in non-human experiments extending our knowledge about the above issues.

Researchers have used pharmacologic intervention (e.g. systematic injection) anti-inflammatory agents can be transported via microfluidic systems into the tissue around the microprobes, and noticed that the response of neighbouring cells and neural tissues changed. Drug delivery in acute experiments can be easily implemented, however, during chronic implantation, the local injection of drugs is more critical. The advantages of the latter is that smaller amount of biological sample is necessary, cells can be directly excited, while peripheral metabolism and the reactive response of neural tissue is excluded increasing the long-term stability of the device [1.2].

My goal in the field of neural microdevices was to design and realise multi-functional microprobes integrating a parallel system of electric sensing or excitation and local drug delivery functions into a single substrate. Since the characterisation of the mechanical and fluidic properties of microprobes fabricated by the proposed technology are essential for future application, and a number of in vivo experiments has been carried out to evaluate microprobe performance.

Diagnostics of blood

Currently, cardiovascular diseases are among the leading reasons of casualties worldwide. Almost every third fatal occasion originates from such illnesses. Fast diagnostics are essential to anticipate the deterioration of several diseases. Therefore, the research and development of microanalytical systems (Lab-on-a-chip, µTAS – micro-Total-Analysis-System) are increasingly heading toward the downscaling and cost-effective fabrication of today's medical microdevices [1.3]. Such systems are able

to complete complex analytical tasks or perform personalized diagnosis that demanded the presence of serious hardware or professional personnel before. In the microscale not only the adaptation of analytical principles means great challenge, but the transport and preparation of biological samples are still relevant issues. Since hydrodynamic phenomena are often different than in the macroscopic world, the solution of sample manipulation (extraction, dilution, separation, and transport to the active region) is a great challenge for microengineers of micro- and nanofluidic systems [1.4].

The aim of the vast majority of clinical tests is the detection of the presence and quantity of several proteins, ions, crystalloids or diluted gas in blood plasma. Since the cell components of blood are not desired during measurements, the first step is removing these particles from the blood plasma. If the measurements are to be embedded in a microsystem, the integration of separation is important [1.5].

The presence of proteins can be efficiently identified by solid-state nanopore membranes as sensing elements. Nanopore sensing is an extremely sensitive analytical method due to the nanoscale pore geometry (shape and surfaces), which makes the interactions between pore surface and molecules of analytes to contribute to the control of ion or molecule transport [1.6]. The detection principle is based on the selective interaction of pores and the analysed component which reduces the permeability of nanopores for the measured marker ions or molecules, and therefore produces a flux change equivalent to the analytical signal. Sensitivity is outstanding, since extremely small immobilized component causes apparent modulation in ion or molecule flux.

My goal in the field of diagnostics of cardiovascular diseases was to design and realise a silicon based microfluidic system, which contains the functions of sample preparation as well as the sensing element. To prepare whole blood, plasma separation and dilution has to be optimized in the microscale and the integration of a detection unit highly sensitive to blood proteins has to be implemented in a single microsystem. This way a rapid diagnosis can be set up in the case of diseases demanding fast intervention (e.g. stroke) in situ [1.7].

1.2 Structure of dissertation

In my thesis, I will give a deeper insight into novel scientific results in microfluidics and related issues. I achieved my work in the MEMS Laboratory of the Institute for Technical Physics and Material Science. This PhD thesis is organized as follows.

In Chapter 2, I introduce the reader to the background of my motivation in the fields of neural implants and Lab-on-a-chip systems.

Chapter 3 contains a brief description on state-of-the-art fabrication principles and technology in microengineering sciences. A general overview of literature on the advanced technologies of silicon based microfluidic components and devices support a better comprehension of following chapters on microfabrication.

In Chapter 4, my proposed fabrication technology and integration of sealed microfluidic channels in silicon into silicon probes are presented, followed by fluidic and mechanical characterisation of the realised microprobes.

In Chapter 5, the principle, characterisation and optimization of a microfluidic sample preparation function is described, and integration concept into Lab-on-a-chip devices is presented.

2. Microfluidics and biomedical applications

2.1 Introduction to microfluidics

By definition microfluidics is the science and engineering of systems in which fluid behaviour differs from conventional flow theory primarily due to the small dimensions of the system. According to other explanations, microfluidics generally deals with the behaviour, precise control and manipulation of fluids that are geometrically constrained to a small, typically sub-millimetre scale. Microfluidics is undoubtedly a multidisciplinary field intersecting engineering, physics, chemistry, microtechnology and biotechnology, with practical applications to the design of systems in which such small volumes of fluids will be used. Microfluidics emerged in the beginning of the 1980s and is used in the development of inkjet print heads, DNA chips etc. Besides small device size, in this regime typical system parameters results in smaller volume of fluids to be handled and lower energy consumption is needed, however, the physical effects typical of the micro domain emerges and should be considered during the design of individual components. Most of the applications include passive microfluidic control like capillary forces, while a number of other devices are equipped external or integrated actuators (e.g. microvalves and micropumps) for providing fluid transport. Latter ones are called active microfluidic systems.

Microfluidic components and systems have several advantages which are attributed to miniaturization:

- Small volume of analyte is necessary
- Speed of reaction is increased
- Precise manipulation (mixing, separation, heating etc) is available
- Other devices can be integrated (Lab-on-a-chip - LOC)
- Disposable assays and cartridges can be used
- Cost of reagents are reduced
- High surface to volume ratio
- Dead volume s minimized
- More parameters can be monitored simultaneously

As mentioned above, micro level brings dramatic changes in the impact of several physical effects [1.8]. Analyzing the physical properties of microsystems is expressive if the concept of scaling laws is applied. A scaling law describes the variation of physical quantities with the size of the given system or object, while keeping other quantities such as time, pressure, temperature, etc. constant. As an example, consider volume forces, such as gravity and inertia, and surface forces, such as surface tension and viscosity. The basic scaling law for the ratio of these two classes of forces can generally be expressed by

$$\frac{F_{surface}}{F_{volume}} \propto \frac{l^2}{l^3} = \frac{1}{l} \xrightarrow[l \to 0]{} \infty \qquad (2.1)$$

This scaling law implies that when scaling down to the microscale in lab-on-a-chip systems, the volume forces, which are very prominent in our daily life, become largely unimportant.

At the microscale some other interesting and sometimes unintuitive properties also appear. In particular, the Reynolds number, which described in more details in Chapter 4.4.1., can become very low. A key consequence of this is that fluid flow is generally laminar, and do not necessarily mix in the traditional sense (see Fig. 2.1); molecular transport happens often through diffusion. High specificity of chemical and physical properties (concentration, pH, temperature, shear force, etc.) can also be ensured resulting in more uniform reaction conditions and higher grade products in single and multi-step reactions.
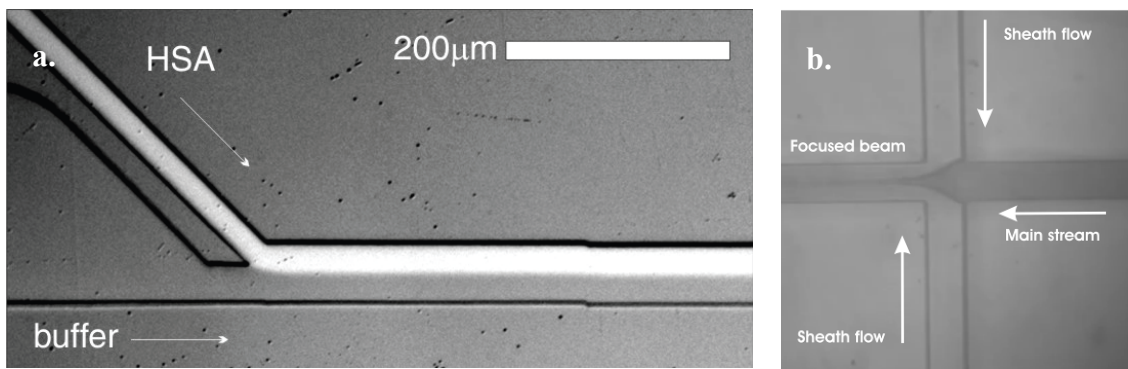
Figure 2.1: Laminar flow of water (buffer) and fluorescently labelled human serum albumine (HSA) in a T-type micromixer (a.) and hydrodynamic particle focusing with three flow stream (b.) produced in the MEMS Lab of TTK MTA MFA.

The basis of most LOC fabrication process is photolithography. Initially most of the processes are in silicon, as these well-developed technologies are directly derived from semiconductor fabrication. Because of demands for e.g. specific optical characteristics, bio- or chemical compatibility, lower production costs and faster prototyping, new processes have been developed such as glass, ceramics and metal etching, deposition and bonding, polydimethylsiloxane (PDMS) and SU-8 processing (e.g., soft lithography - see Fig. 2.2), thick-film- and stereolithography as well as fast replication methods via electroplating, injection moulding and embossing. Furthermore the LOC field more and more exceeds the borders between lithography-based microsystem technology, nanotechnology and precision engineering. My work focuses on some highlights of silicon based microfabrication.
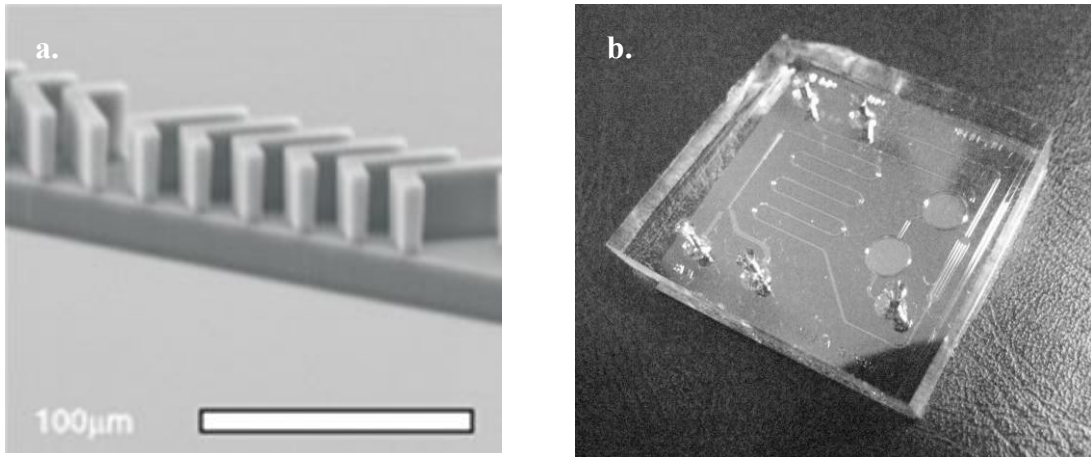
Figure 2.2: Moulding form in SU-8 for Rapid Prototyping (a.) and moulded PDMS based Lab-on-a-chip (b.) produced in the MEMS Lab of TTK MTA MFA.

2.2 Drug delivery in neural applications

The development of pharmacological functions in neural applications is definitely inspired by Deep Brain Stimulation (DBS) techniques [2.1]. Since blood-brain barrier is not penetrable for most proteins, localised delivery of e.g. growth factors is preferred.

The idea of treating neurologic disorders with chronic stimulation began to emerge in the 1960s, but stimulation was largely used for targeting surgical lesions. At the end of 1960s a method of chronic implantation of a bundle of multiple electrode wires deep in the brain was developed. The goal of the stimulation was to delineate the "best" target for a subsequent lesion. Although the goal was initially the lesion guidance only, the period of chronically implanted electrodes started. Since then, DBS has become increasingly used for treating a variety of disorders. As a result of progress in the field of microengineering, implantable neural electrodes with the ability of simultaneous chemical stimulation and electrical recording have been fabricated and applied. They offer interesting perspectives for a variety of common and severe health problems e.g. hearing loss [2.2], chronic pain [2.1, 2.3], essential tremor [2.1], Parkinson [2.1] diabetes [2.3], Alzheimer [2.4], depression [2.5] or epilepsy [2.6]. Simultaneous chemical and electric interactions with the very same groups of cells of an active brain might induce a huge progress in these studies. Moreover, the long-term stability of electrophysiological implants is to be enhanced. With the help of continuous dosage of anti-inflammatory drugs, delaying or reducing the response of the surrounding tissue might be also possible [2.7-2.8]. Currently, the development of microsystems for neural application focuses on the solution of the above issues to maintain the dynamics of progress in this discipline.

As far as the implantation apparatus is concerned, wire electrodes for recording and stimulation of electrical signals [2.9] as well as glass or steel capillaries used to deliver pharmaceutical substances directly into the brain [2.10] are the established tools in neuroscience research. However, the rapid development of micro-electromechanical systems (MEMS) within the last decades has opened completely new technological perspectives with respect to system integration of advanced functions [2.11]. A detailed description of recent progress on microprobe technology is presented in Chapter 4.

The application and optimization of microfluidic principles in neural drug delivery system is still in its infancy. Novel techniques could take further roles in biomedical devices, if their comprehensive characterisation took place after preliminary demonstrations. The mission of microtechnology regarding neural implants is now to review, optimize and integrate the latest developments of microfluidic researches in order to make reliable and efficient physiological and pharmacological measurements through neural implants. My aim is to develop and optimize a microchannel fabrication technology and integrate it into a neural microprobe. Since the fluidic and mechanical performance of a hollow microprobe is significantly affected by the integrated channel system, these issues are also addressed experimentally in later chapters.

2.3 Sample preparation in microfluidic systems

The entire volume of human blood is recirculated throughout the body in every minute. It delivers oxygen and nutrients to every cell and transports products from and toward tissues. During this recirculation, cells of the immune system are also transported quickly and efficiently through blood performing specific immuno-surveillance functions where necessary. As a result, blood can give large amount of information on the actual state of all tissues and organs. This implies that blood sampling and analysis are of great interest for both medical and science applications, and hold a central role in the diagnosis of many physiologic and pathologic conditions.

Progress in technology facilitated several breakthroughs in extending our knowledge on biology and inherently blood itself [2.12]. Advances in microscopy by the seventeenth century allowed the observation of individual cells in blood. Later, in the nineteenth century, the development of tissue-staining techniques facilitated the characterisation of the first blood cell populations. The most common and yet the most informative examination in haematology is performed by Wright-Giemsa staining procedures and full blood count [2.13]. Staining procedures utilize histological stain that facilitates the differentiation of several blood cell types, while counting methods are based on flow cytometry techniques.

Flow cytometry techniques represent nowadays the golden standard in cell identification and separation producing finer details and higher throughput than previous techniques. However, as complexity of these latest techniques is getting higher, they require increasingly higher levels of skill of users. The analysis of the cellular component in particular has been affected by restricting it to highly specialized and strictly regulated laboratories, to the detriment of point-of-care diagnostic tools. In spite of strict regulations, a large number of blood handling is still performed manually, even in relatively well automated laboratories, or in conditions that may significantly alter the results of subsequent analysis. Efforts to reduce the chance for emerging errors, to reduce time blood is exposed from collection until analysis and to increase availability of state-of-the-art analysis techniques on the premises and at low cost requires a completely new approaches.

As new technologies emerge in biological applications, microfluidics and microscale lab-on-a-chip-type devices are getting into the focus of blood analysis development [2.14]. Availability of health care and diagnostics at the bedside is often referred to as point-of-care testing (POCT). Through POCT analysers clinical diagnostics will certainly be revolutionalised. New devices for convenient use at home or in doctors' offices would allow for rapid and accurate diagnostic and prognostic, based on blood cells, of infectious diseases, cancers, and inflammatory responses. As a

result, a better matching between drugs and patient pathophysiology is expected, reducing side effects and improving efficiency of therapy.

In the field of drug discovery, microfluidic devices can redefine the entrance criteria for clinical trials and examine for these criteria sparing time and costs. Moreover, microfabricated devices for sample preparation would open up new possibilities by facilitating comprehensive genomic and proteomic analysis from even small homogenous subpopulations down to single cells. Generally, blood sample preparation in lab-on-a-chip systems may result more gentle, fast, and consistent manipulation of living cells, and therefore produce better quality of gained information.

Due to the rapid development of microfabrication principles, a large number of manipulation technique come to exist, however, only a few of them has been extensively characterised regarding performance, feasibility or possible integration into lab-on-a-chip systems. My aim is to provide a deeper insight into blood plasma separation techniques, and describe the experimental characterisation and optimization of the so-called Zweifach-Fung particle separation method, which will be explained in details in Chapter 5.

2.4   Blood as sample analyte

In this section, I give a brief overview on the physical properties of blood, focusing on characteristic phenomena essential to have knowledge of in order to see the issues during manipulation of blood.

Composition of blood

Approximately eight percent of the total weight of human body is composed of blood. Its average density is 1060kg/m^3 and dynamic viscosity is 0.005Pas, which is very close to that of water (1000kg/m^3 and 0.001Pas respectively). An adult person generally has a volume of blood of 5l, which eventually the mixture of plasma, proteins, lipids and several cell components. Traditionally the separation of plasma from cells takes place by centrifuging. This way, the produced plasma consists of 90% water, 7% plasma proteins, 2% organic and 1% inorganic materials. Cell components are mainly erythrocytes or red blood cells (RBC), leukocytes or white blood cells (WBC), and thrombocytes or platelets (see Fig. 2.3). White blood cells responsible for immunological mechanisms and platelets responsible for thrombosis constitutes only 1/600 and 1/800 part of the whole cell quantity respectively. RBC constitutes almost 45-50% of whole volume of blood. Approximately, there is 5*10^6 RBC per mm^3. Besides, the average number of WBC is 5-8 thousand per mm^3, while the number of platelets is between 250-300 thousands per mm^3.
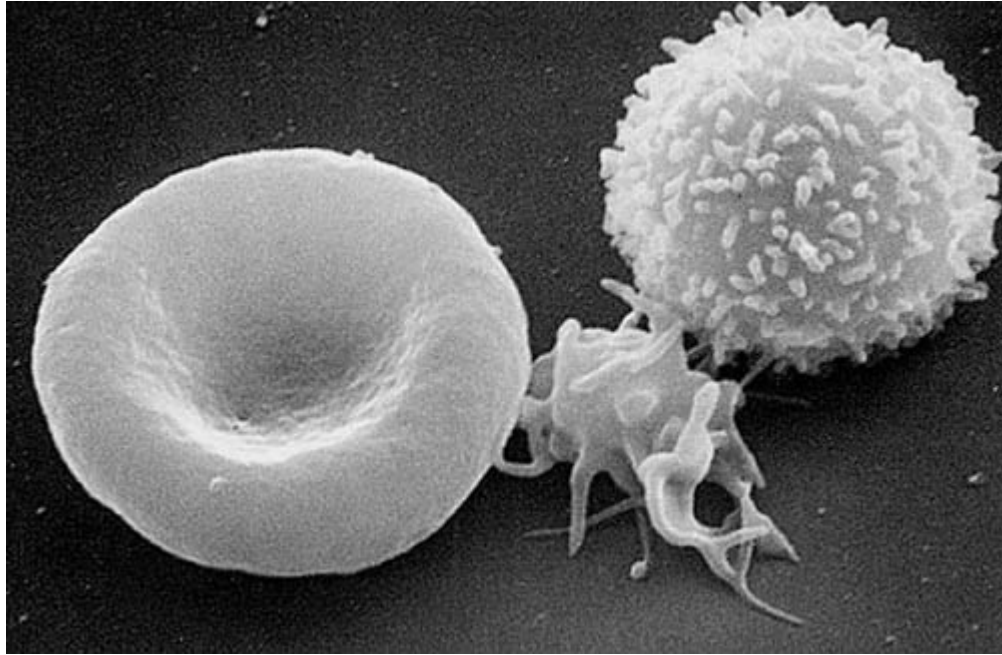
Figure 2.3: A three-dimensional ultrastructural SEM image of a T-lymphocyte (right), a platelet (centre) and a red blood cell (left) made in The National Cancer Institute at Frederick.

Characteristic hydrodynamic and rheological properties of blood can attributed to RBC because of their dominant presence in whole blood. RBC can be considered as biconcave discs. Their diameter is around 7-8μm, their thickness is ~3μm at the circumference and 1μm at the centre. This special biconcave shape is responsible for the little change in surface area even during considerable deformations.

Dilution of blood

Particle concentrations of blood samples are often referred as haematocrit value, which is the volumetric density of RBC. The average haematocrit value is 40-52% and 35-47% in case of adult men and women respectively.

In case of blood samples at rest, RBCs and platelets start to coagulate. This mechanism is called as thrombosis, which is caused by fibrinogen proteins in blood plasma. Since coagulation is an unwanted phenomenon during rheological experiments, blood samples are generally diluted by heparin, EDTA or citrate in order to avoid thrombotic reaction. This way the natural composition of blood is inherently modified, therefore it is essential to carry out blood separation and analysis as fast as possible.

J Zhang et. al. [2.15] have tested how the haematocrit value affects the separation efficiency (more detailed in Chapter 5). Their results are shown in Fig. 2.4. They proposed that separation efficiency increases significantly at low haematocrit value; therefore a preliminary dilution is recommended and eventually used in my experiments.
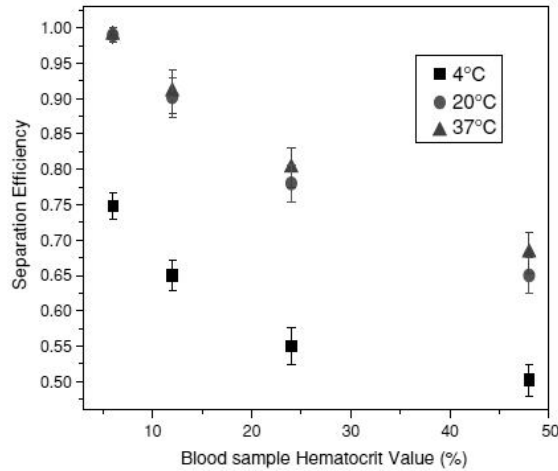
Figure 2.4: Separation efficiency plotted against the sample haematocrit value [2.15]

Viscosity of blood

Fluids, in which the relationship between velocity gradients and shear forces is directly proportional, are called Newtonian fluids. Because of its hydrodynamic properties, blood plasma is also considered as Newtonian fluid [2.16]. However, cells definitely increase blood viscosity (see Fig. 2.5), which depends on flow velocity, microchannel cross-section parameters, density of cells and temperature as well. Whole blood (plasma and cells altogether) therefore shows non-Newtonian behaviour, which finally contributes the easier flow through small capillaries or vessels than plasma itself.
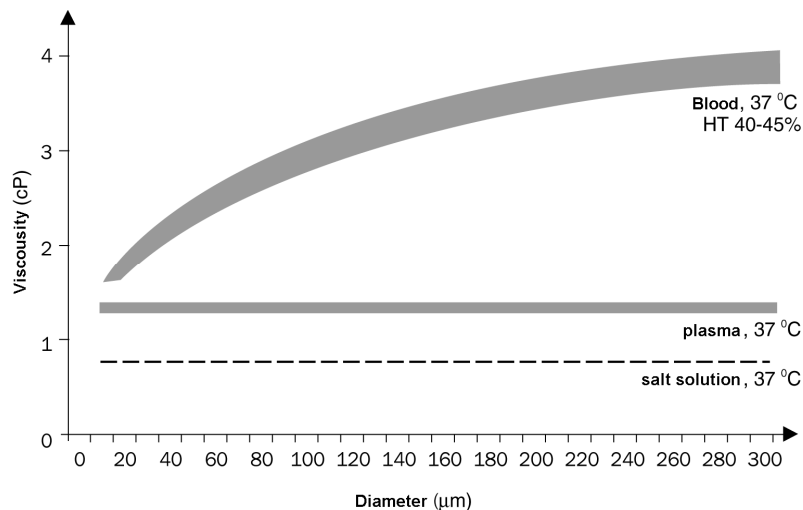

Figure 2.5: The diagram shows the relationship between capillary diameter (x-axis) and viscosity (y-axis). It is clear that at low haematocrit value almost no change in viscosity can be noticed when the tube diameter decreases.

As it is illustrated on Fig. 2.5, blood viscosity is also influenced by microcapillary geometry (e.g. tube diameter). In small capillaries viscosity decreases significantly when decreasing tube diameter. In literature this phenomenon is also referred as Fahraeus-Lindqvist effect.

11

In the case of small deformations, blood viscosity is constant. When increasing shear velocity (gradient of flow velocity), viscosity is decreasing until a constant plateau is reached. Materials are called pseudoelastic, if increasing deformation causes lower viscosity. This property is triggered by the presence of RBC and physical explanation is based on their flexibility and orientation in flow direction.

Haemolysis

Cells cannot be exposed to arbitrary shear forces, since above a critical value cell membrane is damaged, and intracellular content can enter the plasma. This so-called haemolysis is a negative effect in experiments. Cytoplasm alters the composition and ion concentration of blood plasma. Additionally, such proteins can get into blood flow that is usually observed in the plasma only in diseased cases. This way an artefact in analytical measurements can be present. By a precise design of device operation parameters, haemolysis can be avoided. Fig. 2.6 shows the haemolysis index (derived from photometric plasma-haemoglobin measurements) plotted against shear stress and exposition time. Exposition time is the period of time until the cells were exposed to a certain shear load. Damage of RBC is negligible in a wide range, however in case of $\tau <$ 425Pa and $t_{exp} > 620$ms, it can be significant [2.17]. Microchannel sizing and initial flow velocity of blood should be chosen such that shear stresses stay below these experimentally defined critical values.
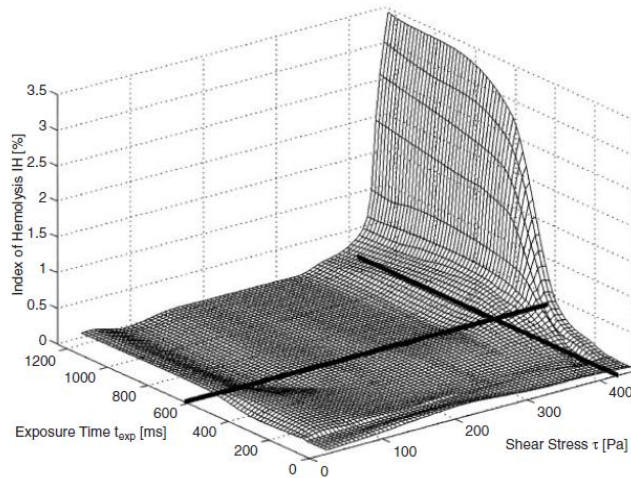
Figure 2.6: Haemolysis index plotted against shear stress and exposition time [2.17].

3. Fabrication of silicon microfluidic systems

3.1 Introduction to MEMS technology

MEMS (Micro-electro-mechanical systems) are referred as integrated devices or systems that combine electrical and mechanical components. They range in size from the submicrometre level to the millimetre level. The construction of MEMS devices extends the fabrication techniques developed for the integrated circuit industry to add mechanical elements such as beams, gears, diaphragms and springs to devices.

The three characteristic features of MEMS fabrication technologies are miniaturization, multiplicity and microelectronics. Miniaturization enables the production of compact and rugged devices with quick response times. Multiplicity refers to the batch fabrication inherent in semiconductor processing which allows thousands or millions of components to be easily and concurrently fabricated. Microelectronics provides the intelligence to MEMS and allows the monolithic merging of sensors, actuators and analogue circuitry to build closed-loop feedback components and systems. IC fabrication technology or microfabrication has so far been the primary enabling technology for the development of MEMS. Advances in IC technology in the last decade have brought corresponding progress in the MEMS fabrication processes. Manufacturing processes allow for the monolithic integration of MEMS structures with driving, controlling and signal processing electronics. This integration promises to improve the performance of micromechanical devices as well. The primary enabling technology for the development of MEMS is based on IC fabrication technology or microfabrication.

The major steps in IC fabrication technology are film growth, doping, lithography, etching, wafer bonding, dicing, and packaging.

- Film growth: Usually, a polished Si wafer is used as the substrate, on which a thin film is grown. The film, which may be epitaxial Si, SiO_2, silicon nitride (Si_3N_4), polycrystalline Si (polysilicon), or metal, is used to build both active or passive components, masking, dielectric or passivation layers as well as conduction bands or interconnections between circuits.

- Doping can be used to modulate the physical properties of the device layer. Low and controllable level of an atomic impurity may be introduced into the layer by thermal diffusion or ion implantation, which is also useful as etch-stop layer for selective chemical etching of the substrate.

- Lithography: A pattern on a mask is transferred to the film by means of a photosensitive (i.e., light sensitive) chemical known as a photoresist. The process of pattern generation and transfer is called photolithography. A typical mask consists of a glass plate coated with patterned chromium (Cr) film and positioned above the wafer by mask aligning systems.

- Etching is the selective removal of unwanted regions of a film or substrate for pattern delineation. Wet chemical etching or dry etching may be used. Etch-mask materials are used at various stages in the removal process to selectively prevent those portions of the material from being etched. These materials include SiO_2, Si_3N_4 or hard-baked photoresist.

- Wafer bonding is applied to form closed microsystems by attaching silicon and/or glass substrates to one another.

- Dicing: The finished wafer is sawed or machined into small squares, or dice, from which individual microchips can be made.

- Packaging: The individual sections are then packaged, a process that involves physically locating, connecting, and protecting a device or component. MEMS design is strongly coupled to the packaging requirements, which in turn are dictated by the application environment. The concept of System-in-Package facilitates to integrate a wide range of functions into the same microcomponent as well.

A more detailed description of process steps of MEMS technology is presented in [3.1].

3.2 Role of MEMS technology in microfluidics

In the 1970s when integrated circuit technology has been adapted for the fabrication of physical sensors e.g. force or pressure sensors initiating the advent of MEMS era, there was no technical obstacles in making the first simple microfluidic systems as well. The first miniaturized gas chromatography system was realised around 1975 [3.2]. The proposed device circulated gas through microchannels etched in silicon and also contained electromagnetic injection as well as thermal detection, all on a single chip just a few centimetres wide. However, the needs of such developments have not been in the focus of those involved in silicon technology, therefore this achievement was individual attempt in that period [3.3]. Only at the beginning of the 1990s got the advantages of miniaturization into the spotlight. Once again all started with chromatography applications [3.4], and then all sorts of microfluidic systems began to be fabricated in a quick pace. Just a few examples from the many almost in chronological order were electrophoretic separation systems, [3.5], electroosmotic pumping systems [3.6], diffusive separation systems [3.7], micromixers [3.8], DNA amplifiers [3.9-3.10], cytometers [3.11], and chemical microreactors [3.12].

In parallel, microfluidics was being used to answer fundamental physical questions, e.g. first experiments involving the stretching of DNA [3.13] in 1993 and molecular level investigation has been triggered and lasts even today.

The first microfluidic products commercialized on a large scale were inkjet printer heads. By parallelizing ejection heads, droplet dispensers can also be constructed and can be successfully used for chemical or biological analyses. Droplet dispensers at this time constitute a substantial part of commercial activity in the field of microfluidics [3.14].

Today's microfluidics chips are produced by the millions for chemistry and biology. The advantage of these chips is that they allow a massive number of tests to be run in parallel, and also provide large amounts of data, which is essential to precisely characterise a product. This kind of development is inevitably in the search for new types of medical treatments.

Due to the relative ease and accessibility of many of silicon based technologies, it has become possible to integrate several elements on the same chip and to create Lab-

on-a-chip devices. The rapid expansion of the field of microfluidics seems to be driven in part by the possibility of integration. The ultimate goal is to be able to detect biological molecules, and transport, mix and characterize a raw sample, all with one device. In traditional genomic analyses, it was necessary to purify and amplify a DNA fragment prior to analysis. This pre-treatment required complex laboratory and highlights the advantage of being able to integrate all these procedures on one chip to make it possible to directly analyse a raw sample, such as a drop of blood. Achieving this would require miniaturizing systems such as cytometers, separators, and bioreactors, and then together. The domain of integrated analysis systems has been designated as µTAS (micro-total analysis systems) [3.14], or also Lab-on-a-chip (LOC) systems. The two terms are essentially synonymous. Lab-on-a-chip devices or µTAS delineate an abundant field that includes analysers of air and water quality, diagnostics of illnesses, and medical implants etc. The economic possibilities of this field have been estimated at tens of billions of dollars per year

3.3 Deep Reactive Ion Etching

Deep reactive ion etching (DRIE) is a key technology of recently fabricated microfluidics and a deeper insight into the physical phenomena is essential to understand ideas in later paragraphs, therefore in the following section a detailed description is provided.

Dry or plasma etching is a group of chemical processes, where the etching medium is produced by the dissociation and ionization of stable molecules or atoms, or through the formation of chemically active particles. The chemical manner of the process is determined such that the etching medium and the etched substrate constitute a volatile reaction product. This etch process has two significant advantages compared to wet etching. The generation of extremely reactive components (see Fig. 3.1) in the plasma (chemical etch), the etch rates are remarkably higher and due the possibility of directional etching, more complex 3D microstructures can be formed.

Dissociation:
$$CF_4 + e^- \rightarrow CF_3 + F + e^-$$

Ionization:
$$CF_3 + e^- \rightarrow CF_3^+ + 2e^-$$

Dissociative ionization:
$$CF_4 + e^- \rightarrow CF_3^+ + F + 2e^-$$

Excitation:
$$CF_4 + e^- \rightarrow CF_4^* + e^-$$

Recombination:
$$CF_3^+ + F + e^- \rightarrow CF_4$$
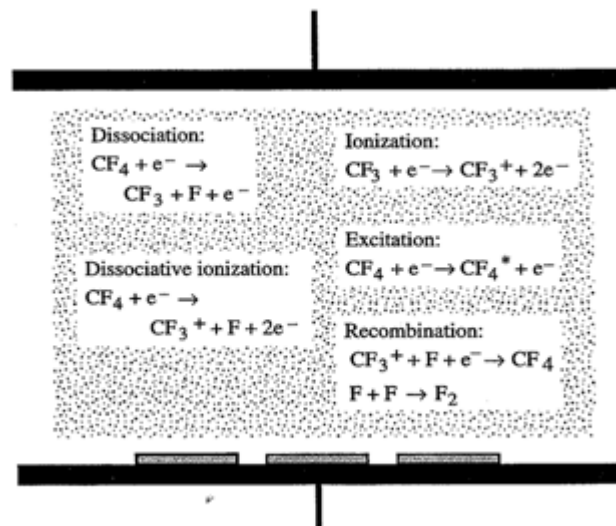$$F + F \rightarrow F_2$$

Figure 3.1: Main phenomena taking place in plasma [3.1]

The directionality of etching (referred to as physical etching) is resulted by the presence of ionized particles in the plasma, which are moved towards the wafer surface

through controlled electric field in the system. In special cases, chemical etching and anisotropic physical etching are performed in a synergetic manner intensifying the effect of one another. Therefore, etch rates higher than the sum of etch rate of individual components can be achieved.

Currently the most important dry etching process is the reactive ion etching (RIE), where the following sub-processes take place respectively.

- Generation of active particles from gas phase by ionization and dissociation of molecules in plasma glow. Active particles can be neutral species, electrons, protons, photons, free radicals or ions.
- Evolution of DC self-bias. Silicon wafer is placed on a capacitively coupled electrode driven by radiofrequency source. Since electron mobility is greater than that of ions, the electrode becomes negatively charged, also called as DC self-bias (see Fig. 3.2).
- Transport of neutral active radicals and positive ions from the plasma to wafer surface. Transport of radicals take place through diffusion, and ions are driven by DC-bias.
- Adsorption. Reactive species are immobilized on the surface of silicon wafer. Adsorption can be enhanced by ion bombardment, which removes the reaction product passivating Si surface.
- Reaction. Chemical reaction is to happen between adsorbed radicals and Si.
- Desorption. By-product should be volatile in order to transport into gas phase (high partial vapour pressure on substrate temperature). In some cases, additional ion bombardment can be carried out to remove them.
- Venting. Desorbed reaction product are diffused from the etched surface into the plasma, therefore they should be removed.
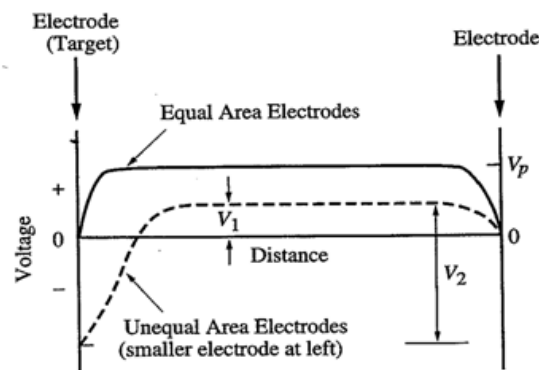

Figure 3.2: Potential distribution in plasma [3.1]

Etching of silicon takes place in halogen-based plasma because of the higher available etch rate. Gases generally used in DRIE systems are bromine, chlorine or fluorine. In the system I have worked with (Oxford Plasmalab 100 – see Fig. 3.3) fluorine based chemistry is used, which guarantees high etch rate, but limited anisotropy compared to bromine or chlorine. To increase the directionality of etching mechanism, ion-inhibitor techniques are applied. Etch stopping by-products deposited on the wafer surface are called inhibitors.

Most of today's DRIE systems are equipped by two energy source, one dedicated to generate plasma, and one used for controlling the translation of generated ions toward the wafer surface. The first source is usually inductively coupled (ICP), while later one is capacitively coupled. This way the density of free radicals and ions in plasma, and energy of ion bombardment can be tuned in independent manner.

During ion-inhibitor procedures, the inhibitor film is necessary to control directionality of etching. The sidewall of etched structures are less exposed to the effect of ion bombardment, therefore the film is only removed form the bottom of the trenches, where Si etching is preformed further. There are several ways of making inhibitor layer:

- Non-oxidant, silicon.oxihalogen gases (like O_2) entering in the reaction chamber.
- Freezing of non-volatile reaction products on the surface (e.g. cryogenic cooling).
- Injection of gases producing carbon-halogen polymers in the reaction chamber (C_4F_8 in case of fluorine based chemistry).
- Redeposition of etched mask materials (e.g. metal.halogens, resist by-products).

Injection of inhibitor gases can take place in parallel (mixed mode) or alternating (pulsed mode) way (Fig. 3.4).

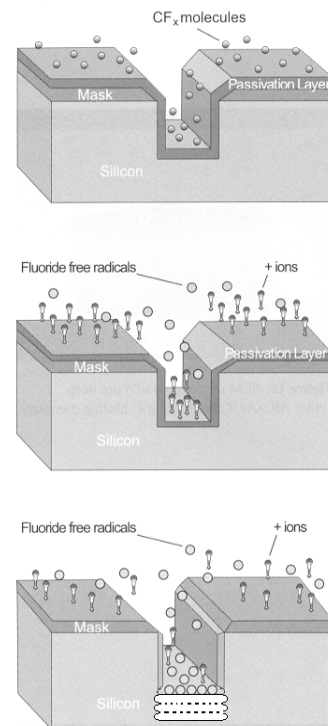Figure 3.3: Oxford Plasmalab 100 equipment used in MEMS Lab in MTA TTK MFA

Figure 3.4: Schematic of Bosch process

Pulsed mode is often referred as Bosch process, since Robert Bosch GmbH has patented [3.15].

In mixed mode usually oxidant gases are used and wafers are cryogenically cooled in order to reinforce the inhibitor layer. In pulsed mode fluoro-carbon gases responsible for polymer deposition are initiated into the reaction chamber. This way a highly etch resistant layer is formed even at room temperature.

3.4 Microchannels in silicon MEMS

In silicon MEMS technology surface and bulk micromaching techniques can be used to fabricate microchannels utilizing conventional clean lab processes such as thin film depositions, photolithography, wet & dry etching techniques.

Silicon surface micromachining refers to different techniques using etching of sacrificial layers or underetching a substrate to form partially released or freely movable structures [3.16]. The term surface micromachining was originally defined for processes using sacrificial layers to form thin film microstructures. Recently polymeric surface micromachining has been introduced, however, in my work I only focus on silicon-based technologies.

A general surface micromachining process for microchannels starts with deposition of the sacrificial layer. The channel material is then deposited over the structured sacrificial layer. After opening etch accesses through the channel wall, the sacrificial layer is etched to hollow the channel. A subsequent deposition of channel material seals the hollow channel.

PSG is deposited as a sacrificial layer over a ground silicon nitride layer. The structured sacrificial layer is then encapsulated by LPCVD silicon nitride. Etch access is opened with RIE of the nitride wall. After removing the sacrificial PSG, a second LPCVD process seals the empty channel with silicon nitride. In a similar process, the channel is underetched resulting in a suspended nitride channel [3.17] (Figure 3.5.a).
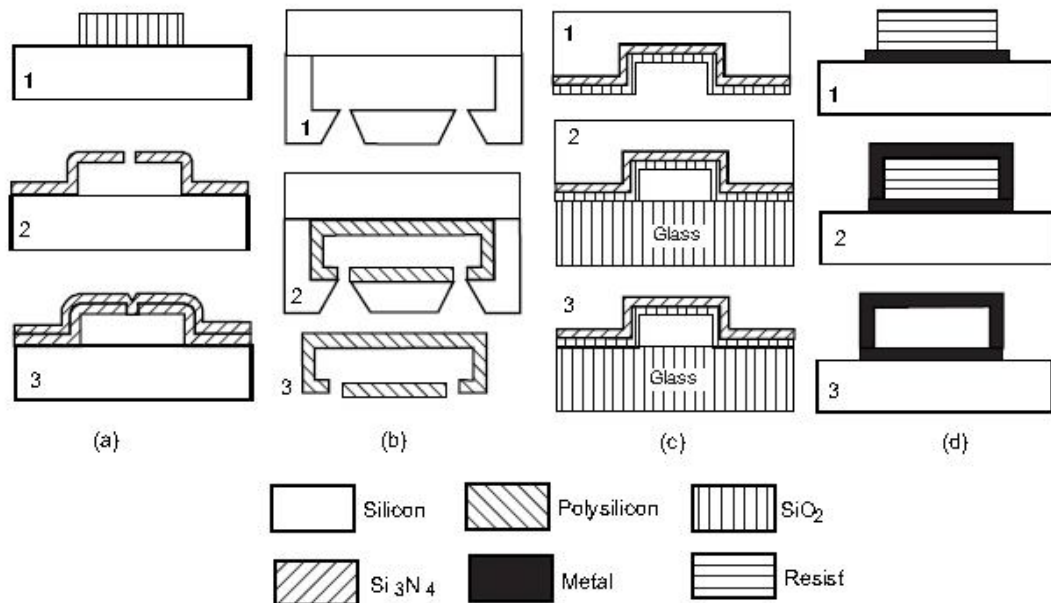

Figure 3.5: Surface-micromachined channels [3.16]: (a) polysilicon channel; (b) moulded silicon channel; (c) oxide/nitride channel; and (d) metal channel.

18

Using the HexSil method [3.18], polysilicon channels can be fabricated with a silicon mould [3.19]. The mould is fabricated in silicon using bulk micromachining. Before depositing the channel material, a sacrificial oxide layer is deposited on the inner wall of the mould wafer. Polysilicon deposition defines the channel wall. Etching away silicon dioxide releases the polysilicon channel. The moulding approach overcomes the thickness limitation of the standard surface micromachining process, where the channel height is constrained by the thickness of the sacrificial layer (Figure 3.5.b).

The moulding approach can be further developed with the silicon substrate as sacrificial material. Similar to the process of [3.20], the mould is fabricated in a handle wafer with bulk micromachining. The channel wall is defined by deposition of nitride/oxide double layer. With silicon dioxide on top, the silicon wafer is bonded anodically to a glass wafer. Etching away the silicon handle wafer releases the nitride/oxide channel on glass. If the channel wall is too thin for certain applications, the surface of the structure on glass can be coated with a thick polymer layer (Figure 3.5.c).

Besides the above moulding approaches, microchannels with reasonable heights can be fabricated with the process described in [3.21] (Figure 3.5.d). The process starts with deposition of a metal seed layer on the substrate (e.g. Ni). A subsequent electroplating process defines the bottom wall of the channel. Next, a thick film photoresist such as AZ4620 is deposited and developed to form the sacrificial structure for the channel. Gold is then sputtered on the resist structure as the second seed layer. Electroplating on this seed layer forms the side wall and top wall of the channel. Etching the gold layer exposes the sacrificial photoresist. Removing photoresist with acetone creates a hollow metal channel.

Because of the limited dimension only low throughput microfluidics – even better to call them nanofluidic systems - can be realised by surface micromachining methods. Contrarily bulk micromachining methods offer a more reasonable exploitation of substrate materials, and therefore give a larger freedom for tuning channel profile and hydrodynamic resistance.

Both isotropic and anisotropic etching can be used to fabricate microchannels in bulk material such as glass or silicon [3.16]. A variety of cross-sectional channel shapes can be achieved by combining different micromachining techniques. Since glass is a familiar material in chemistry and life sciences, microchannels in glass attract attention of applications in these fields [3.22-3.23]. Glass consists mainly of silicon dioxide and therefore can be etched with conventional oxide etchants. Channels can be etched in fused silica wafers using a polysilicon mask [3.22]. The two glass wafers are bonded together at high temperatures. Channels in other glass types can be etched in fluoride-based solutions [3.24-3.25].

Isotropic etching in silicon results in channel shapes similar to those of glass etching. Figure 3.6 show channels formed by anisotropic etching of (100) - [3.26] and (110)-wafers [3.23] respectively. A glass wafer or a silicon wafer covers the channels using anodic bonding or silicon fusion bonding. By combining two etched wafers, different channel shapes can be achieved (Figure 3.6).
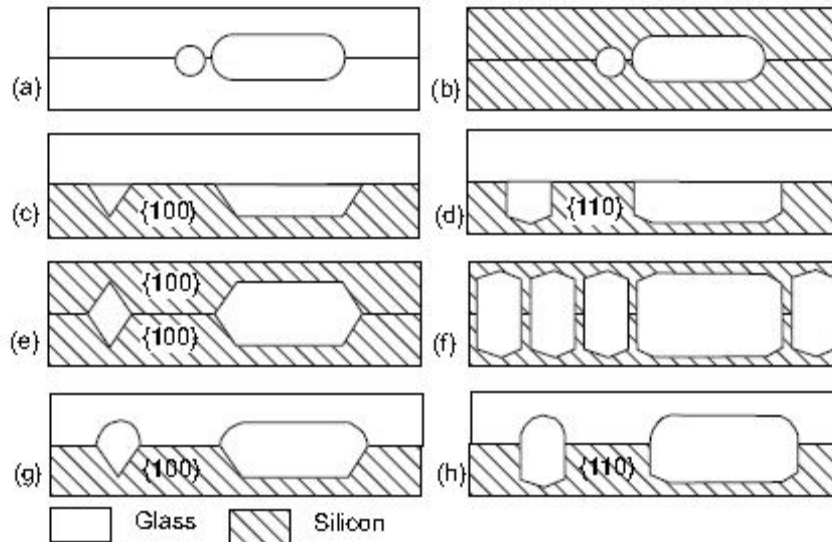
Figure 3.6: Bulk micromachined channels [3.16]: (a) glass-glass; (b) silicon-silicon; (c) glass-silicon; (d) glass-silicon; (e) siliconsilicon; (f) silicon-silicon; (g) glass-silicon; and (h) glass-silicon.

The microchannels described in Figure 3.6 have drawbacks of wafer-to-wafer bonding. For channels shown in Figures 3.6(a–h), misalignments and voids trapped during bonding processes can change the desired shapes and consequently the device function. Therefore, fabrication of covered channels in a single wafer is increasingly important. The general concept of these methods is to fabricate a buried channel in a single substrate and to cover the etch access with a subsequent deposition process.

Figure 3.7 describes the basic steps of making a buried channel in (100) wafer. To start with, a highly boron-doped silicon layer with a doping concentration higher than 7×10^{19} cm^{-3} is used as mask layer for the subsequent wet etching process. Etch accesses are opened by RIE through the highly boron-doped layer. The buried channel is etched by EDP, which does not attack the boron-doped layer. After anisotropic etching, the access gaps are sealed by thermal oxidation. The final deposition of silicon nitride covers the entire structure [3.27]. The burying depth of the channel described above depends on the thickness of the highly boron-doped layer, which is a maximum 5-10 μm due to limits of diffusion processes.
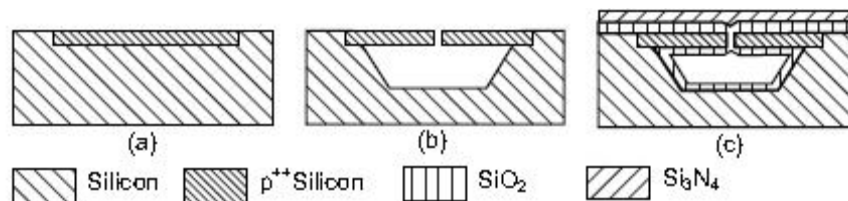

Figure 3.7: Buried channel with highly boron-doped silicon layer as cover [3.27]: (a) boron doping; (b) opening etch access, anisotropic wet etching; and (c) deposition of silicon oxide and silicon nitride.

As Deep Reactive Ion Etching techniques appeared in the middle of the 1990s, dry etching has gone through revolutionary change in microtechnology. As a result, combination of anisotropic and isotropic dry etching techniques has been developed to

fabricate microfluidics. In this field a milestone was established the concept of buried channel technology [3.28] using highly anisotropic dry etching techniques. The advantage of the method is that the entire volume of the substrate can exploited, which is a key property regarding the decreasing size of today's neural implants. Since then several applications has been proposed in the literature [3.29-3.32], however, attempt to optimize the original process flow in order to utilize it in devices with complex functionalities has not been made. Appendix A describes the concept of this technique.

In my work, an optimized fabrication process of the original channel formation concept is presented, which eventually results in superb surface planarity above the sealed microchannel. My proposed technology is suitable for being integrated into hollow silicon microprobe containing electrodes of small feature size.

4. Development and characterisation of drug delivery system for Si microprobes

## 4.1. History & advances in silicon microprobe technology

The initial use of microelectrodes in neural investigations dates back to the 1950s. Since then, single wire metal microelectrodes have been extensively applied in field of electrophysiological measurements mainly in extracellular environments. Metal electrodes generally contain an insulated metal wire except for the tip of the wire which serves as the recording site for electrical signal collection [4.1-4.2]. By 1970s, a breakthrough in fabrication technology emerged when Wise and his group took advantage of integrated circuit microfabrication techniques and reported the use of the first silicon-based microprobe to interface neural tissues [4.3]. Since this pioneering work, silicon micromachining techniques has become a leading fabrication technology to realise and develop neural probes and probe arrays in the microscale [4.4-4.8] and eventually contributed to the establishment of the field of Neural MEMS or NeuroMEMS. Recently, polymer based microprobes have received more attention because of the emerging of simple and inexpensive fabrication process, flexibility and biocompatibility [4.9-4.10], however, the reign of silicon based probes is sustainable due to reproducibility and large scale integration of several functions such as read-out electronics, fluidic or optical systems [4.8].

The fabrication of silicon neural probes is based on thin film deposition (including deposition of a metal layer on an insulated substrate) and subsequent patterning of the deposited layers by photolithographic techniques to form recording sites or read-out pads for interfacing external signal processing units. An insulating thin film is finally deposited over the realised microstructure and patterned providing open access to recording sites and bonding pads. The role of the substrate is definitely to provide mechanical support during surgical implantation.

The introduction of MEMS technology including both surface and bulk micromachining techniques significantly standardized the fabrication of microprobes with well defined probe shafts and precise placement of recording sites [4.11]. The issues of manual or non-automated microprobe production have diminished by silicon microtechnology featured by high accuracy, repeatability and batch production at a low unit cost. Inherent property of silicon micromachining is the possibility to integrate signal processing circuitry [4.12] or microactuators driving the electrode shaft in order to track the neuron movement [4.13]. The use of silicon photolithography process allow excellent control over the recording site size, shape and spacing enabling multiple recording sites to be placed at variable heights on a single electrode shank. Such ability allows insertion of a large number of recording sites in a small volume which is not possible with metal wire arrays or bundles. Inclusion of integrated circuits can be performed directly on the probes and offers benefits in terms of better signal acquisition, reducing power line interference, and ultimately reducing the overall probe size by reducing the electrical cable sizes [4.14].

A silicon-based in-plane probe used widespread in the detection of neural activity is the Michigan probe [4.15] (also see Fig. 4.1). The fabrication process of Michigan probes is based on anisotropic etching with ethylene diamine pyrocatechol (EDP) utilizing a boron-etch-stop. The process takes advantage of the fact that the etch rate for

p-type silicon is much slower than for un-doped silicon. Boron doping is first performed on silicon by ion implantation or diffusion to define the shaft thickness in the substrate and followed by EDP wet etching to release the probe shafts by having a rounded cross-section and a rounded sharpened tip.
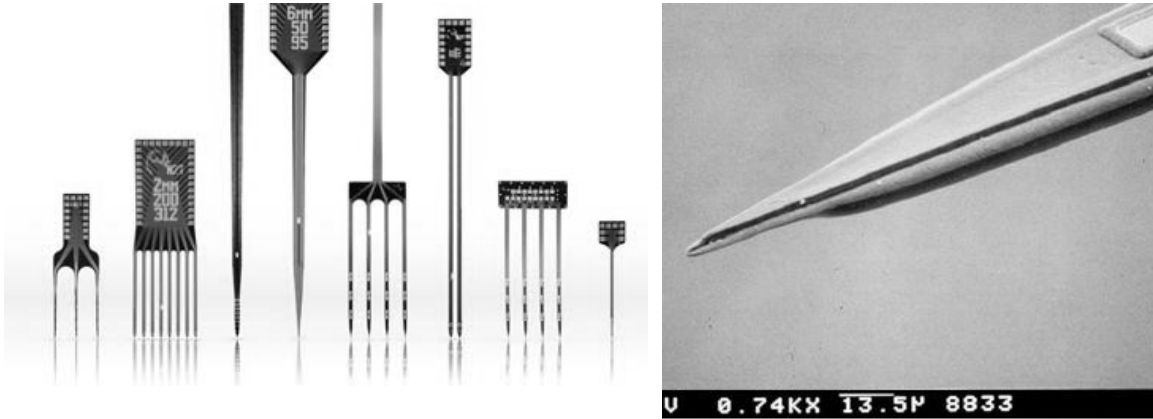
Figure 4.1: Single and multi-shaft Michigan probes [4.15]

Metal recording sites can be formed by gold, platinum, or iridium deposition. The final insulation on the top is made with triple layers of silicon dioxide, silicon nitride, and silicon dioxide. Finally, the interconnection is made with a 4–5μm thick polysilicon cables which are reported as weak cables and easy to break leading to lower yield for long lengths because of the high aspect ratio and lack of robustness [4.15]. Michigan probes have been successfully used in a number of neuroscience applications, but they also suffer from some disadvantages related to probe thickness and durability. Mechanical weakness of the probes may lead to crack and shatter and may cause severe damage and disturbance to the brain tissue during insertion.

Another well-known silicon based-probes incorporating multiple-electrode arrays is the Utah type microelectrodes [4.16-4.17] (Figure 4.2). The Utah electrode arrays are usually micromachined from 1.83mm thick boron doped silicon substrates. First, a diamond dicing saw is applied to make a grid pattern of several hundred micrometer deep grooves on the surface of the substrate. The electrode bases are sealed by deposited glass. Electrode columns are then formed by additionally sawing a grid on the other side of the silicon wafer and also separated by glass insulation. Wet chemical etching provides smoothes pillars and creates sharpened probe tips. Tips are then coated with metals (Au, Pt tor Yr) for recording. At the end, polyimide is used to cover probes as insulation layer. The Utah electrode arrays are out-of-plane electrodes as opposed to all other silicon neural probes which are in-plane (horizontally oriented) electrodes. As a result, the probe length of the Utah electrode arrays is quite limited by the thickness of the silicon wafer.
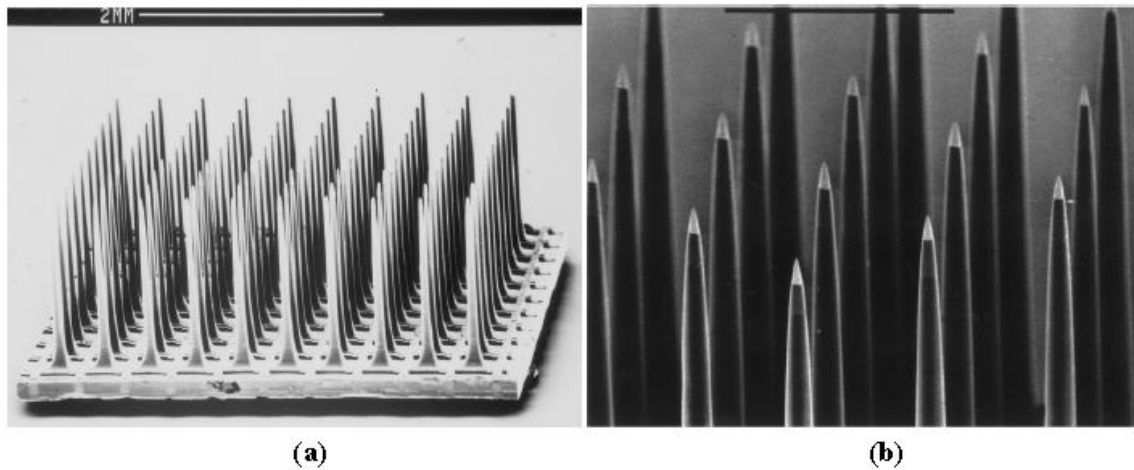
Figure 4.2: Microscopic view of Utah electrode array (a.) and its tip shape (b.)
[4.16].

Recently, SOI (Silicon-on-Insulator) wafers have become popular, which are produced by placing a thin, insulating layer such as silicon oxide (SiO_2) sandwiched between a thin layer of silicon (device layer) and the silicon substrate (also called as handle wafer). SOI based neural probes employ the buried SiO_2 layer as an etch-stop layer. Both wet [4.18] and dry [4.19] chemical etching process exist, where etch rates for SiO_2 are much lower than for silicon. The handle wafer is etched through from the backside in order to release the probe shaft. This means that the probe shaft thickness is limited by the thickness of the device layer of SOI wafers. Different techniques have been used to develop neural probes using SOI wafers starting with the use of backside wet-etching using potassium hydroxide (KOH) solutions. Plasma etching technology for silicon was also employed which led to the establishment of new fabrication processes to develop neural probes. Plasma etching is a physical-chemical dry etching technique which offers several advantages over traditional wet etching including more reliability and yields a smoother and cleaner etched surface. The plasma etching also has other advantages including relative insensitivity of the etch rate for silicon to its electrical conductivity, less corrosion problems for metal features in the recording sites, and less undercutting and broadening of the photoresist features. Therefore, the use of SOI wafers combined with plasma etching technique provides a good control over the final probe thickness compared to using wet etching with a boron etch-stop.

More recently, novel approaches of fabrication microprobe arrays have appeared embedding single silicon shafts in a matrix [4.20-4.21].

In the following chapters my contribution to the buried microchannel development both in fabrication and integration technology is detailed. A preliminary characterisation on channel geometry as well as my experimental investigation on mechanical behaviour of hollow probes and fluidic functionality is also involved.

4.2 Development of drug delivery system in silicon microprobes

4.2.1 Fabrication of buried microchannels

The advantage of the concept of buried channel technology is that a network of sealed microchannels can be formed at different depths in bulk silicon. A summary of the currently known and applied technology can be found in [4.22] and also presented in Appendix A. The process starts with a DRIE step of a narrow trench. After the trench wall is protected by SiO_2 or SiN_x deposition, the protective layer at the bottom of the trench is removed by a RIE process to allow the formation of the channel by either anisotropic or isotropic wet or dry etching step.

Major properties considered for improvements or simplifications are as follows:

- All alternative process flows demonstrated used thermal SiO_2 (or LPCVD SiN_x) + Cr double layer as a mask in the first step.
- All of the process flows required protection of the coating layer using a combination of an additional pre-etch step and a sacrificial layer etch, which also limits surface planarity above the microchannels.
- In all cases costly cryogenic ICP-SF_6 plasma etching was used for the Si DRIE of the trench.
- SiO_2, SiN_x etch were performed by a RIE, which resulted in greater mask erosion.

In Appendix A my simplified process flow is compared to the traditional technology proposed by de Boer et al [4.22]. Several steps of Scheme 1 (a combination of Cryogenic DRIE and isotropic dry RIE-SF_6 recipe), have been enhanced. Detailed process parameters of the applied etch recipes are shown in Table 4.1.

In my work, all the etching step (including both SiO_2 & Si etch) was performed in an Oxford Plasmalab System 100 ICP 300 type DRIE.

Initial substrate is a (100) single-crystalline silicon wafer. It should be noticed that the crystallographic orientation and resistivity of the silicon substrate are not critical (step 1). As a masking material for Si etching, thermally grown wet oxide and SPR220 photoresist are used. Since a highly selective ICP process is applied for pattern transfer, no additional Cr layer is necessary (step 2). Pattern transfer is completed by a dry etch of SiO_2 masking layer in C_4F_8 + O_2 plasma was used for pattern transfer (step 3). In my optimized process no under-etching or sacrificial layer etch is needed, in contrast with Step 3 of the traditional BCT process. In the next step a room temperature Bosch-process is used for deep trench etching (step 4), which is more robust and cheaper than the cryogenic DRIE of the traditional technology. Aspect ratio better than 1:25 can be now achieved using the Bosch-process [4.23]. The surface roughness of the walls, originating from the sequential passivation/etch steps, is approximately 150nm.

	SiO₂ etch	Deep Si etch – Bosch process (passivation/etch)	Highly anisotropic SiO₂ etch	Isotropic Si etch
Process step	Step 3	Step 4	Step 7	Step 8
Pressure	8mtorr	30mtorr / 40mtorr	30mtorr	40mtorr
ICP power	2000W	- / 750W	-	750W
LF power (350kHz)	-	1W / 8W	-	8W
RF power	100W	-	200W	
C_4F_8 flow rate	36sccm	100sccm / -	-	
O_2 flow rate	4sccm	-	-	
SF_6 flow rate	-	- / 150sccm	-	150sccm
Ar flow rate	-	-	20sccm	
CHF_3 flow rate	-	-	30sccm	
Etch time	-	4sec / 9sec (cycle time)	5min	5min

Table 4.1: DRIE etch parameters. A standard cubic centimetre (sccm) is defined as the volumetric flow rate at calibration reference conditions of 1013.25 hPa and 0°C.

As Fig. 4.3 presents, this roughness causes no problems in the following etching steps. After preliminary trench etch a 100nm thick thermal SiO_2 is grown on the substrate (step 5), which also removes the residual fluorocarbon-polymers from the passivation step of sidewalls during Bosch-process.
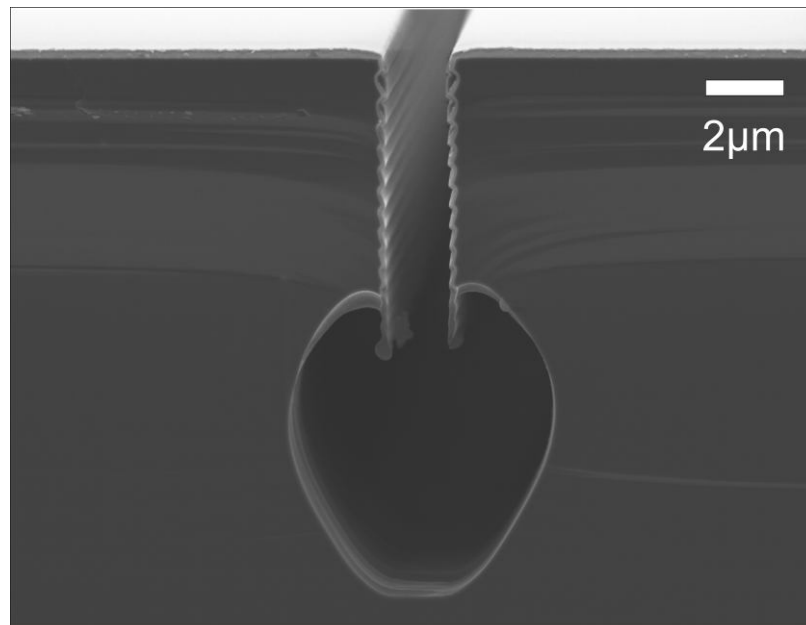
Figure 4.3: Open channels after the isotropic etch of Si.

Electron beam evaporation of a 100nm thick Al layer follows the oxidation (step 6), which will act as a protective coating not only for the planar surfaces, but also for the

trench edge and the rough sidewall as well (Fig. 4.4).   The beneficial effects of the Al layer are detailed later in this chapter.
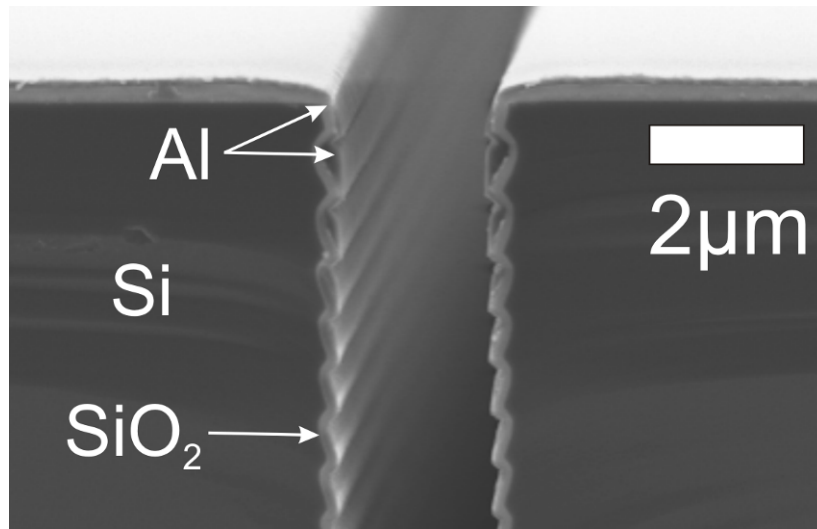
Figure 4.4: Aluminium step-coverage in the close vicinity of the trench opening

In order to remove the SiO_2 protection layer from the bottom of the trench, an anisotropic etch recipe using CHF_3 + Ar plasma chemistry is utilized (step 7).   The formation of microchannels (isotropic Si etch) is carried out in SF_6 plasma (step 8). During the isotropic Si etch step, the thermally grown 100nm oxide becomes partially free standing, but still mechanically stable. No bending of the material occurred, which could otherwise close the trench and reduce the etch rate. Wet etching of the sidewall protection in BHF for 10 minutes removes both Al and SiO_2 protection layers (step 9). Fig 4.3 shows a cross-sectional image of the channel before filling. After dehydration of the wafers at 300°C, an LPCVD process is applied for closing and sealing of the trenches by poly-Si deposition (step 10). An additional annealing of the poly-Si layer at 1000°C reduces the stress in the deposited layer. A cross section SEM image of a sealed channel is shown on Fig. 4.5.
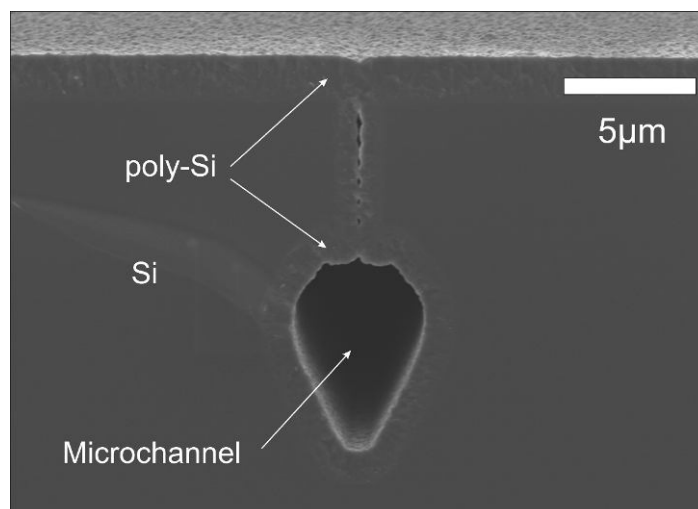
Figure 4.5: Cross-section of a buried microchannel after the sealing by LPCVD poly-Si deposition is completed.

The 100nm thick aluminium masking layer was deposited in order to protect the edges of the trench during both the anisotropic dry SiO_2 etching and the isotropic Si etching steps. Since the step-coverage of electron beam evaporation is poor in case of trenches with a small feature size, the bottom of such structures (width close to the micron range) is left almost uncovered, so anisotropic dry oxide etching is not affected significantly [patent pending – 4.24].

The analysis of the step coverage of the evaporation process was carried out using the planetary evaporation model of SILVACO Virtual Wafer Fab [4.24a]. Model parameters were adjusted according to the experimental setup of the Varian 3120 vacuum chamber. Al coverage versus aspect ratio at various trench widths was simulated by the Elite module and is presented by Fig. 4.6.
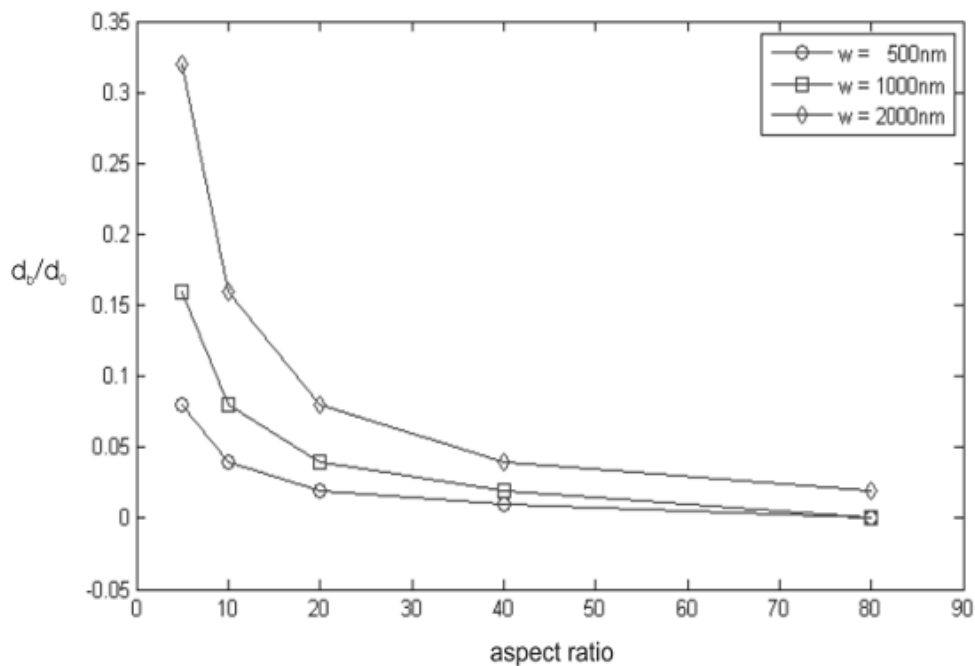
Figure 4.6: The thickness of Al layer deposited at the bottom of the trench strongly depends on the width (w) and the aspect ratio of that – Al thickness on the plane wafer surface and at the bottom of the trench is denoted by d_0 (100nm) and d_b respectively.

Images on the step-coverage in the close vicinity of the trench edges are shown on Fig. 4.4.

The Al passivation of the trench edges also modifies the characteristics of the subsequent etching steps. Different masking layers in DRIE processes can influence not only the etch profile but the etch rate as well [4.25-4.26]. Al can easily heat up due to eddy currents, so local rising of temperature might cause increasing etch rate as well as directional changes.

The aspect ratio of the trenches also influences the etch rate. If the aspect ratio is increasing, a thinner Al layer will be present at the bottom of the trench, which affects the anisotropic oxide etch cycle significantly. On the other hand, due to the physical ion depletion and bowing, the effect of diffusion on the supply of reactants to the bottom of the trench, and consumption of reactants at the trench sidewalls is limited [4.25, 4.27], therefore smaller openings are etched slower. These two phenomena are supposed to

result in a compensation of aspect ratio dependent etching during the isotropic Si etch (channel formation). The above statements are still being thoroughly investigated in order to determine safety margins of the proposed technology.

The final microstructure after isotropic Si etch of the sample is shown on Fig. 4.5. Some unique features of the proposed method of edge passivation can be concluded as follows:

- Due to the step-coverage of e-beam evaporation, trenches, channels or reservoirs of larger feature size (aspect ratio < 5) on the wafer are substantially protected by the aluminium layer from being etched during isotropic Si etch in SF_6 plasma (step 8). The effect is apparent on Fig. 4.7. That property enables to form the fluidic inlets simultaneously with the channels using the same lithography step.
- Further advantage of the proposed edge-protection method is that wafers can be exposed to long Si and SiO_2 etch cycles due to the high selectivity of both the anisotropic dry oxide etch and the isotropic dry Si etching [4.28] to the Al + SiO_2 masking double-layer. As a result, the formation of microchannels buried deeply below the surface (aspect ratio > 30, at a depth of even 150μm) of the silicon substrate is possible.
- The most apparent benefit of the modified technology is not only the optimized process flow, but the protection of the surface planarity. While under-etching has practically disappeared from the vicinity of the edges, the poor quality of the surface topography above the filled trenches is reduced as well below the micrometer range (see Fig. 4.8). Average depth of the orifices is in the 200-300nm range, while the depth realized by de Boer et al. was approximately 5-10μm.
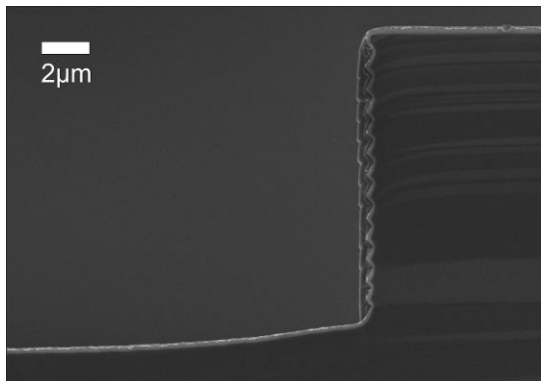

Figure 4.7: Profile of the isotropic Si etch of a fluidic reservoir (the Si etch is practically inhibited on the surfaces covered by the evaporated aluminium layer).
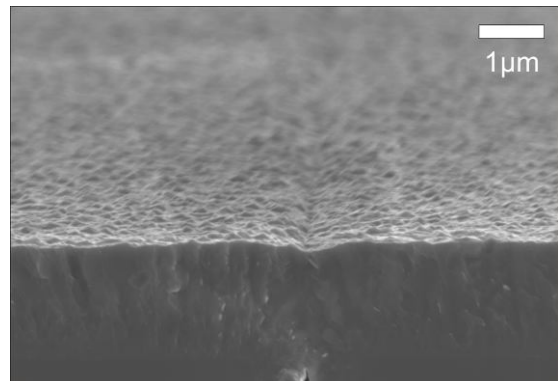
Figure 4.8: Close SEM view on the surface profile of a sealed trench. It is apparent that the size of the orifice is well below the micron range.

Fig. 4.9 shows a cross-sectional view of a fluidic channel fabricated by the new planar process (a.), and one realized by the traditional technology, while no protection of the coating layers is performed at all (b.). In the first case, the reproducibility and controllability of the process is not reliable. My enhanced process results in a well-controlled, planar poly-Si surface, which enables the further CMOS processing after buried channel formation is complete.
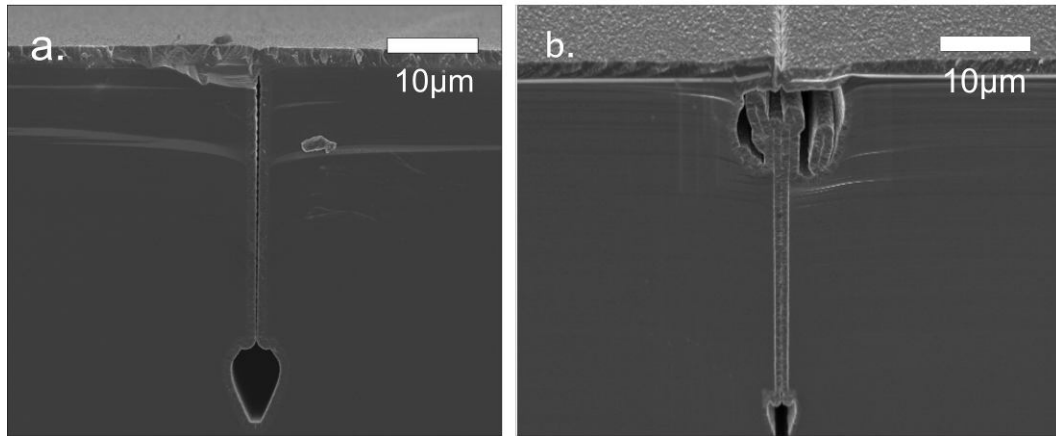
Figure 4.9: Sealed microchannels fabricated by the improved technology with mask protection (a.), and by the original technology, but without mask protection (b.). On the right SEM picture, the collapse of the under-etched masking oxide layers around the trench opening can be clearly seen.

In my work, it was aimed to make improvements and simplifications in the microfabrication technology of silicon buried microchannels. The edge protection of the trenches before the anisotropic dry oxide etch was achieved by a simple aluminium evaporation step, which finally resulted in excellent surface planarity above the sealed microchannels. In my enhanced process flow, an additional Cr mask is not necessary, and both pre-etch cycles and sacrificial layer etch steps can also be omitted. Moreover, the applied ICP etch recipes results in less damage of the masking layer [4.29]. Introducing a room temperature Bosch process instead of cryogenic or mixed mode DRIE the whole process flow becomes more cost-effective.

The sealing properties of the microchannels can be improved further by testing some emerging technology development including tapering [4.30] or sidewall smoothness [4.31] of Bosch-process.

The proposed development contributes to the integration of the buried microchannel technology into the fabrication scheme of hollow silicon neural microprobes with high-density electrode system for deep-brain stimulation applications [4.32].

4.2.2 Fabrication parameters vs. microchannel shape

Etching mechanisms

When etching high aspect ratio (AR) trenches into silicon with reactive ion etching, it is observed that the etch rate is depending on the feature sizes. Therefore smaller trench openings are etched slower compared to wider ones. This effect is known as RIE lag or ARDE (aspect ratio dependent etching) and is caused by the depletion of etching ions and radicals or inhibiting neutrals during their orbit in a trench [4.25-4.27, 4.33]. We can use the RIE lag to create trenches with different depth, e.g. buried channels defined by narrow (1-2μm) openings can be placed shallower, while fluidic inlets with larger feature sizes will be etched much deeper, which can be useful to establish the fluidic connection to an outer interface. This effect is also shown on the schematic illustration of the process flow in Appendix A.

Channel formation takes place in SF_6 plasma. The SF_6 etch can be described as a highly chemical and radical-dependent etching mechanism [4.34]. Since the pure SF_6 plasma lacks any passivation mechanisms above room temperature, the final etch profiles are almost isotropic. The etch process is generally considered to be chemical, where the rate-limiting step is desorption of the etch products. In this process the ion flux to the surface enhances the etch rate by assisting desorption. Since the ion flux works upon the etch rate, Si etch in SF_6 will be influenced by shadowing effects at the bottom of a trench. This shadowing effect depends on the ion angular distribution caused by ion collisions [4.26] and the AR of the trench.

Dry etch profiles

Based on the above discussed etching mechanisms the following observations are made about the channel etch and geometry.

AR dependent etch rate: using cross sectional SEM profile analysis we observed decreasing average etch rate with increasing aspect ratio. I suppose that this is the same mechanism that causes the RIE lag, the depletion of etching ions and radicals. Fig. 4.10 shows the tendency that we observed in my experiments.
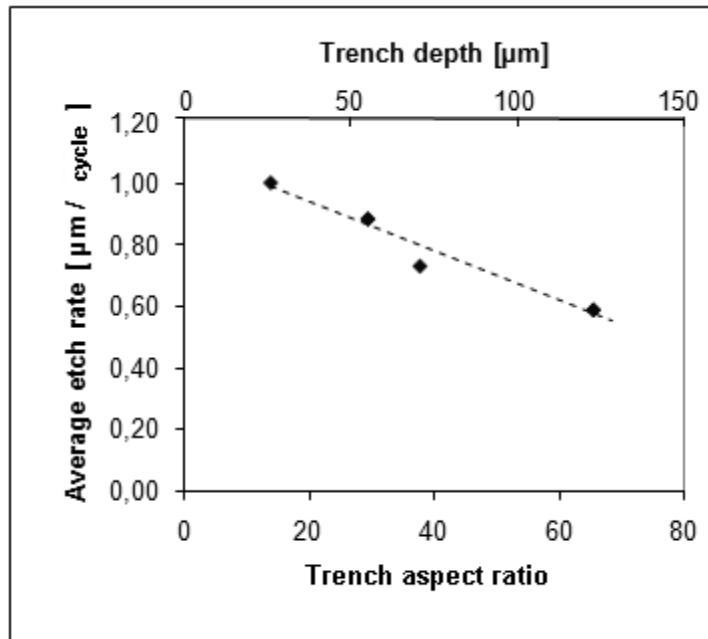
Figure 4.10: Change of etch rate vs. final geometry of the trenches.

AR dependent anisotropy: Fig. 4.11 shows two cross sectional SEM image of the microchannels before the trench-filling step. Etch rate in the horizontal direction slows down with increasing AR because of the shadowing of the ionic flux component. The deeper the trench is, the more anisotropic the channel will be while using the same plasma conditions.
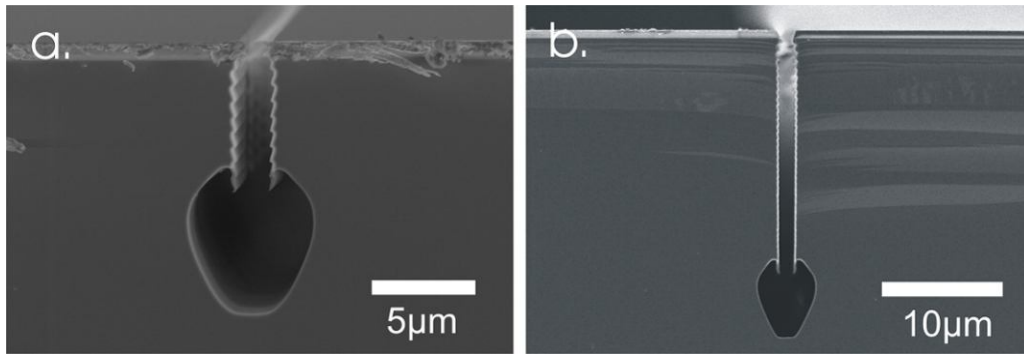
Figure 4.11: Profile of DRIE etched buried channels before trench-filling in case of aspect ratios 4 (a.) and 14 (b.).

Fig. 4.12 shows the vertical and horizontal etch rate versus the AR. Both etch rate slow down with increasing AR. The vertical component is influenced mainly by the depletion of the radicals. The horizontal etch rate is decreasing faster than the vertical, causing a more anisotropic profile of the channel with increasing depth. I suppose that the horizontal etch rate is influenced not only by the depletion of the radicals, but a highly decreasing horizontal ion flux is superposed, originating from the shadowing effect of the trench wall [4.27]. Since the ion flux to the surface enhances the etch rate by assisting desorption, reduced ion flux will cause lower etch rate.
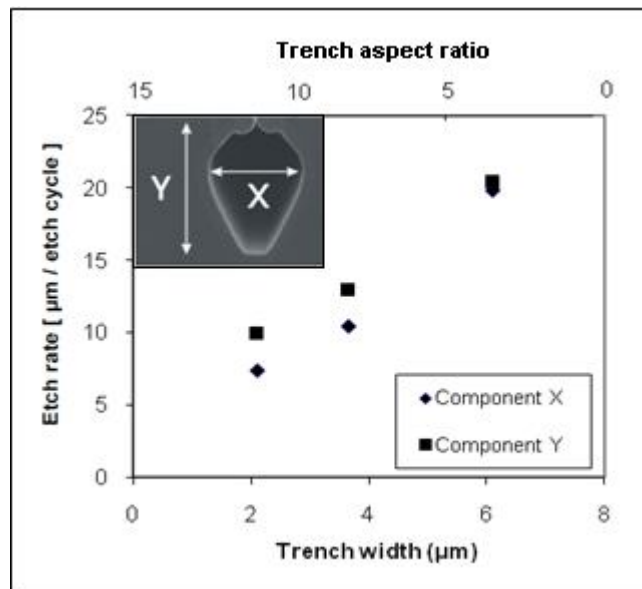
Figure 4.12: Change of etch components vs. final geometry of the trenches. Trench width is 2µm.

4.2.3 Integration into neural microprobes

 Probe layout

Mask layout was designed as individual probes attached to a silicon frame contained single shafts capable of penetrating the brain, and the bonding pad area. The overview of an entire silicon wafer with the probes and frames is shown in Fig. 4.14.

Shafts were 15-70mm long with several widths (200µm, 400µm) and thicknesses (200µm, 400µm). On the shaft there are 4 and 16 square-shaped (30µm×30µm) exposed Pt contact sites for extracellular potential recording with equal centre to centre distances of 100 µm. Each recording site is electrically connected to a bonding pad, via 6µm-wide conductive wires with 5µm-wide gaps between them.
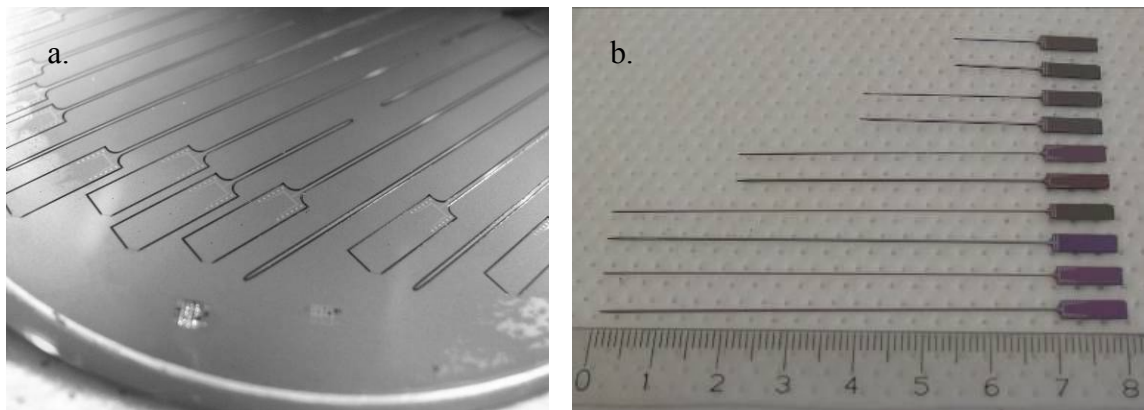
Figure 4.14: Through-wafer etched microprobe before complete release (a), realized silicon deep-brain probes with 15-70mm shaft length (b).

Overview of the fabrication process

Four photolithography masks were used to define the planar microstructure and the shape of the probe. All masks served for front side micromachining and defined the buried microchannels, the conductor and passivation layers, and the shape of the probe shafts. The formation of microchannels has been detailed in Chapter 4.2 and illustrated by Appendix A, therefore in this section the steps of the proposed microprobe technology are continuously explained after channels have been sealed by LPCVD poly-silicon.

After deposition of the initial insulation by thermal oxidation and by LPCVD of low-stress silicon nitride, the conductor layer was deposited by sputtering and patterned by lift-off technology. TiO_x and Pt sputtering were used to form the adhesion and conductor layers [4.27a]. This was followed by depositing and patterning of the insulation and protection layers, which define recording sites and bonding pads. Probe shafts and microfluidic inlets were formed and released by through wafer etch using deep reactive ion etching through metal mask.

Formation of the insulator and conductor structure of the probe

Silicon wafers containing the buried microchannels (Step 1, Appendix B) were oxidized in wet atmosphere at 1100 °C in order to grow a 1000nm thick thermal SiO_2 layer on the substrate (Step 2). A 300nm thick low-stress silicon nitride (SiN_x) film was then deposited by LPCVD at 830 °C (Step 3). Note, that each layer is removed by buffered HF and phosphorous acid from the backside before further processing.

A sacrificial Al layer was used to define the pattern of the TiO_x/Pt conductor path via a standard lift-off process (Steps 4-6). First, the 300nm thick sacrificial Al layer was deposited by electron beam evaporation. This was followed by the first photolithography and etching steps defining the negative pattern of the conductor path. In the next step, the photoresist layer was left in situ. The conductor layer consisted of a 15nm thick adhesion layer of TiO_x formed by reactive sputtering of Ti in an Ar/O_2. In the same vacuum cycle, 270nm thick Pt was sputtered on top of TiO_x. The photoresist together with the overlying TiO_x/Pt layer was removed using acetone. The Al layer was etched away as before, to complete with the lift-off process. In the next step, 300nm thick SiO_2 and SiN_x layers were deposited using LPCVD at 430 °C and 830°C (Step 7-8) respectively. Contact and bonding sites were defined by additional photolithography step followed by selective SiO_2 and SiN_x wet etching process in NH_4F buffered HF and phosphorous acid until the total removal of the oxide and nitride layers (Step 8).

Formation of microprobe shaft

The probe shaft and inlet reservoirs were micromachined by dry etching using Bosch recipe in a DRIE chamber. Masking layer was standard photoresist on the front side, while the etch stop layers were electron beam evaporated aluminium and subsequently spin-coated photoresist (step 10), which provided good thermal and mechanical distribution along the etch process.

The final microstructures have been analysed by SEM and optical microscopy. Results are illustrated by Fig. 4.15 & Fig. 4.16.

One can conclude that the integration of microfluidic and electric functions in the probe shaft has been successfully completed. The proposed process is the first demonstration of a hollow silicon microprobe fabricated by DRIE in a single substrate.
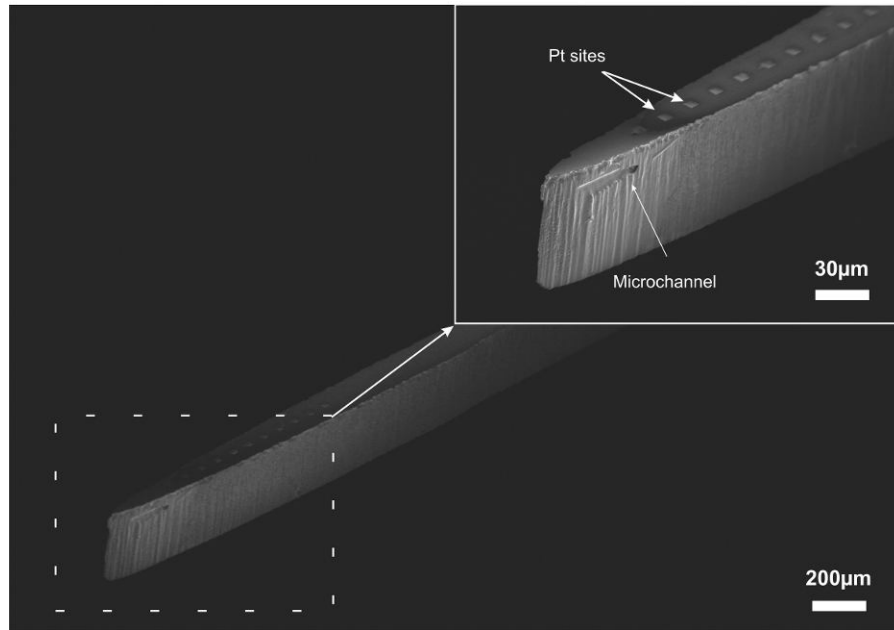
Figure 4.15: Hollow silicon microprobes realised by deep reactive ion etching and containing both fluidic ports and electrical recording sites
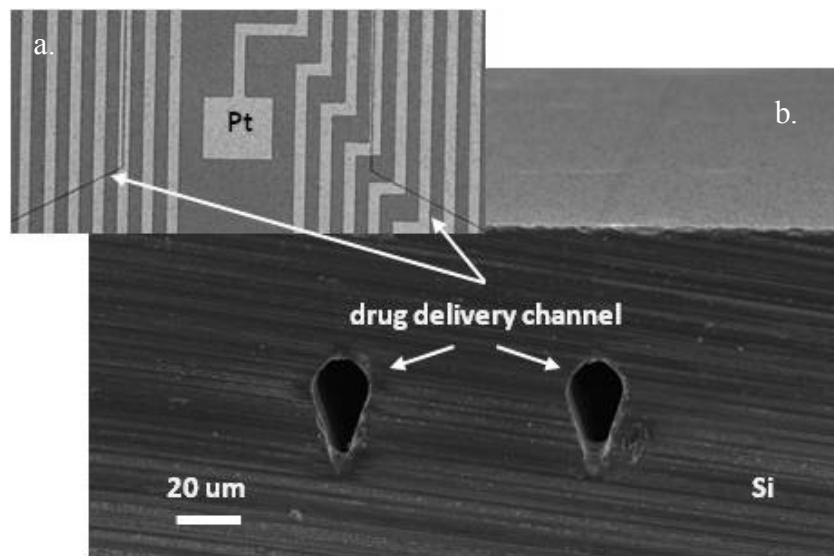

Figure 4.16: a) Optical microscopy image of the Pt wiring and the silhouette of the channel closures b) Cross sectional SEM image of the monolithically integrated drug delivery channels

4.3 Mechanical performance of Si microprobes

4.3.1 Impacts during medical implantation

During medical implantation, the puncture of dura mater makes great demands on the microprobe itself [4.35]. The possible removal of dura is not preferred since regeneration or local infectious reactions may cause inserted probes to fail. Therefore it is essential to design probe geometries that can withstand the mechanical impact during

insertion and can provide precise drug delivery and/or electrophysiological detection simultaneously as well.

Based on the requirements for puncturing, it seems obvious to design as robust probe as possible to avoid buckling during insertion. This is not as simple, since another dominant implantation parameter dimpling occurs. Dimpling is generally defined as the distance what is covered by the microprobe's tip from touching the surface of dura mater until puncturing that. Dimpling can be considered as a significant issue because of the so-called TBI (traumatic brain injury). TBI leads to cell death in case of traumatic impacts on brain tissue (e.g. compression). When dimpling is relatively great, transport through capillary vessels to cortical cells stops. Since these cells do not have any supplementary resource to function, but only blood, even a short period (1-2min) of circulation disorder results in irreversible damages and poor gain of neuronal activity during electrophysiological measurements [4.36].

If penetration force and dimpling parameters are to be measured, one should know about how the circumstances of measurement affect the collected data.

Conditions of surgery are of key importance regarding the quality of tissue microprobes are facing during insertion. One can conclude that realistic measurements are likely to be resulted from in vivo experiments. In situ and ex vivo implantation significantly decrease force values, giving false impression on the insertion mechanics of microprobes [4.37]. Experiments have also proved that the removal of dura and pia mater also reduces tissue resistance [4.38]; however, because of the above detailed physiological reasons, these layers are left intact during my measurement. As Noort [4.39] and Gefen [4.40] has demonstrated in case of human and rat respectively, the biomechanical behaviour of dura mater is age-dependant. Even one order of magnitude can be the difference in measured force data in rat surgery.

Microfabrication of microprobes can also advantageously affect the implantation parameters [4.41]. The cross-section and tip are the key geometric properties of any realised probe. Generally larger cross-sectional area induces larger penetration resistance of the tissue [4.42], and smaller tip angle makes the insertion easier [4.43], however, mechanical responses show a great variety for different fabrication technologies. Tip angle on the other hand cannot be reduced arbitrarily, since the asymmetry makes the probe deflect as being implanted reducing necessary load to fracture [4.44].

In many cases manual insertion of microprobes is performed, however, a controlled way of implantation can protect tissue from harsh impact [4.45]. Pneumatic [4.46] or spring-loaded [4.47] inserters can provide small load on dura, but they cannot offer further and controlled movement inside the tissue after insertion.

Silicon as structural material is still in the focus of microengineers of neural probes (for more details see previous chapters), however, in spite of the significance of the above issues during insertion, only a few attempt has been made to thoroughly characterise single-shaft silicon probes from the point of view of mechanical loading in vivo [4.38, 4.48].

In my work, silicon microprobes were designed and fabricated with a length covering the possible mammalian applications of the near future. The integration of drug delivery is based on the fabrication method detailed in previous chapters. The mechanical response to axial loading of non-hollow and hollow DRIE etched microprobes and discussion on experimental results is presented in the following chapters.

4.3.2 Experimental methods

Fabrication parameters

The length (1.5-3-5-7cm), width (200 μm & 400μm) and height (200 μm & 400μm) of the sample probes were systematically varied (Fig. 4.17), while the angle of inclination of the tip was kept at 30°. Probe tip of a typical DRIE etched sample is illustrated by Fig. 4.18.

However, the fabrication process is independent from the selection of crystallographic orientation, in order to take advantage of the substrate material regarding the mechanical robustness of the probe as much as possible, all probe shafts were positioned parallel to <100> crystallographic direction along the silicon wafer resulting in maximal Young-modulus [4.49].
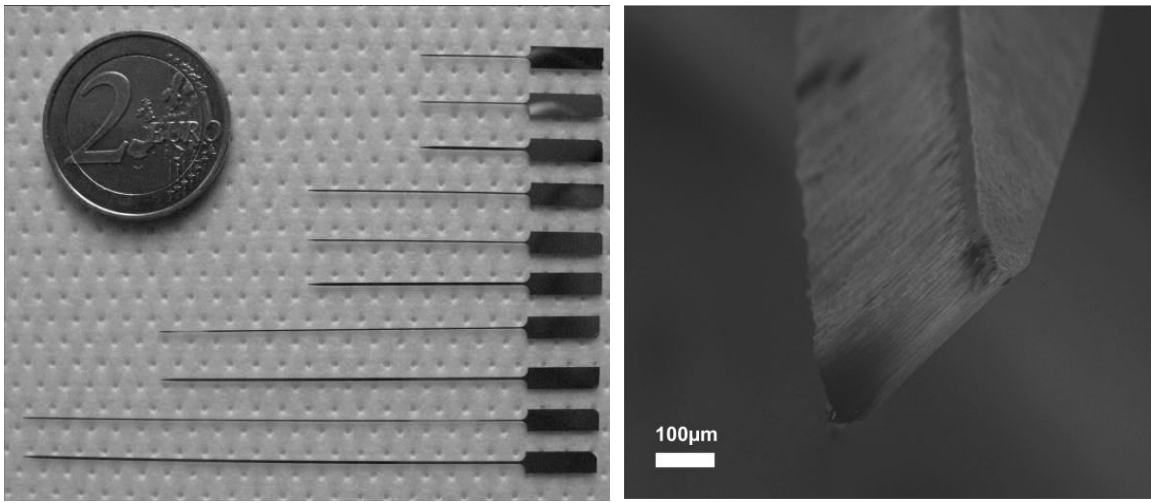
Figure 4.17: Silicon microprobes of several dimensions; length: 1.5-7cm, width: 200-400μm.

Figure 4.18: SEM view of the tip of the realized microprobes.

Notation	Probe width (μm)	Probe thickness (μm)
200x200	200	200
200x400	400	200
400x200	200	400
400x400	400	400

Table 4.2. Description for sample notations.

Fracture test method

The response of the microprobes to axial loading was tested by the experimental setup shown in Fig. 4.19. Probe base was clamped in a fixed position, while the tip was placed in a V-trench fabricated in a PMMA fixture which conveys the force to the measurement system and does not facilitates the sliding of the tip, but allows torsion. In

all direction, micrometer precision racks supported the maintenance of eccentricity during experiments. Loading was monitored by an Andilog CENTOR Force Gauge [4.50] providing 1mN resolution. The final fracture values were derived from the average of at least three consecutive fracture force measurement of probes bearing the same geometric features.

In order to investigate the influence of the integrated microchannels on the mechanical stability of the probe, both non-hollow (as reference) and hollow probe shafts were analyzed.

In order to investigate the influence of the integrated microchannels on the mechanical stability of the probe, both non-hollow (as reference) and hollow probe shafts were analyzed. Optical and electron microscopy was also used to evaluate failure properties.
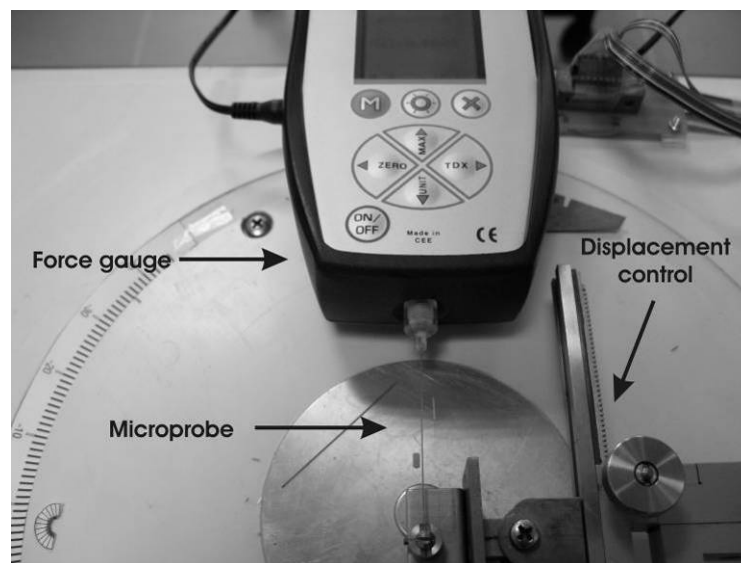
Figure 4.19: Experimental setup for fracture test of silicon microprobes

In vivo method

Seven 3-4 months old Sprague Dawley rats were used for in vivo mechanical experiments. All procedures were conducted according to the Animal Care Regulations of the Institute of Cognitive Neuroscience and Psychology, Research Centre for Natural Sciences, Hungarian Academy of Sciences. A mixture of 37.5 mg/ml ketamine and 5mg/ml xylazine at 0.2 ml/100 g body weight injection volume was applied as initial anesthesia via intraperitoneal injection. Body temperature was maintained at 37 °C throughout the penetration experiments. Animals were mounted in a stereotaxic frame and a 4 mm diameter craniotomy was performed in order to have access to cortex. Dural surface was cleaned by sterile saline and was left intact, and it served as reference point for calculating the penetration depth, which was 3mm throughout all the experiments. We used Bregma for the determination of the anterioposterior and mediolateral locations of the implantations. Implantation sites were chosen such that ventricles were avoided along the implantation tracks. Both left and right hemispheres were used, since both of them are considered similar, regarding tissue mechanics. A maximal number of six insertions from at least 1mm from one another were performed per hemisphere in order to minimize parasitic phenomena. When a depth of 3mm was reached, inserting motion was stopped, and after 1 minute probes were retracted with the same speed as

used for insertion. At the end of each experiment, animals were sacrificed by overdosing the above mixture of ketamine/xylazine.

Microprobes were fixed in a custom-designed holder, which was attached to an Andilog Centor Easy type force gauge (measuring limit: 10N, resolution: 1mN). Finally this setup was mounted on a stereotaxic frame. The vertical position of the probes was adjusted by a Gamma type stepper motor (1.8° step angle). The measurement setup for in vivo insertion is shown in Fig. 1. Stepping units of the motor was 10µm, while stepping precision was 1µm. Data acquisition was performed by a Labview controlled measurement system through a NI digital I/O card by a sampling rate synchronised to the actual stepping frequency of the linear motor. Noise level of the thereby constructed insertion system was found to be approximately 1mN. This noise level is too high to make reliable evaluation in the retraction phase; however, it is sufficiently low to analyze penetration force during tissue puncturing. Insertions were performed at constant speed. Penetration speeds were determined as 1.2, 3, 5.25, 7.5 and 10.5 mm/min. Before each insertion, the probes mounted on the load cell were lowered by 1mm until getting contacted with the tissue surface for baseline recording. The probe tip was considered to reach the surface of dura, when the measured force values exceeded the noise level. Dimpling was measured from this point until the maximal force was applied (penetration force). Buckling of the probes was not observed in the case of any insertion experiments. In each case of geometric variation and insertion speed, at least two insertions were carried out (except for sharpened samples), recorded and evaluated by descriptive statistical methods.
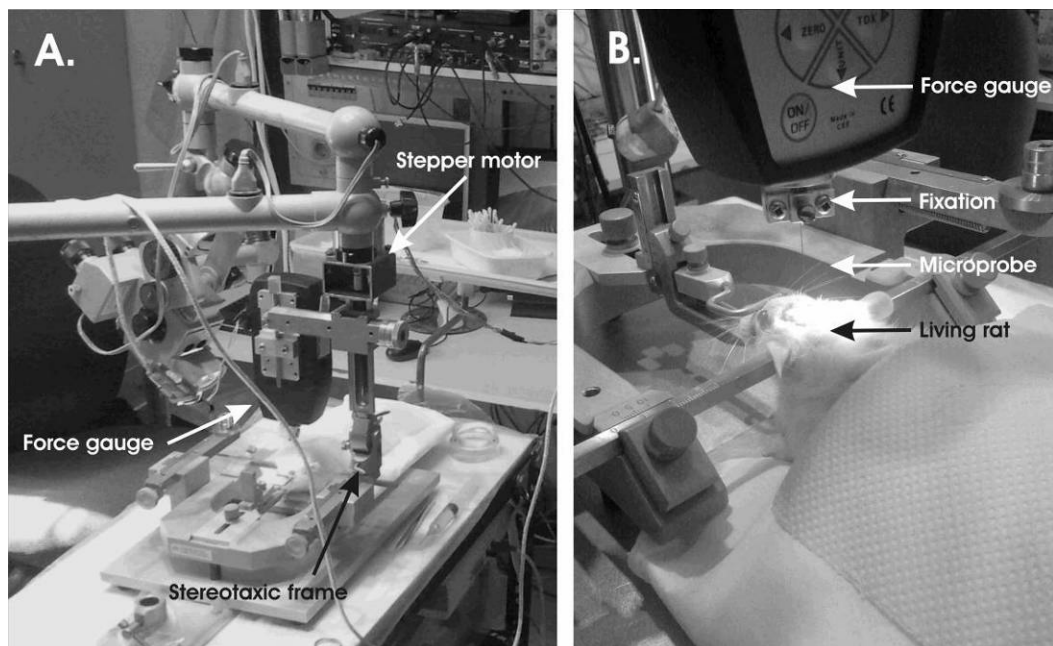

Figure 4.20: Experimental setup for in vivo testing of penetration mechanics

4.3.3. Fracture test results

Characterisation of non-hollow microprobes

Non-hollow microprobes of given cross-sections were tested to see the effect of contour parameters on mechanical behaviour independently from the case involving an

integrated microchannel. The measured fracture forces belonging to the realised probe geometries are shown in Fig. 4.21.
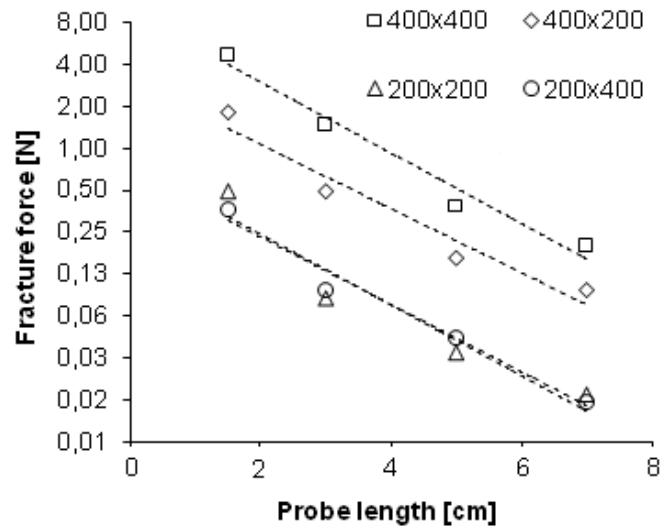

Figure 4.21: Measured fracture plotted against probe length in the case of several cross-sections (width x thickness). The y axis is illustrated by a logarithm (base two) scale.

The measured set of data suggests that increasing one of the cross-section dimension of the probe shaft by n times, the fracture force reduces by approximately n^2 times. Obviously, smaller cross-section means reduced mechanical stability, however, larger amount of measured values are required to make established statements in this regard.

On the other hand, it is apparent that boundary conditions (e.g. fixation of the probes) have an effect on the results, since force values in case of samples '200x200' and '200x400' are in the same range. Moreover, the fracture forces experienced at samples of the same cross-section ('200x400' and '400x200') differ significantly. The above observations suggest that surface area perpendicular to buckling dominates the load bearing properties of the probes.

The measured curves also show that fracture force depends upon the length according to the function $1/x^2$. That suggestion is confirmed by the fitted curve on Fig. 4.22.
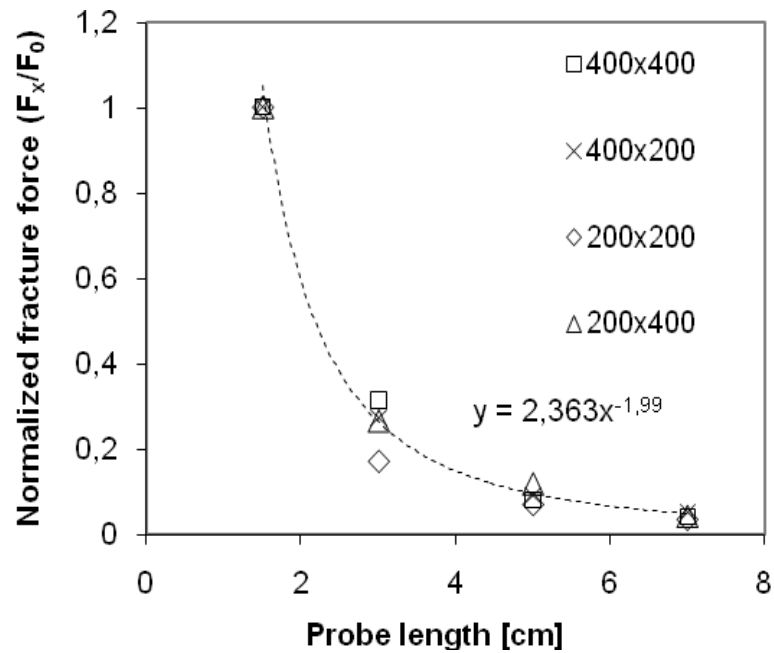
Figure 4.22: Fracture forces normalized according to the greatest measured value of specific cross-section.

Characterisation of hollow microprobes

Hollow probes were also tested under the same conditions as non-hollow ones. Fracture forces for hollow and non-hollow probes with cross-section of '200x400' are presented in Fig. 4.23. The integration of a microchannel significantly deteriorates the robustness of the probe. The micrograph of the microchannel cross-section is illustrated as part of Fig. 4.23. The differences in the measured values are approximately as much as 80% in the case of each probe length.

I noticed that the cross-section ratio of the microprobe and microchannel also affects the results. Microchannels of the same parameters integrated in a microprobe of 400µm x 400µm dimensions cause 2.5-3 times lower deterioration in fracture forces than in the case presented in Fig. 4.22.
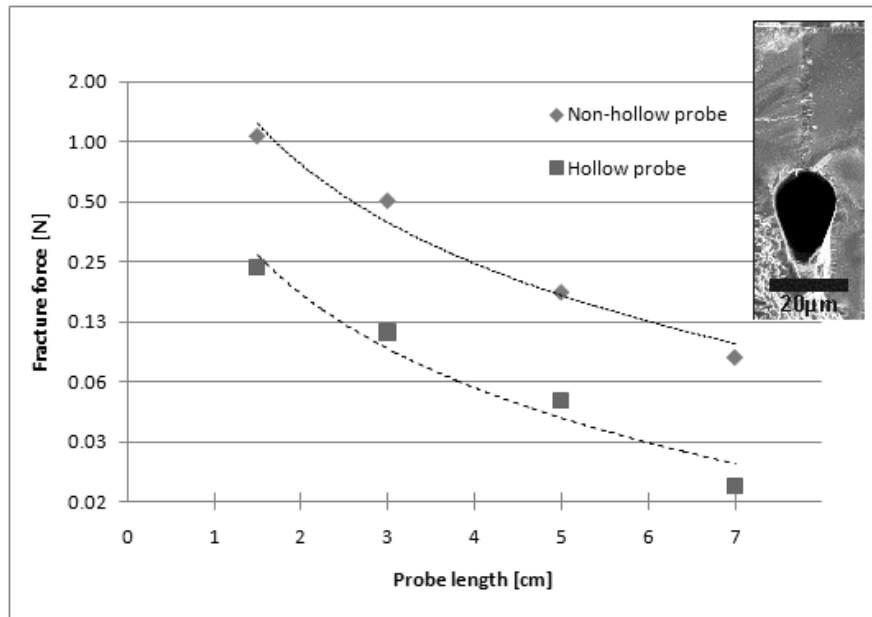
Figure 4.23: Semi-log representation of the comparison between fracture force belonging to hollow and non-hollow probe shaft series. The y axis is illustrated by a logarithm (base two) scale.

A preliminary experiment was carried out to see how the position of microchannel in the substrate influences the vulnerability of the hollow probe. Fig. 4.24 shows the schematic representation of test structures A and B with different microchannel location. According to my results (Table 4.3.), further improvement can be made if the axis of microchannels is moved from the central axis of the probe (by 100µm in my experiment). I suppose that mechanical stresses are concentrated on the edges, therefore mechanical performance of hollow probes can be enhanced if microchannels are placed relatively far from critical edges (e.g. tip) of the shaft.

Probe length (cm)	Non-hollow probe (mN)	Hollow probe A (mN)	Hollow probe B (mN)
1.5	1061	233	773
3	504	150	249

Table 4.3: Fracture forces in case of different microprobe samples (cross-section is 200 µm x200µm). Hollow probe A and B represent samples having a single microchannel in and out of the central axis of the probe respectively.
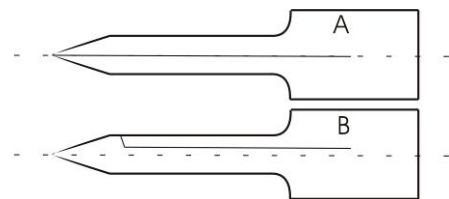
Figure 4.24: Schematic representation of test structures A and B with different microchannel location.

Microscopic analysis

Optical microscopy was used to evaluate the typical failure mode during fracture tests. As expected the fixation of probes did not allow bending caused by lateral or shear forces. According to my observations, the typical failure mode was buckling. Since the tip of my samples is inherently symmetric due to DRIE etching, it is assumed

that conditions would be similar in case of in vivo penetration; however, further analysis is required to prove this statement.

I also analyzed the failure of the probes by SEM cross-sectional views. A typical micrograph on the close vicinity of the microchannel integrated in a probe shaft broken during measurements is illustrated in Fig. 4.25. I noticed that weak points of the system tend to be concentrated at the bottom of the channel. I assume that the change of channel profiles (e.g. circular instead of tapering) may alter the mechanical stability of the hollow probes beneficially. Nevertheless, from the point of view of fluidic functionality, it is also observed that crack generation or propagation along filled trenches is not typical during buckling, which proves the feasibility of my drug delivery integration concept in microprobes even if buckling would occur.
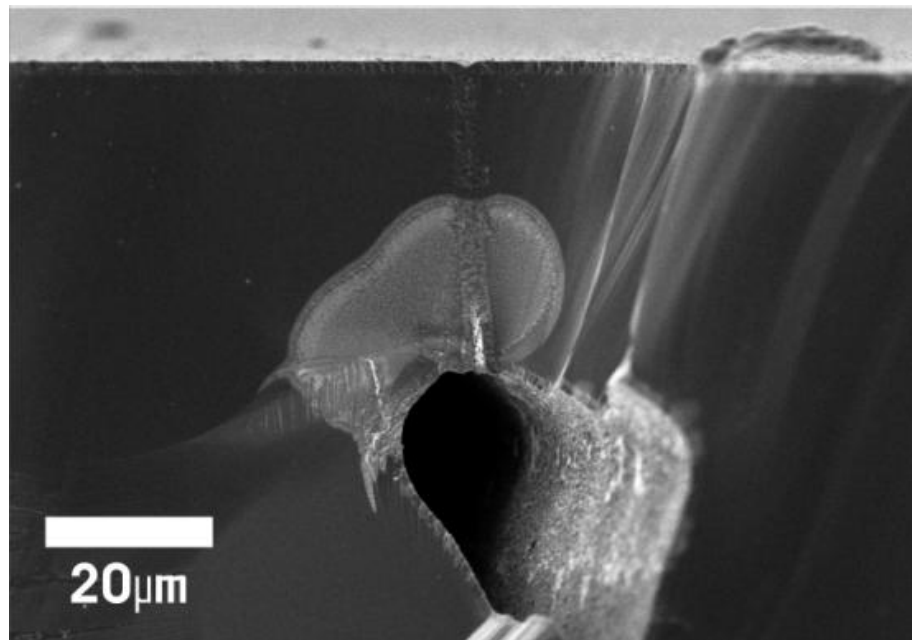
Figure 4.25: Typical surface morphology of a broken hollow microprobe around the sealed channel (SEM view).

Perspectives

Considering the order of magnitude of puncture toughness of the human dura mater [4.39], we concluded that the axial fracture force of my 7cm long hollow probe with the above tip and cross-section parameters is in the same order of magnitude (13mN in my case) as the force necessary to penetrate into the brain tissue through human dura mater. This means that safety margins are getting closer as one is further decreasing the characteristic sizes of a probe fabricated by the proposed technique. In order to have better understanding of the limits of such probes in vivo analysis is recommended.

4.3.4. In vivo results

Apparently, all the tested microprobe geometries are more robust than it is required in case of rat surgery and implantation, however, larger cross-sections produce larger force and dimpling values through rat dura mater and therefore a more objective comparison

can be made well above the noise level of our measurement setup. Nevertheless, it must be emphasized that the following results and relationships are valid only in the investigated insertion speed range and in the case of actuation by a stepper motor.

A representative recorded force vs depth curve is shown in Fig. 4.26. Relaxation phase shows additional small peak loads, which can be attributed to the increasing interfacial area of the probe being in contact with the surrounding tissue. These rest forces were consequently experienced, however, not explained here in details, since they were still detected in the close vicinity of the noise level of the measurement setup.
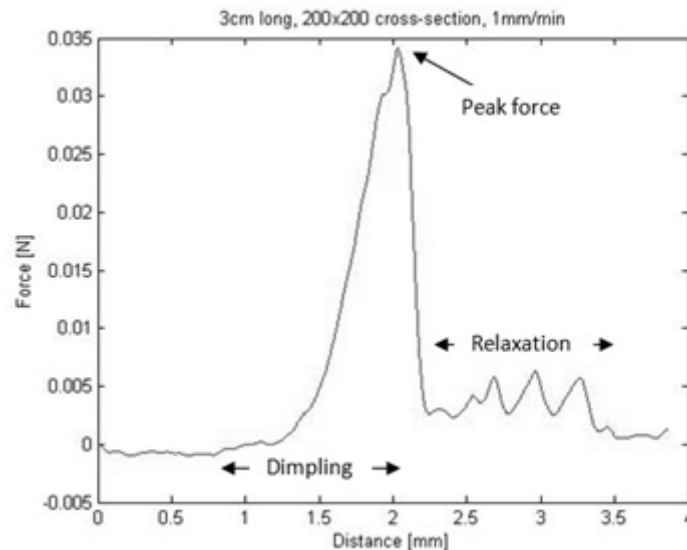
Figure 4.26: A representative measured force-distance curve before signal processing at an insertion rate of 1.2mm/min.

It was observed that the actual mechanical behaviour of the cantilevers is remarkably sensitive to the stepping frequency of the linear motor and in some cases the resonant vibrations of the microprobe tip reduces both penetration force and dimpling during insertion. Due to the presence of resonant modes, a lower mechanical response is experienced, which can be clearly seen in Fig. 6. Tip oscillations of long probes at certain speeds is inevitable, however, it can be eliminated by the precise selection and adjustment of insertion speeds (stepping frequencies) which are out of resonant modes of the microprobe. On the other hand, the geometric parameters of our long probes show such a great variety that it would be a great deal to avoid the presence of the first, second or third mode in every single case (insertion speed vs sample cross-section). Nevertheless, outstanding data points attributed to tip vibration can be clearly indentified and we found that trends can be still obviously determined.
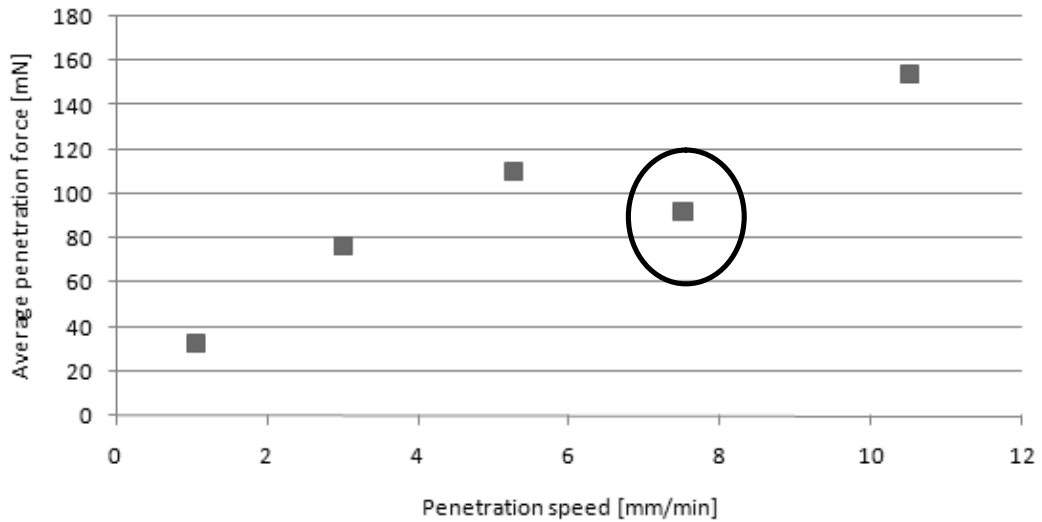
Figure 4.27: Error assigned to resonance generated by the stepper motor (probe cross-section: 400μmx400μm)

Penetration force was analysed at several probe cross-section (see Fig. 4.28). It was concluded that increasing the insertion force a gradually increasing penetration force is acting on the probe tip. Regarding microprobe geometry, samples of higher interfacial area resulted in higher penetration force. The above experiences are in well agreement with results published elsewhere [4.42].
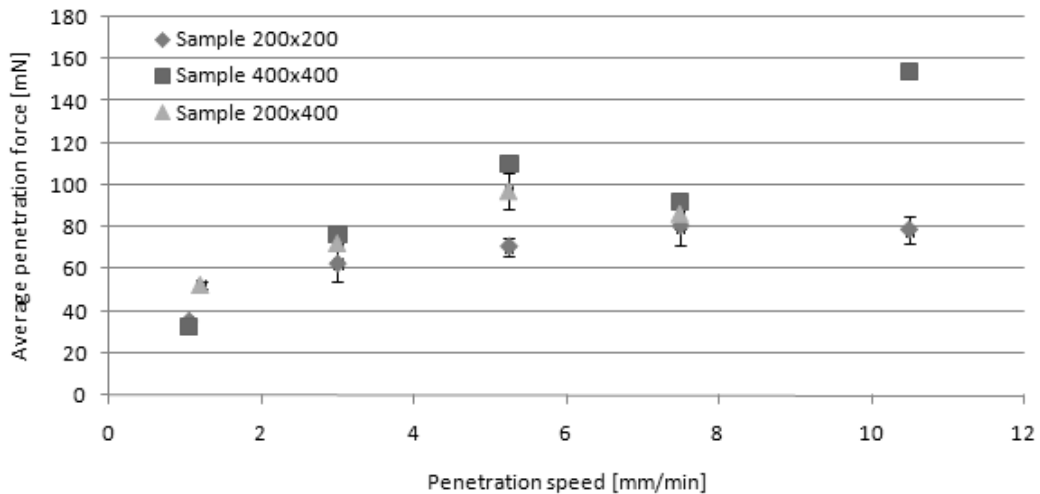

Figure 4.28: Penetration force plotted against penetration speed of the microprobes

Dimpling was also determined from the measured force-depth curves and was plotted against insertion speed. Data are presented by Fig. 4.29. Characteristic dependance of dimpling on speed was not observed, however, probes with larger interfacial area produced higher dimpling. It should be noted that pneumatic [4.45] or spring-loaded [4.46] insertion devices provide much lower dimpling, but their regime of implantation speed is far more exceed that of the hereby proposed setup.
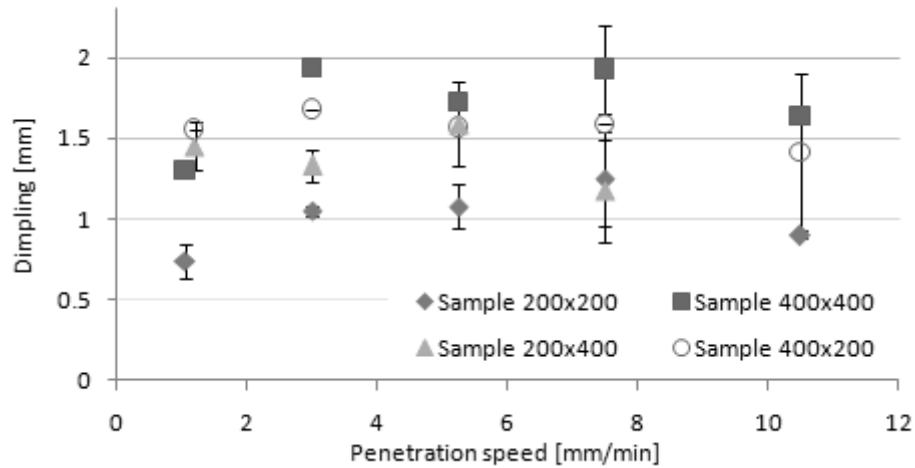
Figure 4.29: Dimpling of microprobes plotted against insertion speed

Since dimpling did not show any consistent relationship with speed in the analyzed regime, an average value for each probe geometry was derived and compared (Fig. 4.30). A clear tendency shows that interfacial area of the microprobe has a significant effect on the expectable dimpling. Difference in behaviour between samples denoted by 200x400 and 400x200 suggests that length of the cutting edge tailors the extent of exerted pressure in case of probes of similar cross-section.
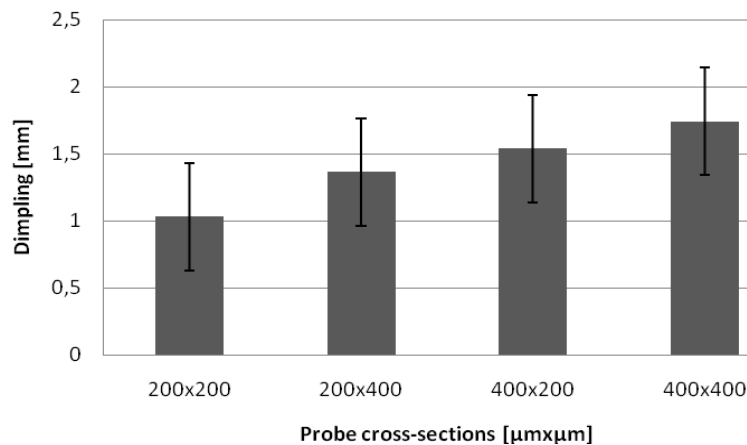
Figure 4.30: Dimpling of microprobes of different cross-section

Finally, a brief comment on the influence of geometric properties on fracture force and penetration force can be made. Based on fracture tests and in vivo experiments a relative decrease of forces is illustrated by Fig. 4.31. However, a decreasing size of probe contributes to a moderately smaller penetration force; the axial load the probe can withstand decrease more drastically by the cross-section.
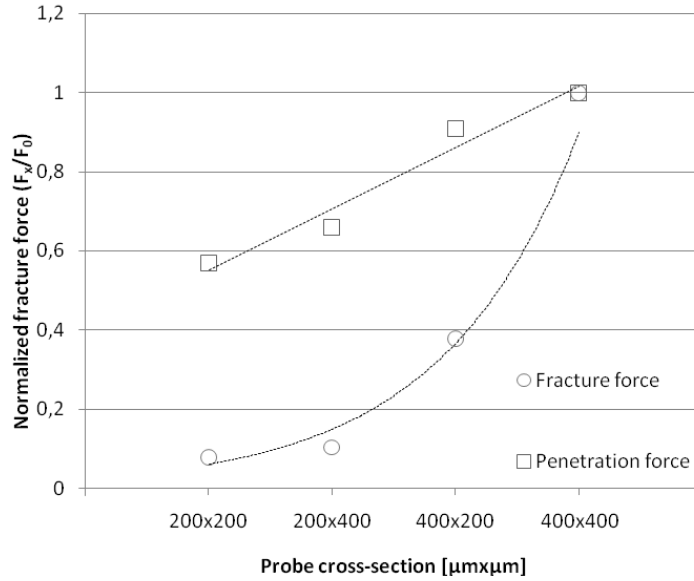
Figure 4.31: Change of penetration force and fracture force at an insertion speed of 3mm/min

4.4. Characterisation of integrated drug-delivery system

4.4.1 Terminology

The pressure-driven, steady-state flow of an incompressible Newtonian fluid through a straight channel is referred to as Poiseuille flow. It is well known that constant pressure drop Δp results in a constant volumetric flow rate Q. Relationship can be summarized in the Hagen–Poiseuille law [1.8], which is analogous to Ohm's law $\Delta V = R\,I$, relating the electrical current I through a wire with the electrical resistance R of the wire and the electrical potential drop ΔV along the wire.

$$\Delta p = R_{hyd} \cdot Q \qquad (4.1)$$

The proportionality factor R_{hyd} is known as the hydraulic resistance. The concept of hydraulic resistance is central in characterizing and designing microfluidic channels in lab-on-a-chip systems. The mathematical expression for the flow rate through an arbitrary shaped microchannel derived from Navier-Stokes equation is as follows [1.8]:

$$Q = \frac{1}{\gamma} \cdot \frac{\Delta p}{2\eta L} \cdot \frac{A^3}{P^2} \qquad (4.2)$$

where A is the microchannel cross-section, P is the wetted perimeter, L is a length scale characteristic of the flow, and η is the dynamic viscosity. Numerical calculations have revealed that the infinite sum is very close to 1/8 for a wide range of shapes and exactly equal to this number for the circular cross-section. A factor of 8 is therefore

47

introduced and the resulting dimensionless sum is denoted $\gamma-1$. The flow behaviour in microchannels is often qualified by the Reynolds number [1.8], which is given by:

$$\text{Re} = \frac{\rho \cdot u \cdot L}{\eta} \qquad (4.3)$$

where u is some velocity characteristic of the flow, and ρ is the density. The physical significance of the Reynolds number is that it is a measure of the ratio between inertial forces and viscous forces in a particular flow. The different regimes of behaviour are:

• Re < 2300: viscous effects dominate inertial effects (flow is laminar)
• 2300 < Re < 4000: viscous effect comparable to inertial effects (vortices appear);
• Re > 4000 inertial effects dominate viscous effects (turbulence occurs).

4.4.2 Experimental methods

p-Q measurement setup

The microprobes were validated fluidically by attaching silicone tubing to the in-plane fluidic ports. The tubes were connected to an isobar-pump, which served constant flow of deionised water. Pressure range up to 250kPa has been applied, while microchannel outlet was sampled by micropipettes. The volumetric flow rate was derived from the collected amount of sample and time required. The microfluidic interface to the microprobe is illustrated by Fig. 4.33. The leak-free pressure range of the hollow microprobe was also tested.
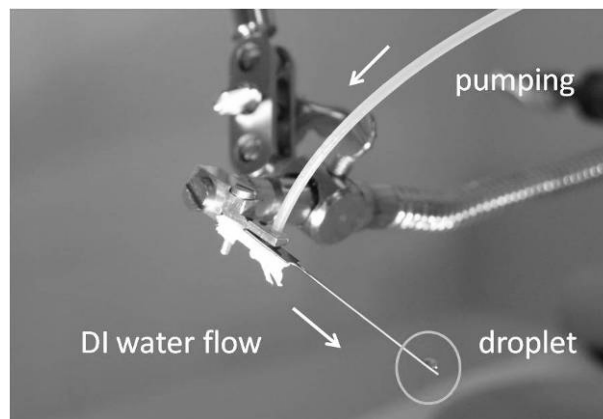

Figure 4.33: Pumping DI water through the integrated drug delivery channel

In vivo measurement setup

A 30mm long, 200μm thick, 400μm wide probe with a single buried channel along its shaft has been applied for performing preliminary in vivo measurements in the Comparative Psychophysiology Lab of the Hungarian Academy of Sciences. All procedures were conducted according to the Animal Care Regulations of the Institute

for Psychology of the Hungarian Academy of Sciences. The effect of pyrrolidine-2,4-dicarboxylic acid (PDC) on neural activity in rat hippocampus has been studied. Application of PDC can enhance gamma oscillation (25-100 Hz) through such effects as inhibition of glutamate uptake [4.51] and stimulation of glial glutamate release [4.52].

A 300 g male Wistar rat has been anesthetized with a 0.6 ml mixture of 37.5 mg/ml ketamine and 5mg/ml xylazine, its sleeping state maintained by 0.2 ml/h updates of the same solution. The Si-based probe with the buried channel, releasing PDC has been implanted into the hippocampus, 3.0 mm posterior and 3.2 mm lateral from the bregma, with an angle of 10°. In the opposite hemisphere, a 16-channel wire electrode (site distance: 100 μm) has been used for signal recording (Fig. 4.34). Rat hippocampi are strongly connected with each other, therefore changes of their activities can be monitored from the opposite one. Illustration of the measurement setup during surgery is illustrated by Fig. 4.35.
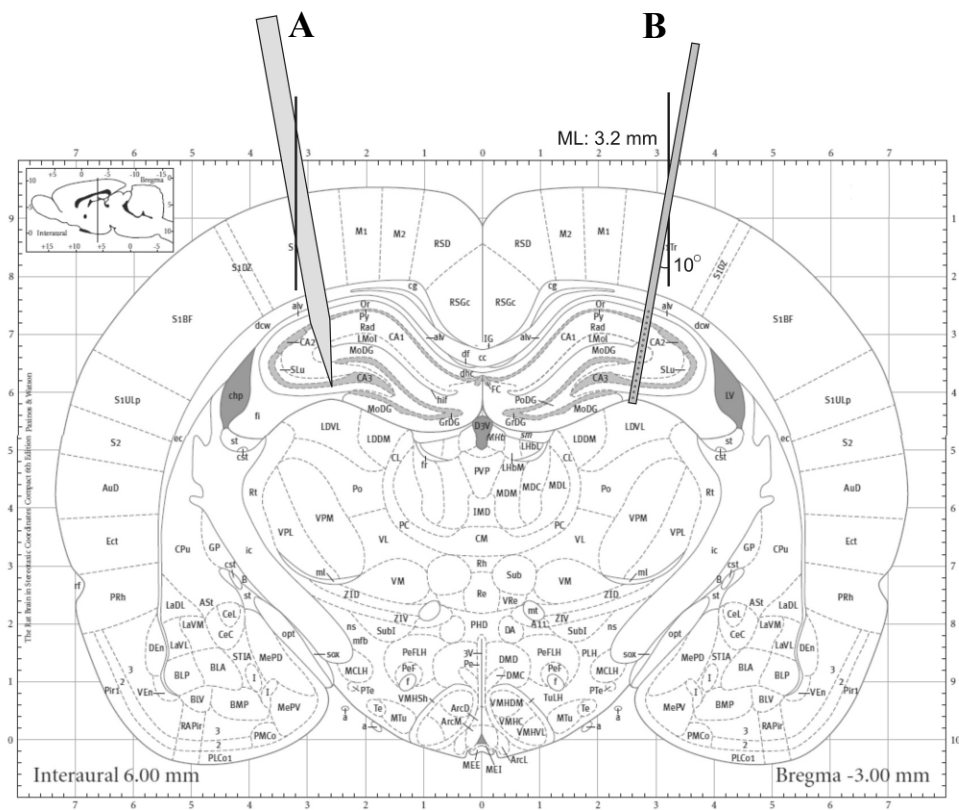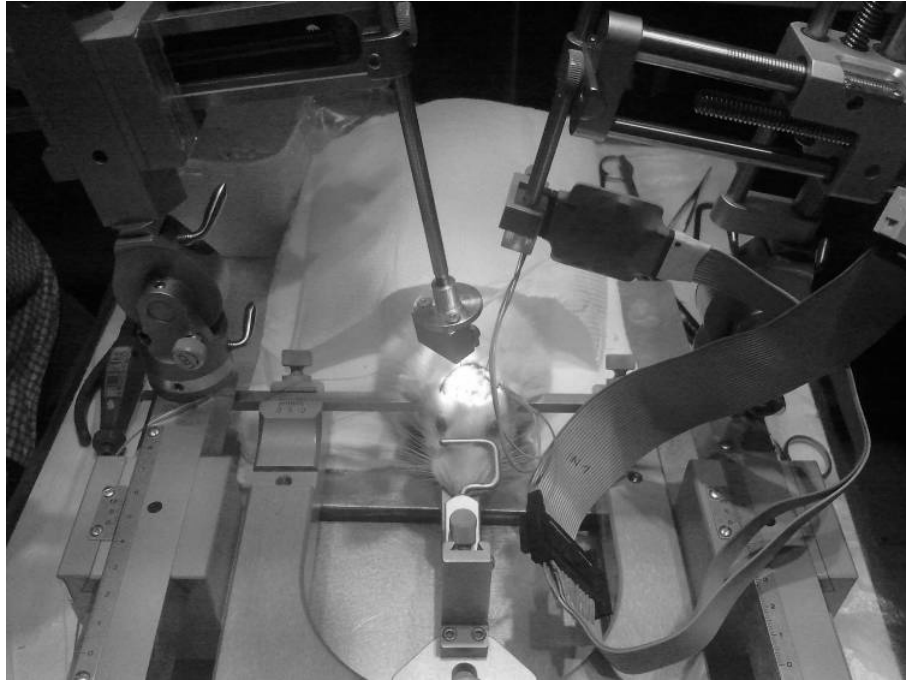

Figure 4.34: Targeted locations of the implants: a Si-based probe with buried channel (A) with a 16-channel wire electrode (B). Based on Figure 58 of [4.53].

Figure 4.35: Experimental setup of hollow microprobe testing

4.4.3 Hydrodynamic characterisation

Hydrodynamic characterisation of hollow microprobes has been carried out and fluidic transport through buried microchannels was successfully demonstrated (see Fig. 4.36).
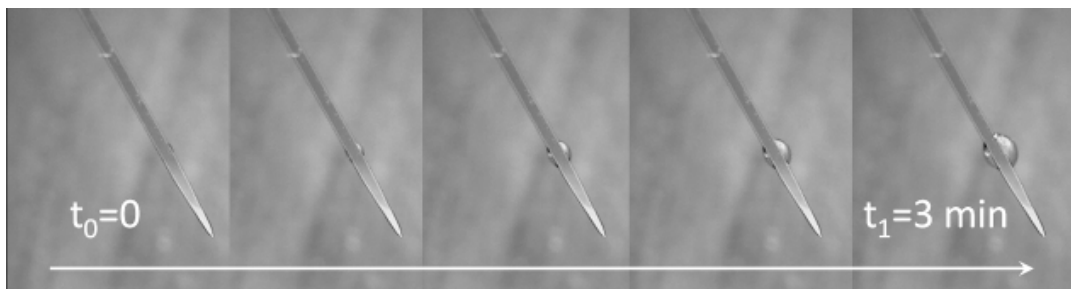
Figure 4.36: Sequential photograph of a delivery of deionised water through the sealed microchannels integrated in the microprobes.

A representative measured p-Q function is shown in Fig. 4.37. As expected from laminar flow theory, the flow–pressure relationship is linear. Measured flow rate values slightly differ from calculated ones.
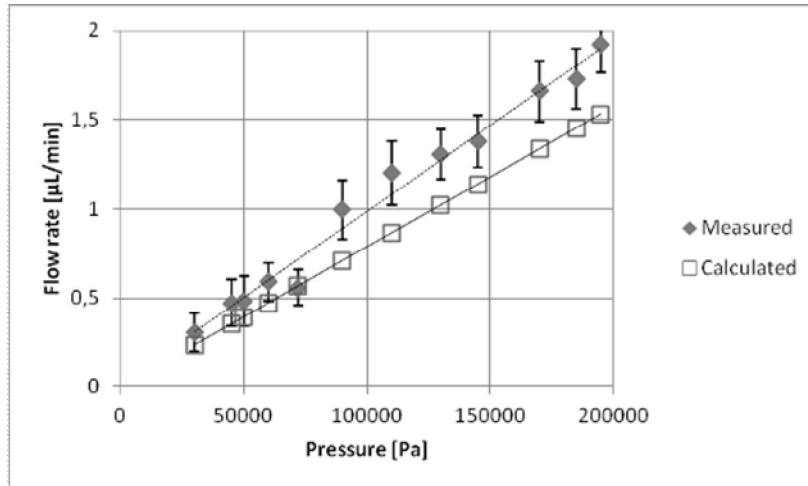
Figure 4.37: Representative pressure-flow rate characteristics. Linear curve is fitted to calculated valuesderived from Eq. 4.2.

Typical flow rates for neuroscience applications are summarized in Table 4.4 including literature references.

Author	Flow rate [μL*min−1]	Pressure [kPa]
Seidl [4.54]	1.5	1
Chandrasekaran [4.55]	16.7	30
Cheung [4.56]	50	260
Fernandez [4.57]	11.7	60
Ziegler [4.58]	0.2	1
Zahn [4.59]	0.7	137
Own result	1	85

Table 4.4: Hydrodynamic properties of hollow microprobes in the literature

In order to see the extent of laminarity in my system, Reynolds-numbers derived from Eq. 4.3 were calculated in the investigated pressure range. According to the values represented in Fig. 4.38, flow is apparently laminar in the whole regime as expected.
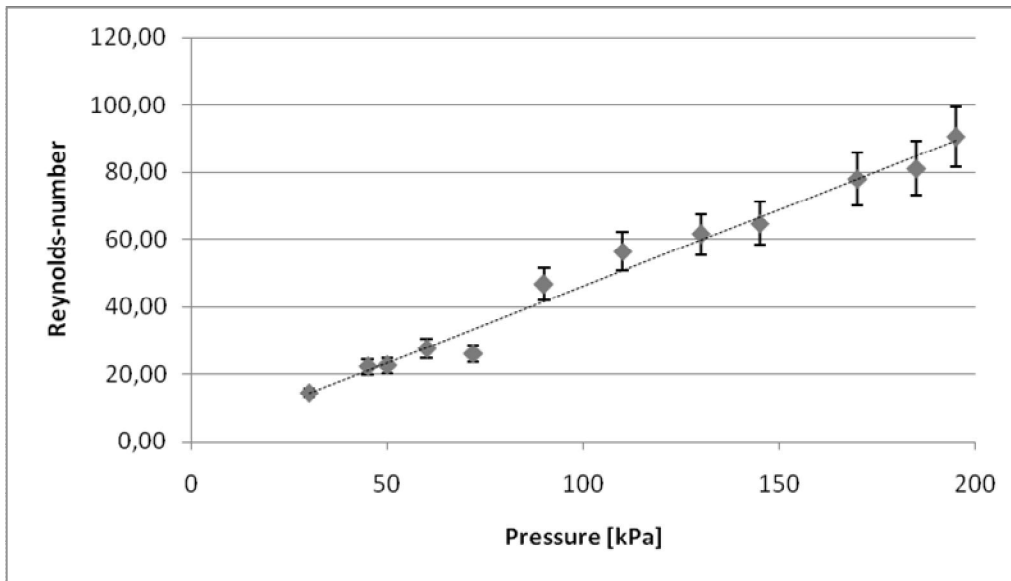
Figure 4.38: Reynolds-number plotted against exerted pressure.

My fluidic microprobes are found to be gas tight up to a pressure of at least 400kPa, which is generally sufficient in neural applications. A typical leakage above this pressure is illustrated by Fig. 4.39. However, further improvement can be made if additional thin films (insulation and conduction layers) are also present and considered.

Figure 4.39: Typical leakage through poly-silicon orifice above the critical pressure.

4.4.4 In vivo results

Signal characteristics monitored in sleeping state suggest that channel 7-13 were located in the hippocampus (Fig. 4.40). Applying fast Fourier transform (FFT) on channel 10, a slight increase of the amplitudes of gamma waves after PDC injection can be observed (Fig. 4.41).
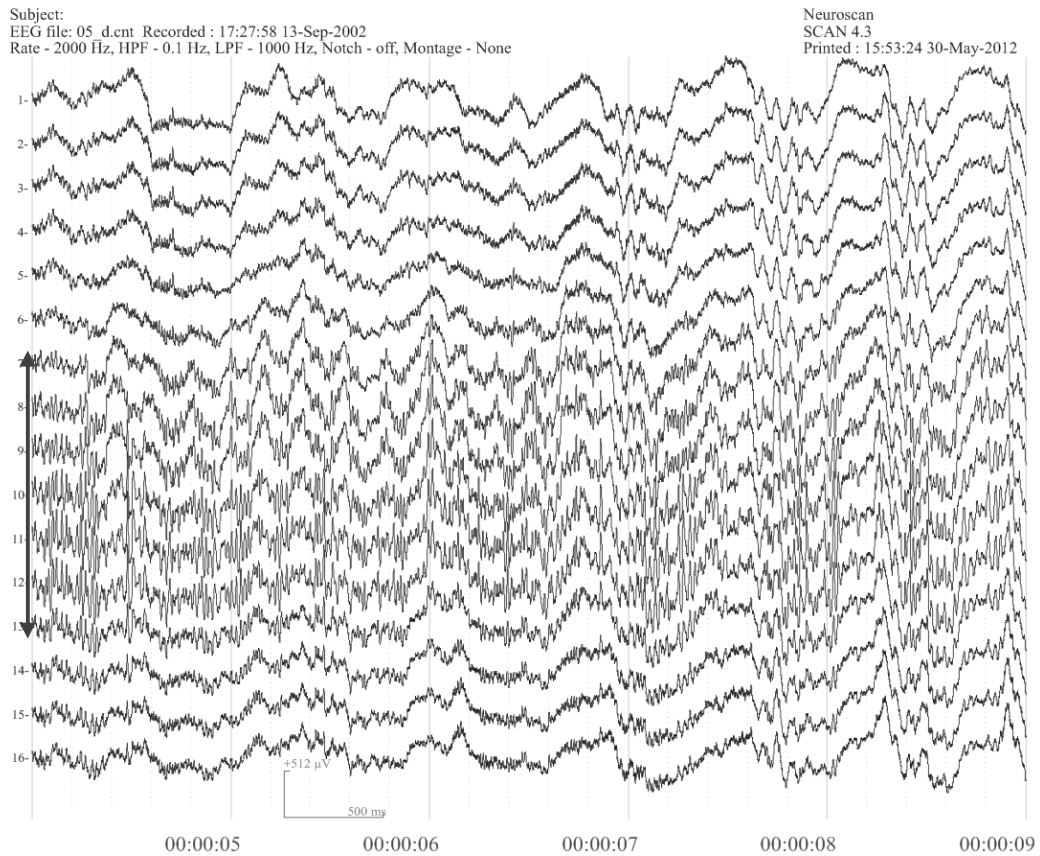
Figure 4.40: Hippocampal recordings on channel 7-13, with 25-100 Hz gamma-waves
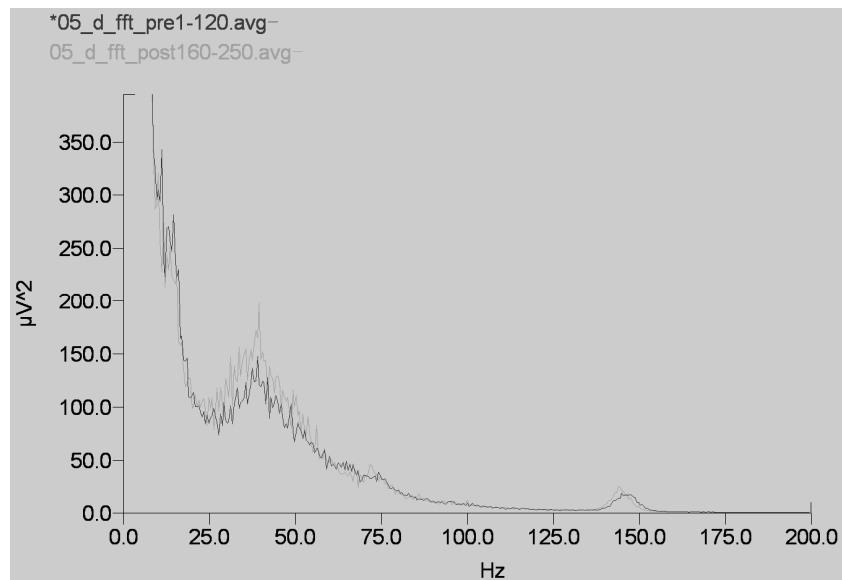

Figure 4.41: Frequency analysis of signals recorded before (green curve) and after (red curve) PDC injection.

The performed in vivo test proved that the fabricated hollow microprobes are applicable as drug delivery devices in medical implants; however, further studies are essential to be carried out in order to reveal the parallel use of fluidic and electrical functionality of my proposed microprobe.

53

5. Development of sample preparation microfluidic system

5.1. Recent advances in microscale blood separation

5.1.1. Overview of blood separation methods

A significant number of clinical tests is aimed to quantitatively or qualitatively analyze the presence of proteins, ions, crystalloids or diluted gases in human blood [5.1]. In this case, the presence of blood cells in the sample could be a serious drawback, so the first stage of the tests must be the separation of plasma or serum from the whole blood [5.2-5.5].

Two significant parameter conventionally used for performance characterization are separation efficiency (SE) and purity efficiency (PE). These terms are defined as follows.

$$SE = \frac{V_{plasma}}{V_{plasma} + V_{cell}} \tag{5.1}$$

where V_{plasma} is the volume of sample liquid flowing through the plasma branch of a bifurcation, and V_{cell} represents the collected sample from the main channel.

$$PE = 1 - \frac{C_{plasma}}{C_{in}} \tag{5.2}$$

where C_{in} and C_{plasma} are the concentrations of particles in the inlet and plasma branch respectively. The efficiency of the separation is quantified by Eq. 5.2.

The conventional method for blood plasma separation is the centrifugation, a technique widely applied in the clinical practice. Several researchers have aimed to integrate this function into the sample preparation cartridge of the bioanalytical devices via miniaturisation [5.6-5.7]. The centrifugal methods (Fig. 5.1.a) have the advantage of high separation efficiency and purity(> 90%), but the disadvantage of using moving parts. A modified version of this method could be adapted at the microscale where the cells are separated in bending or spiral channels due to the Coriolis-force and diverted by a junction [5.8]. Disadvantage of this method is the possible haemolysis due to the high shear-forces or the sharp edges of the junction and the possible mixing due to the Dean-vortices evolving in case of higher flow rates.

In the literature two different methods were described using conventional filtration: "dead end" and "cross-flow" filtrations. In case of the "dead end filtration" (Fig. 5.1.b) PE is excellent, but the amount of the resulted plasma is weak (~20µL) due to the quick blocking of the filter [5.9]. The "cross flow filtration" (Fig 5.1.c) can solve the problem of the blocking, PE (100%) is high, but the SE parameter is around 1%. [5.10].

The combination of the dielectrophoretic (Fig. 5.1.d) and capillary phenomena was applied by Nakashima for blood plasma separation [5.11]. They demonstrated the applicability of the method achieving 6% SE and 97% PE during the separation of 300nL plasma from the initial 5µL blood drop.

The blood plasma separation method based on the Zweifach-Fung hydrodynamic effect was also characterised and 25% SE and 100% PE were achieved applying adequate flow rates [5.12-5.14]. The basic phenomena could be supplemented by the axial migration effect which resulted in higher SE (~40%) and moderate PE (~50%) [5.14]. The relevant literature is summarized in Table 5.1.
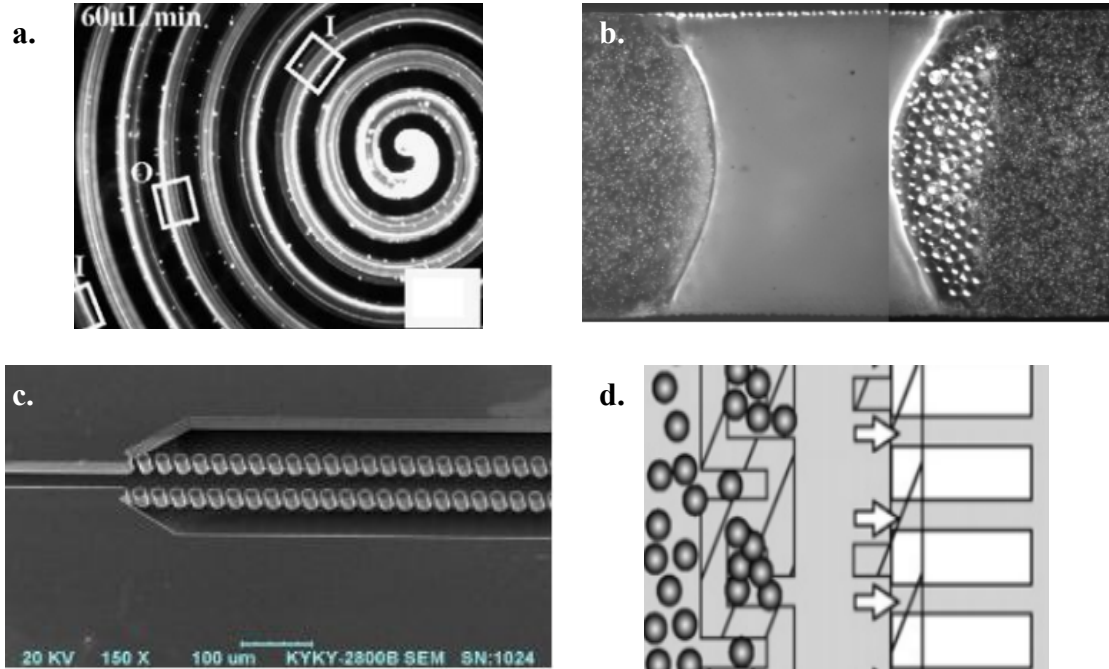

Figure 5.1: Centrifugal method (a.) [5.8], dead-end filtering (b.) [5.9], cross-flow filtering (c.) [5.10] and dielectrophoretic actuation (d.) [5.11] for particle separation.

Author	Principle	PE [%]	SE [%]	v [μL/min]	Blood sample	H [%]
Haeberle [5.6]	Centrifugal	99	88	N/A	human	45
Zhang [2.15]	Centrifugal	90	22	N/A	human	6
Blattert [5.7]	Centrifugal	90	3	1200	human	5
Sollier [5.8]	Coriolis force	99	11	100	human	2
Moorthy [5.9]	Dead-end filt.	100	90	10	rabbit	2
Crowly [5.10]	Cross-flow filt.	100	1	N/A	human	45
Nakashima [5.11]	Dielectrophoresis	97	6	N/A	human	4.5
Yang [5.12]	Zweifach-Fung	100	25	3	sheep	5
Kersaudi-Kerhoas[5.13]	Z-F. + axial migr.	53	40	167	human	3

Table 5.1: Summary of experimental works on blood plasma separation.

One can conclude that the most promising methods for on-chip plasma separation could be the centrifuging (Coriolis-type) or the Zweifach-Fung separation regarding the purity, efficiency and the possible adaptation at the microscale.

5.1.2 Principle of Zweifach-Fung separation

Utilizing the Zweifach-Fung effect the blood cells can be transported separately from the plasma. This effect was described by Zweifach [5.15] and Fung [5.16] and observed in microvascular vessels (see Fig. 5.2). Although the phenomenon has been successfully used in a wide range of micromachined lab-on-a-chip device, there is still no consensus on the explanation of the principle in the scientific community.
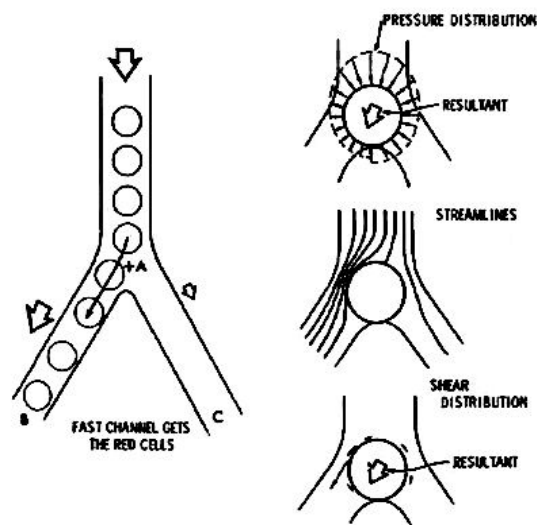

Figure 5.2: Original illustration and explanation of the separation phenomenon by Fung [5.16].

According to the original theory, there is an attraction towards the higher flow rate branch of a microscale bifurcation, which was first described when investigating the flow in blood vessels of different diameters. According to the Bernoulli-law the pressure is lower in the regions with higher flow rates, so the pressure gradient points to the central line of the capillary. In the close vicinity of the bifurcation, blood cells are generally forced into the channel of higher flow rate. The shear forces aroused are also considered as a major component of the Zweifach-Fung effect. The asymmetric distribution of shear forces on the surface of the cell produces a torque on the cell, which drives cells towards the higher flow rate branch of the bifurcation. Eventually, it is supposed that the higher the flow rate ratio between the two branches of the bifurcation is, the higher the purity efficiency of the sample analyte is. A typical realization is shown in Figure 5.3.
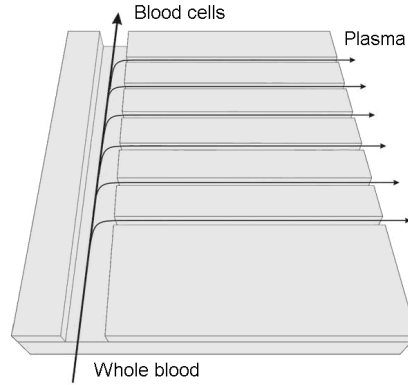
Figure 5.3: Schematic view of the blood separation cascade test structure.

Based on the results of recently implemented simulations and experiments, a new explanation is proposed. The detailed description and arguments are summarized in the work of Doyeaux [5.17]. According to the novel view the initial distribution of cells in the inlet channel has the major influence on the purity efficiency of the separation. As Fung has also reported in his previous work [5.16], a cell-free layer already exists, when particles get to the bifurcation. In the blood circulation system it is also called as plasma skimming. Doyeaux et al. has shown that a depletion of cells due to skimming drives cells to the high flow rate branch at a so-called stagnation point in the bifurcation, however, a migration towards the low flow rate branch is dominant, when cells are approaching the bifurcation from the inlet.

5.2. Characterisation of Zweifach-Fung separation method

However, a number of groups have applied the Zweifach-Fung separation method in a microdevice, none of them has characterised thoroughly the influence of geometric properties of a single bifurcation experimentally and no suggestion has been made for microsystem designers.

In my work, different test structures relying on the Zweifach-Fung plasma filtering method were designed and realised, and the influence of geometric parameters (like channel width, flow rate ratio and bifurcation angle) on both PE and SE features of separation was investigated.

5.2.1. Experimental methods

Design

A range of test structures containing various single bifurcations were designed to evaluate the resulted sample purity and the separation efficiency of Zweifach-Fung plasma filtering method in Si-glass heterostructures. The geometric parameters such as channel width, length and depth were sized to eventually adjust the hydrodynamic

resistance of each microchannel and form specific flow rate ratios between cell and plasma branches.

The hydrodynamic resistance, R of a given microchannel can be calculated by Eq. 5.3 [5.18] in the case of a rectangular cross-section, where the channel depth, width are length indicated by *a*, *b* and *L* respectively, and η indicates the dynamic viscosity of the liquid.

$$R = \frac{12 \cdot \eta \cdot L}{a^5 \cdot b} \cdot \left(1 - \sum_{n=1,3,5...}^{\infty} \frac{192 \cdot a}{n^5 \pi^5} \cdot \tanh \frac{n \cdot \pi \cdot b}{2 \cdot a} \right)^{-1} \tag{5.3}$$

The channel depth is assumed to be 10µm. Bifurcation branches of two different widths is applied. Both of them are comparable with the size of test particles, and therefore the final hydrodynamic resistance of microchannels can be adjusted on the test chip by the microchannel length only. Varied parameters are summarized in Table 5.2.

Side channel width (µm)	10 & 15
Main channel width (µm)	25 & 37
Hydrodynamic resistance ratio (Rp / Rc)	1:2, 1:4, 1:6, 1:8, 1:10
Bifurcation angle (°)	30, 45, 60, 90

Table 5.2: Varied parameters of the filtering structures.

The influence of bifurcation angle was also analyzed experimentally, although only in the case of a specific hydrodynamic resistance ratio of 1:8. The four different angles designed are illustrated by the microscopic view of realized microstructures in Figure 50.
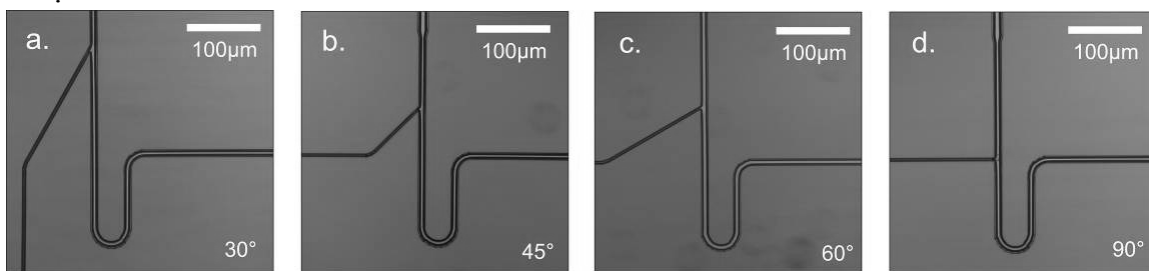

Figure 5.4: Filtering test structures with different bifurcation angles (30° - a, 45° - b, 60° - c & 90° - d) fabricated in silicon. The input stream is to be considered from the top in each microscopic view of the bifurcations.

Fabrication

The microfluidic test chip was realized by silicon & glass micromachining utilizing conventional steps in MEMS manufacturing. The schematic view of the fabrication process is shown in Figure 5.5.
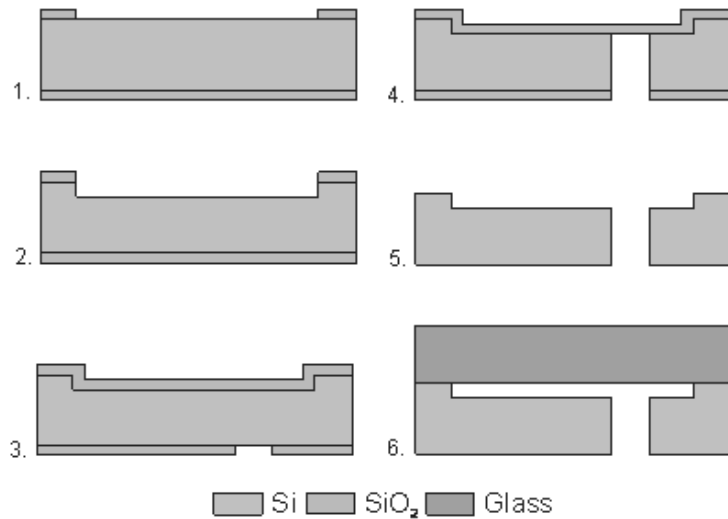
Figure 5.5: Process flow of microfluidic test chip fabrication.

First, a <100> single crystalline silicon wafer is thermally oxidized (thickness: ~ 1µm) and patterned by conventional photolithography (step 1). The microfluidic channel system of the separation chip defined by the masking oxide windows is etched by the Bosch-process of deep reactive ion etching (DRIE, see step 2). Dry etching parameters are the same as detailed in the second column of Table 4.1. A subsequent thermal oxidation and patterning are performed on the backside of the wafer (step 3) in order to fabricate fluidic bores (inlets & outlets) connecting to the front-side microchannels by DRIE again (step 4). After the removal of silicon-dioxide in buffered HF solution (step 5), the front-side of the silicon wafer is anodically bonded to a borosilicate glass substrate which serves as a sealing layer on top of the microfluidics (step 6).

A representative SEM micrograph of a DRIE etched bifurcation is illustrated in Figure 5.6. The small scalloping (~ 100-200nm) of the Bosch-process is apparent, however, it is ignored during both the design and the simulation phases.
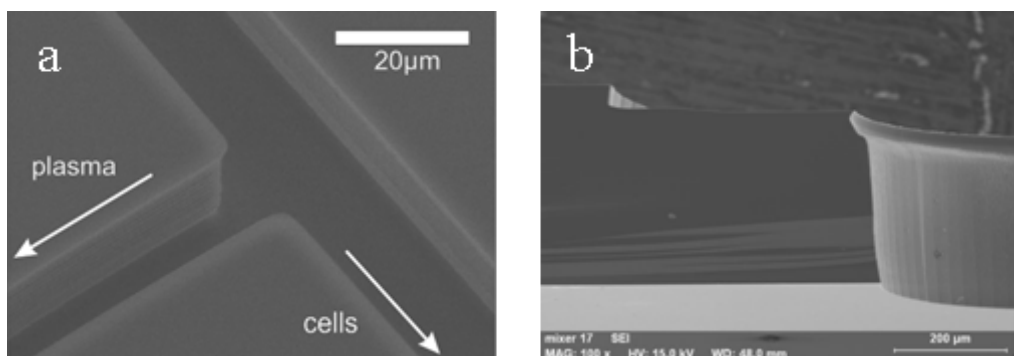

Figure 5.6: SEM view of a bifurcation (a) and the cross-section of the fluidic bore (b) in silicon fabricated by deep reactive ion etching.

Measurement

The silicon-glass microfluidic chips were precisely designed such that they can be functionally tested in the microfluidic platform of Micronit Microfluidics [5.19]. Inlets of the filtering test structures were connected to a syringe pump, and a continuous flow of fungi dispersed in a water-based buffer solution is driven through the microchannel systems. The average diameter of the slightly deformable fungi is around 5µm close to the dimension of red blood cells. The haematocrit level of the solution is estimated to ~ 1%. It was noted by Zhang [2.15] that SE deteriorates proportionally to an increasing haematocrit level, therefore we applied low concentrations. The plasma concentration of such diluted sample was applied as initial parameter for calculating PE and SE. The flow rate of the solution was 30µL/min, which implies a Reynolds number well below one. A typical stream of dispersed fungi solution is shown by an optical microscopy view in Figure 5.7.

A simple Bürker chamber was used to evaluate the concentration of solutions in both inlet and outlet reservoirs. The outlet volume of each branch was measured by micropipettes of µL resolution.
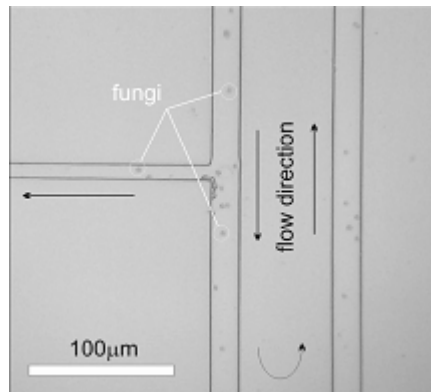
Figure 5.7: Particle transport in the microfluidic channels, representing the separation effect.

Modelling

The flow conditions in the vicinity of the bifurcations were analyzed by Finite Element Modelling using COMSOL Multiphysics [5.20] solving the Navier-Stokes equation. Boundary conditions on the wall were set to no-slip, and average velocity of the Newtonian fluid (water) from the inlet was defined as 2m/s. Flow was assumed as laminar in the channel system. Outlet pressure was 0 Pa. The angle of bifurcation was varied (30°, 45°, 60° & 90°) and velocity field distribution and pressure conditions were examined right before the bifurcations. The hydrodynamic resistance of the channel branches were adjusted such that fixed volumetric flow rate ratio (1:8) between bifurcation vessels was sustained.

5.2.2. Performance of single bifurcations

Flow rate characterisation

Before further analysis of each realized test chip, the exact flow rate ratio between bifurcation branches was measured (see Fig. 5.8). One can conclude that the measured ratio is definitely greater in each case than the designed values which are getting more remarkable as the designed resistance ratios are increasing.
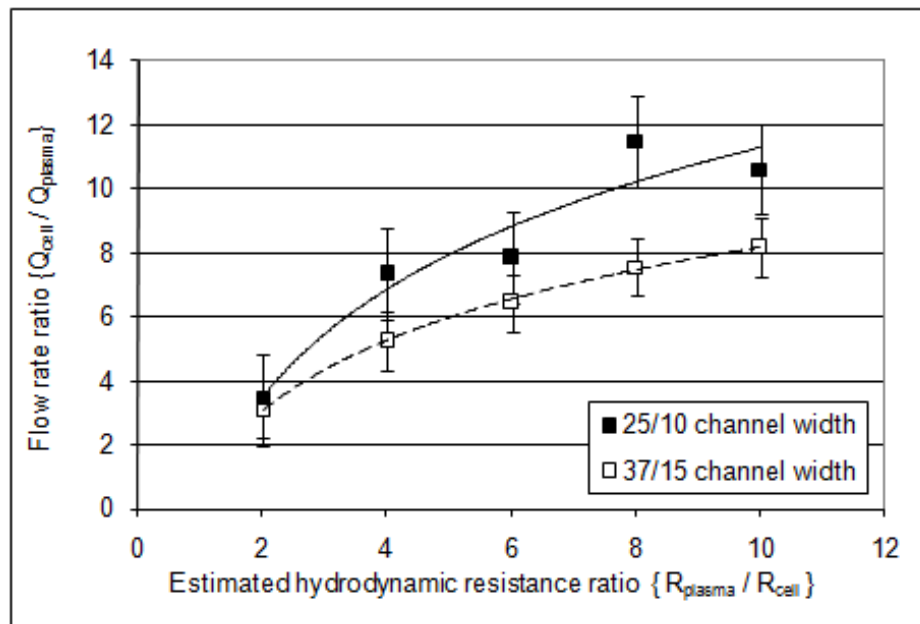

Figure 5.8: Comparison of designed vs. measured flow rate ratio. The black dots represent bifurcations with 10 μm & 25 μm wide branches, while white ones refer to that of 15 μm & 37 μm wide channels.

The higher flow rate ratios can be explained by the presence of several physical effects. One is the deterioration of the channel cross-section due to the technological characteristics of the DRIE process. Loading effect cause narrow trenches to be etched slower than wider features of the pattern, altering the hydrodynamic resistance of the fabricated capillaries. On the other hand, the surface properties of the capillary walls are influenced by a residual fluorocarbon polymer deposited during the Bosch-process. In the bifurcation branch collecting cells, the hydrophilic surfaces (top and bottom of the channels) are therefore remarkably greater than that of the plasma branch.

The practical hydrodynamic resistance of the small channels is also significantly affected by the so-called viscous-capillary phenomena. In my case the influence of the capillary diameter on the viscosity (Fahraeus – Lindqvist effect) is not considered due to the low haematocrit level. The saturation in the relationship between the flow rate ratio and estimated hydrodynamic resistance ratios can be rather assigned to the examined separation effect itself, since the cell concentration in the higher flow rate branch is always greater, and therefore the viscosity of the liquid is different from that of the lower flow rate branch of the bifurcation.

Performance evaluation

The PE parameters determined for test structures detailed in Table 5.2 are shown in Fig. 5.9. PE is increasing, when bifurcation flow rate regime is increasing. Previous experiments by other groups resulted in similar tendency.
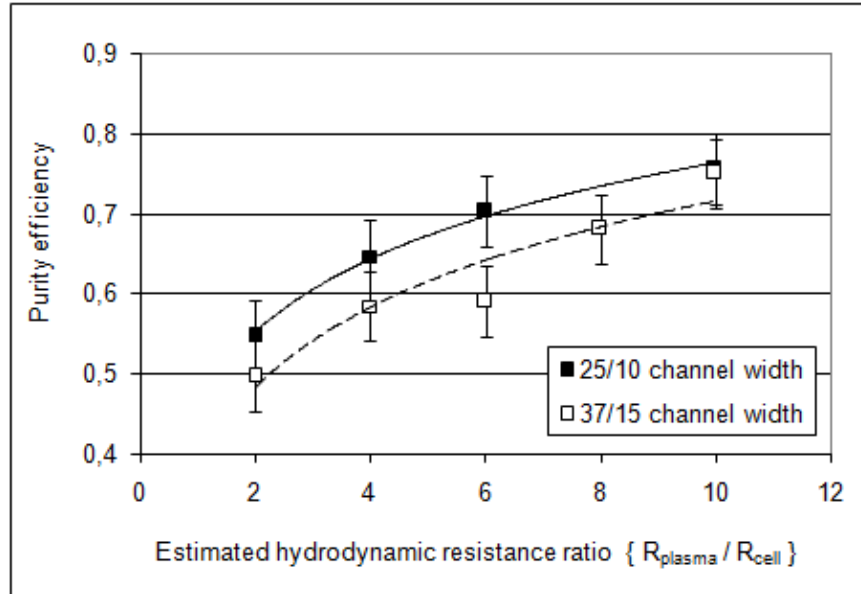

Figure 5.9: Purity efficiency of separation plotted against the designed ratio of hydrodynamic resistance of the bifurcation branches

SE of test structure strongly depends on the flow rate as well. The measured values are shown in Fig. 5.10. When the flow rate or resistance ratios are increasing, the SE of the device is getting lower.
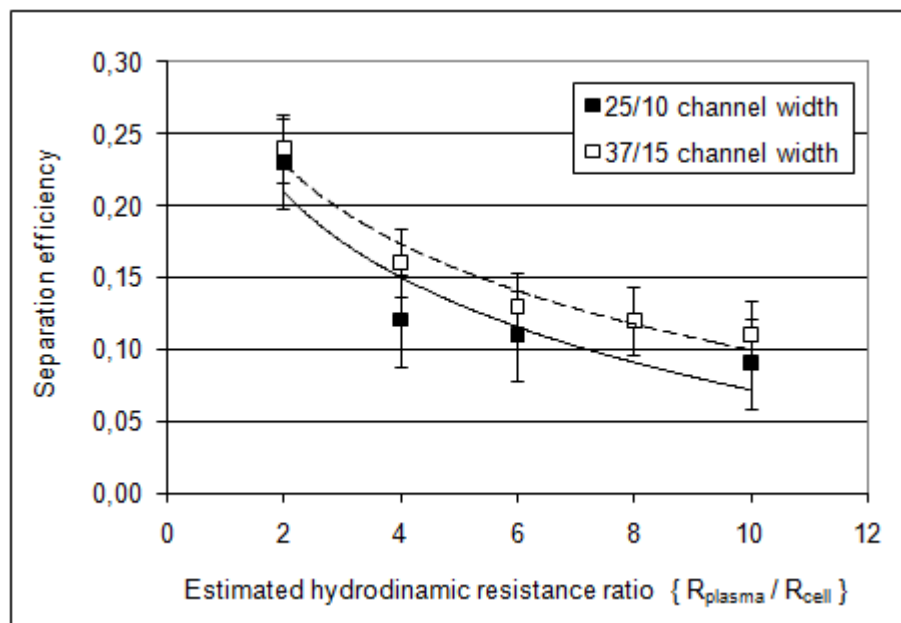

Figure 5.10: Separation efficiency plotted against hydrodynamic resistance ratio of the bifurcation.

Based on Fig. 5.9 and 5.10, it is also obvious, that thinner microchannels can improve PE, but deteriorate SE of the separation system, so a compromise should be made during the design. As other groups reported, the bifurcation angle could significantly affect the purity efficiency [5.17, 5.21]. I have also checked that how PE changes when the angle of bifurcation varies. Four different angles (see Fig. 5.11) were investigated. According to my measurements, a larger angle of inclination between bifurcation branches results in lower PE.
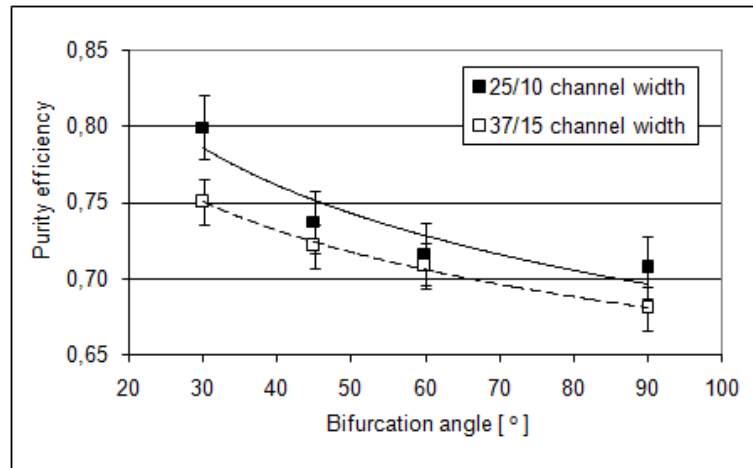

Figure 5.11: The influence of bifurcation angle on purity efficiency of the separation.

The above statement was also checked by Finite Element Analysis including all type of bifurcation angles tested experimentally. Figure 5.12.a illustrates the pressure values in the cross-section of a microchannel (Area = 10 μm x 25μm) right before the fluid enters the bifurcation space. Apparently, at decreasing angle of inclination the pressure gradient is getting higher as the particle is migrating close to the plasma branch. This implies that at a critical streamline the particle tends to move into the daughter vessel rather than into the higher flow-rate channel. This tendency is in good agreement with the proposed theory detailed in the latest literature [5.17]. The velocity amplitude in the direction of the plasma vessel is represented by Figure 5.12.b.
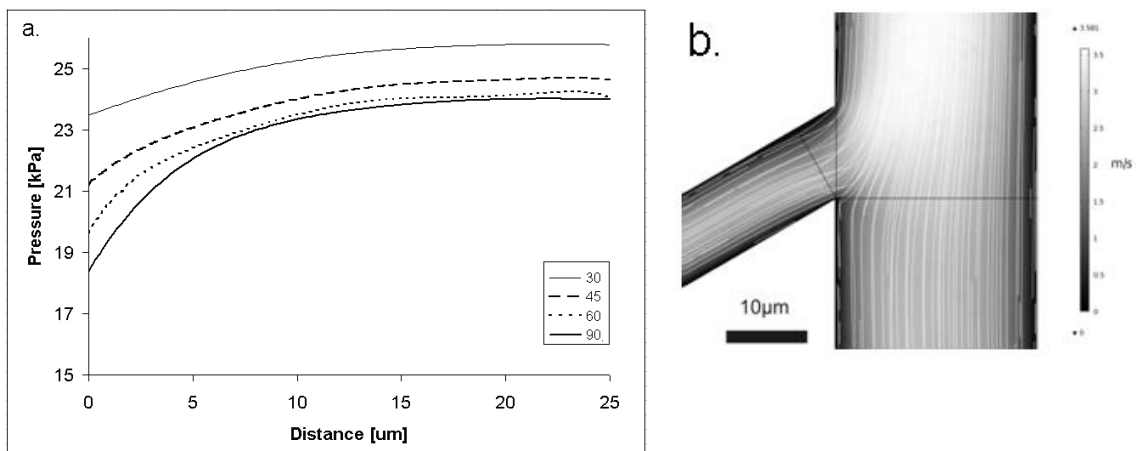

Figure 5.12: Pressure gradient along the main channel before entering the bifurcation (a.) and distribution of velocity amplitude in the vicinity of a bifurcation with inclination angle 60° (b.)

5.3 Optimisation and integration of Zweifach-Fung separation method

5.3.1. Cascade-type bifurcation based separation system

Since the integration of a single bifurcation into a lab-on-a-chip system is usually inadequate due to the low plasma yield, a series of bifurcation (often referred as cascade-type) is used instead [5.4].
Before proposing a concept of cascade-type system, conclusion on single bifurcation analysis has to be drawn. Based on the experimental and simulation results detailed in previous chapters, the following rule of thumb can be set up for geometric design for single bifurcations.

- Large hydrodynamic resistance ratios should be designed.
- Change of viscosity in the main stream should be considered.
- Larger daughter vessels produce larger SE and smaller PE
- Trade-off between PE and SE is inevitable.
- Small inclined angle between main flow and daughter flow is preferable.
- Migration of cells towards lower flow rate branch should be avoided.

To prove how lateral migration influences separation performance, a series of bifurcation was designed such that only flow rate ratios were determined at each bifurcation by circuit analogy. The comparison of the performance of a four-step and a single bifurcation is illustrated by Table 5.3.
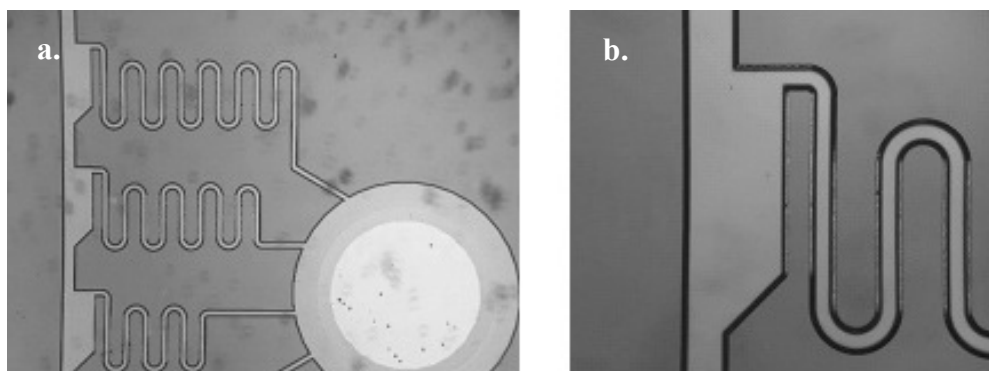
	Single bifurcation		Four-step cascade bifurcation	
Inclined angle of bif. branches	45	90	45	90
Purity efficiency	72.1%	68%	48.6%	46%
Separation efficiency	14%	12%	37.2%	49%

Table 5.3: Effect of multiple bifurcation in a separation system; flow rate ratio, cell branch and plasma branch are 8, 37μm and 15μm respectively.

Although due to the larger number of bifurcation, the separation efficiency of cascade-type systems are remarkable, purity efficiency is still well below that of a single bifurcation. This suggests that lateral migration towards daughter vessels is an increasing issue in case of every subsequent bifurcation. Deflections of velocity streamlines (Figure 5.12.b) close enough to the plasma branches suggest that a preliminary sorting particles before each bifurcation is essential in order to have acceptable purity efficiency.
A possible technique of enhancing PE in cascade systems is structural focusing of the particles. The proposed concept of this pre-sorting microstructure increasing the skimming space before the separation microstructure is shown in Fig. 5.13.

Figure 5.13: Optical microscopic image of cascade type bifurcations with preliminary cell-sorting designed for high-throughput plasma separation (a.), enlarged view of a single bifurcation (b.)

The viscosity of separated sample is also changing from bifurcation to bifurcation, which is not negligible. According to Fig. 5.9 and Fig. 5.10, on purity and separation efficiency, sample compartment in the main stream after each bifurcation will enrich in particles and therefore an increasing viscosity is raised. Finally, the performance of each preceding bifurcation is deteriorated by subsequent change in hydrodynamic resistance. Consequently, the characterisation of single bifurcations should be always carried out before applying any in cascade-type separation systems.

5.3.2. Towards the Lab on a Chip

The opportunity of applying the above results was given in the framework of ENIAC CAJAL4EU platform [5.22]. As the participant of this international project, the Institute for Technical Physics & Material Sciences is involved in the development of a nanopore-based solid-state sensor system including the integration of microfluidic functions as well. My task was to participate in the development of the microfluidic system which contains both the sensing structure (nanopore membrane) and preliminary sample preparation functions and can be interfaced through an intermediate microfluidic platform (developed by Micronit Ltd.) to a measurement system (developed by 77Elektronika Ltd.).

The application of the complex micro- and nanofabricated structures as sensing transducers becomes more relevant regarding high sensitive chemical or biochemical sensor systems. With the application of novel and innovative biosensing principles new possibilities are being revealed in medical applications as well. Based on the pore through transport modulation phenomena (see Figure 5.14) the chemically modified nanopore arrays can be successfully applied to the detection of specific biomolecules selectively binding in the pores. The main subject of the development is the verification of the applicability of the nanopore based sensors for label-free detection of CVD related marker proteins.
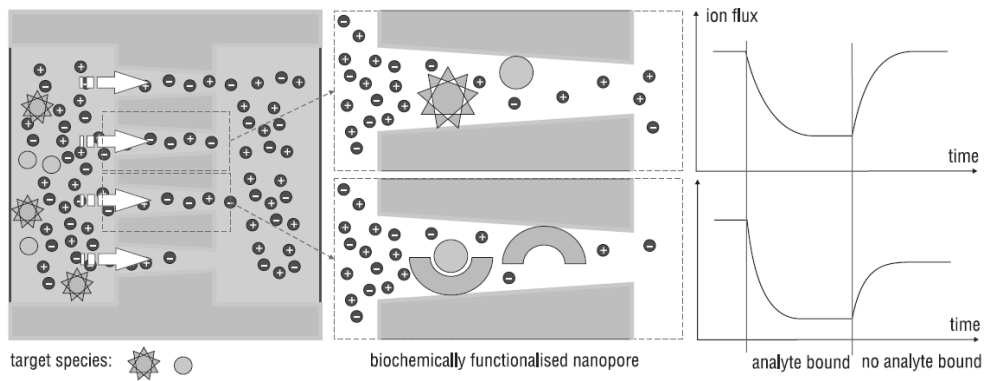
Figure 5.14: Representation of ion transport modulation through nanopore membranes.Target species immobilized in the nanopore contributes to impedance reduction measured through the membrane. This way a very sensitive detection of biomarkers can be achieved by simple electrical measurement.

A possible nanopore fabrication method is Focused Ion Beam milling of solid-state membranes by Ga ions [5.23]. Due to this technique nanopore of conical shape can be realized as is illustrated in Figure 5.15.
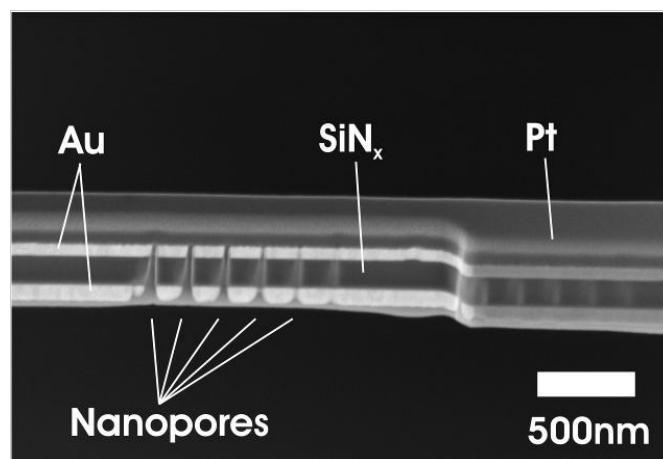

Figure 5.15: Representative layer structure containing a nanopore matrix fabricated by FIB. The platinum layer is sputtered subsequently in order to support the pores during microcutting.

In my work, I focused on the integration of separation and sample transport functions as well as nanopore as transducer element into a single autonomous system. Integration of microfluidic sample manipulation has the following advantages:

- Sample transport to sensor area is included
- Microscale separation facilitates the use of whole blood as initial analyte
- Disposable fluidic cartridge can be developed
- Both fluidic and electrical addressing is included.
- Membranes can be functionalised through microfluidics

The schematic representation of the proposed 3D microfluidic system and its connection to the intermediate microfluidic platform is shown in Fig. 5.16.

66
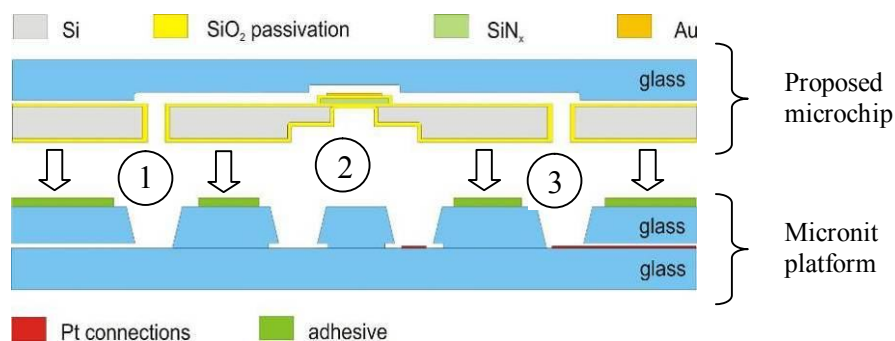
Figure 5.16. Schematic cross-sectional view of the proposed nanopore membrane structure integrated into the transport microfluidic system. Sample flow is considered from chamber 1 to chamber 3, while chamber 2 serves as an electrolyte reservoir for the impedance measurements. Measurement of the analytical signal is performed through Pt electrodes integrated on the Micronit platform.

The transducer device was fabricated by the combination of silicon micromachining and subsequent nanofabrication processes considering the chemical, electrical and mechanical requirements. The vertical fluidic connections, the microfluidic channels and the multilayer membrane structure were developed by MEMS technology steps as Low Pressure Chemical Vapour Deposition (LPCVD) of silicon-dioxide (SiO_2), stoichiometric (Si_3N_4) / non-stoichiometric silicon-nitride (SiN_x) layers, evaporation of titanium-dioxide and gold layers and multistep Deep Reactive Ion Etching (DRIE) of the silicon.

Considering the nanopore based electrochemical metrology high electrical and chemical resistance of the mechanical layers are crucial requirements, so the performance of the structural materials were extensively characterized by electrochemical impedance spectroscopy and fast chronoamperometry to provide a feedback on the optimal layer structuring. To ensure both chemical and electrical resistance and low residual stress a SiO_2 / SiN_x stacked supporting membrane with adequate layer thickness ratio was realised. The realised silicon structure was anodically bonded to the glass microfluidics in wafer level applying adequate working parameters (temperature, chamber pressure) limited by the integrated materials (gold) and thin layer structure. The final stacked structure was bonded onto fluidic connection platform designed and realised by the Micronit Microfluidics BV. The realised structures are shown in Fig. 5.17. The solid state nanopores were fabricated by Focused Ion Beam milling, the achieved geometry parameters are presented in Fig. 5.17. The final device contains an on-chip separator system.
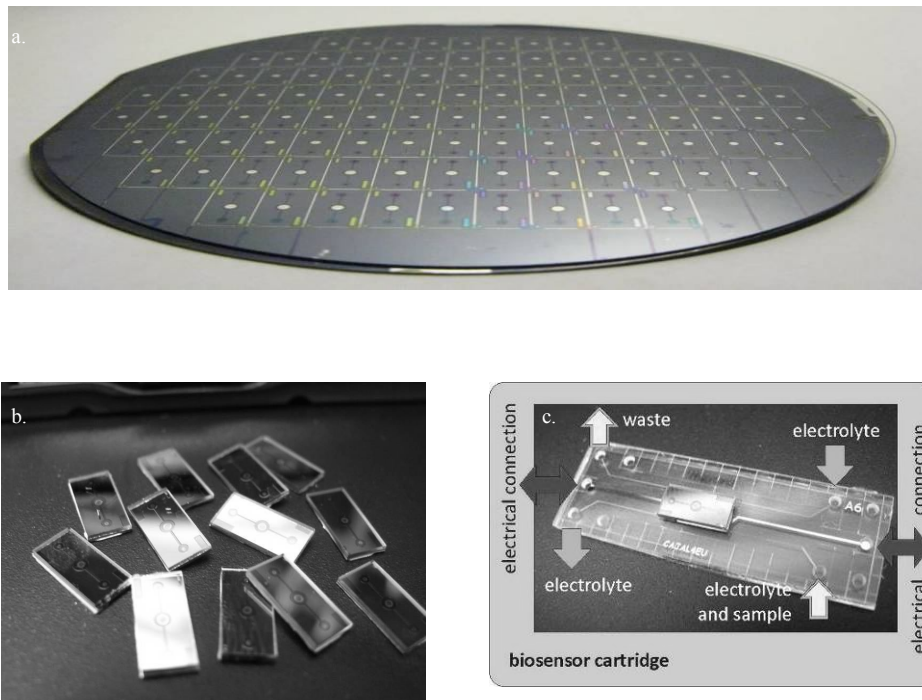
Figure 5.17: Wafer-scale layout of the proposed microchips (a.) and the individual sealed silicon-glass structures after micromachining has been completed (b.). Back side fluidic connections (production of Micronit Microfludics BV) addressing the nanopores membrane is illustrated in figure (c.).

The feasibility of the integrated microfluidics for nanopore sensing is characterized in terms of contingent shunting and proper sealing by impedance spectroscopy. It is obvious that the impedance through nanopore membrane should not be deteriorated by electrical parameters of the transport fluidics. Given the high resistance of the nanopore any leakage or shunting would prohibit the detection of specific pore resistance changes. The circuit model of the device is illustrated in Fig. 5.18.
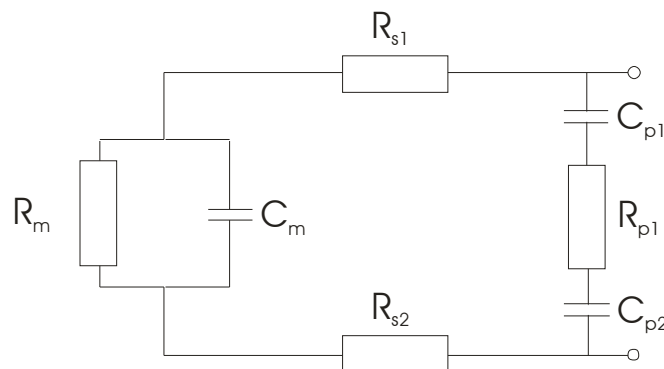

Figure 5.18: Circuit model of the microfluidic system including the integrated nanopore membrane. R_s represents resistance of the transport microfluidics. R_m and Cm constitutes the impedance of the nanopore membrane, while R_{p1} stands for the parallel resistance through the solid-state substrate. C_{p1} and C_{p2} are bilayer capacities.

The impedance of transport fluidics and nanopore was evaluated by measuring between points 1 and 3 (Z_s), and 2 and 3 (Z_m+Z_p) respectively (see Fig. 5.16 and 5.18 for detailed description). I noticed that the resistance of the microfluidics connects in the setup designed is negligible with respect of the pore resistance, which showed clear dependence of electrolyte concentration (see Fig. 5.19).
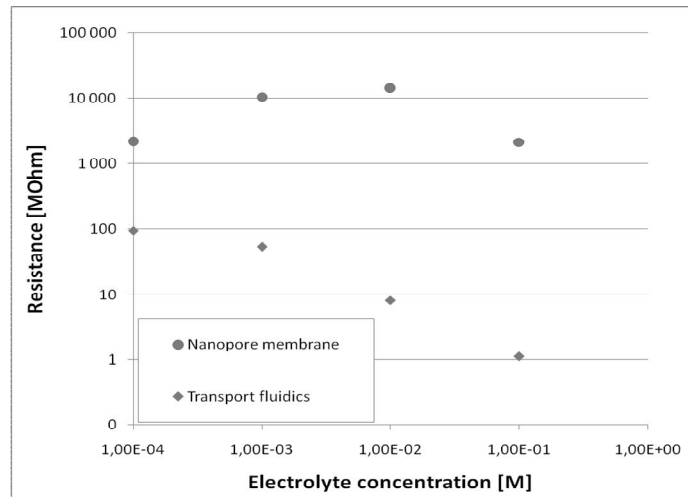
Figure 5.19: Ohmic component of impedance measure in the case of microfluidic integrated nanopore chips at different electrolyte concentration of KCl. Due to the difference in impedance values between transport fluidics and nanopore membrane, the proposed microsystem is a good candidate for the detection of blood proteins in low concentration analytes.

According to the above results, the integrated microfluidic platform is a promising candidate for the future detection of biomarkers with high sensitivity.

6. Overview of scientific results

Thesis Group I: I developed and characterised deep-brain silicon microprobes (up to 7cm) containing both microfluidic and electrical functions.

I.1. I developed a process sequence based on MEMS process flow, that is feasible for the integration of drug delivery and electrical functions in a single neural silicon microprobe.
a) I developed the technology of buried microfluidic channels in single-crystalline silicon by using of deep reactive ion etching and selective aluminum deposition, which finally resulted in planar surface facilitating subsequent photolithography for further integration of IC or MEMS components [K1, L1, Sz1].
b) I determined how the fabrication parameters affect the shape of the realized microchannels. I found that anisotropy during SF_6 etching increases as trench depth (up to 110μm) is increasing. My experiments proved that increasing trench width (between 2-6μm) and/or decreasing aspect ratio (between 12-3) causes increase in etch rate of SF_6 etching (between 6-25 μm/etch cycle) [L2].
c) I proved that the proposed buried microfluidic channels can be integrated into single multi-electrodes [K2].

I.2. I performed the mechanical and hydrodynamic characterisation of the realised microprobes.
a) I experimentally characterised the response of non-hollow and hollow silicon microprobes having several geometric properties (cross-section, length) to axial loading and determined the relationship between probe geometry and fracture forces. I found that fracture force of DRIE etched silicon microprobes is increasing by larger cross-section (with width and thickness in the range of 200-400μm), and the integrated microchannels may cause deteriorate force values by 80%. I also found that displacement of microchannel axis inside the probeshaft (inclined angle of tip edges is 30°) enhances the robustness of hollow microprobes.
b) I tested the mechanical robustness of non-hollow microprobes by in vivo insertion into rat brain. I determined the relationship between insertion speed and penetration force and dimpling in the case of several microprobe cross-section. I found that increasing the insertion speed in the regime of 1-10.2mm/min causes remarkable increase in penetration force (between 30-160mN). I also determined that dimpling (between 1-1.7mm) increases monotone by increasing interfacial area of the probes.
c) I experimentally characterised the hydrodynamic behaviour of buried microchannels integrated into hollow microprobe shafts between pressure range 0-250kPa. I determenied that in the investgiated pressure regime leak-free injection can be performed. I also determined that pressure-flow characteristics through the proposed microchannels is linear in the analyzed cross-section range (200-405μm^2). I proved by in vivo injection that hollow microprobes are feasible to be used for neural drug delivery in the μL/min range [K2].

Thesis Group II: I realised and optimized a glass-silicon based microfluidic separator. Integrating the proposed separation principle into a biochemical sensor, I developed an autonomous lab-on-a-chip system including nanopore membrane as transducer element.

II.1. I realised and carried out the performance characterisation and optimization of a micromachined particle separation system based on Zweifach-Fung principle.
a) I designed and realised silicon-glass heterostructures to analyse the effect of geometric properties on the performance of passive particle separator utilizing Zweifach-Fung principle. I found that inceasing main (of width between 15-37μm) and daughter (of width between 10-25μm) channel cross-section improves separation efficiency by even 20%, but deteriorate purity efficiency by even 10% in case of fixed hydrodynamic resistance ratios (2-10) between bifurcation branches and fixed channel depth (10μm). I determined that increasing the angle of bifurcation decrease purity by 7% in average [K3, L3].
b) Besides performance analysis, I performed experiments and modeling which proved that lateral migration is an inherently dominant effect of Zweifach-Fung separation. Based on my results, I proposed a concept of cascade bifurcation system which can be applicable for further enhancement of separation purity by structural focusing of particles and placing daughter microchannels out of the critical velocity streamlines [K3, L3].

II.2. I established a Lab-on-a-chip concept which includes a sub-system for whole blood manipulation and solid-state nanopore membrane as transducer.
a) I designed and developed the fabrication technology of a silicon-glass heterogenous microfluidic system, which includes sample transport and preparation (dilution/separation) and integrated read-out facilitating biochemical detection based on solid-state nanopore transducers [K4, K5].
b) I proved the applicability of the system by measuring the electrical performance by impedance spectroscopy. I found that serial and parallel impedance of microfluidic environment including sample preparation and transport functions is comparably smaller than that of the nanopore impedance. Therefore, the sensing principle can be applied even as part of the proposed integrated microfluidic platform. [K4, K5].

7. Utilization of scientific results

Results detailed in Thesis Group I contributed to the fabrication of neural microprobes in the MEMS Laboratory of TTK-MFA, which has been successfully used in neurophysiological measurements in the Institute of Cognitive Neuroscience and Psychology and in the Materials Science and Technology Institute of Bay Zoltán Applied Research Nonprofit Ltd.

Results detailed in Thesis Group II contributed to the improvements of international consortial grants like P3SENS (Polymer Photonic multiparametric biochemical SENSor for Point-of-care diagnostics) and CAJAL4EU (ENIAC project on Nanoelectronics-based biosensor technology platforms) projects.

8. References

[1.1]   W. M. Grill, S. E. Norman, R. V. Bellamkonda, Implanted Neural Interfaces: Biochallenges and Engineered Solutions, Annual Review of Biomedical Engineering 11 (2009) 1-24

[1.2]   P. G. Gross, E. P. Kartalov, A. Scherer, L. P. Weiner, Applications of microfluidics for neuronal studies, Journal of the Neurological Sciences 252 (2007) 135–143

[1.3]   P. S. Dittrich, A. Manz, Lab-on-a-chip: microfluidics in drug discovery, Nature Reviews Drug Discovery 5 (2006) 210-218

[1.4]   T. M. Squires, S. R. Quake, Microfluidics: Fluid physics at the nanoliter scale, Rev. Mod. Phys. 77 (2005) 977–1026

[1.5]   G. M. Whitesides, Overview The origins and the future of microfluidics, Nature 442 (2006) 368-373

[1.6]   S. Howorka, Z. Siwy, Nanopore analytics: sensing of single molecules, Chem. Soc. Rev., 38 (2009) 2360-2384

[1.7]   W. G Lee, Y. Kim, B. G. Chung, U. Demirci, A. Khademhosseini, Nano/Microfluidics for diagnosis of infectious diseases in developing countries, Advanced Drug Delivery Reviews 62 (2010) 449–457

[1.8]   H. Bruus, Theoretical Microfluidics, Oxford University Press, 2007, ISBN-13: 978-0199235094

[2.1]   J. S. Perlmutter and J. W. Mink, Deep Brain Stimulation, Annu. Rev. Neurosci. 29 (2006) 229–257

[2.2]   B.S. Wilson and M. F. Dorman, Cochlear implants: A remarkable past and a brilliant future, Hearing Research 242 (2008) 3-21

[2.3]   N. A. Kotov, J. O. Winter, I. P. Clements, E. Jan, B. P. Timko, S. Campidelli, S. Pathak, A. Mazzatenta, C. M. Lieber, M. Prato, R. V. Bellamkonda, G. A. Silva, N. W. Kam, F. Patolsky and L. Ballerini, Nanomaterials for Neural Interfaces, Advanced Materials 21 (2009) 1–35

[2.4]   A. W. Laxton, D. F. Tang-Wai, M. P. McAndrews, D. Zumsteg and R. Wennberg, A phase I trial of deep brain stimulation of memory circuits in Alzheimer's disease, Annals of Neurology 68 (2010) 521–534

[2.5]   H. S. Mayberg, A. Lozano, V. Voon, H. McNeely, D. Seminowicz, C. Hamani, J. Schwalb and S. Kennedy, Deep Brain Stimulation for Treatment Resistant Depression, Neuron 45 (2005) 651-660

[2.6]   T. L. Ellis and A. Stevens, Deep brain stimulation for medically refractory epilepsy, Neurosurgical Focus (2008) 25 E11

[2.7]   W. He and R. W. Bellamkonda, Nanoscale neuro-integrative coatings for neural implants, Biomaterials 26 (2005) 2983–2990

[2.8]   J. P. Seymour and D. R. Kipke, Neural probe design for reduced tissue encapsulation in CNS, Biomaterials 28 (2007) 3594–3607

[2.9]   G. Lehew and M. A. L. Nicolelis, State-of-the-art microwire array design for chronic neural recordings in behaving animals Methods for Neural Ensemble Recordings. 2nd edition. Boca Raton (FL): CRC Press; 2008. Chapter 1, ISBN: 978-1420006414.

[2.10] J. G. Malpeli, Reversible inactivation of subcortical sites by drug injection, J. Neurosci. Methods 86 (1999) 119–28

[2.11] T. Jochum, T. Denison and P. Wolf, Integrated circuit amplifiers for multi-electrode intracortical recording, J. Neural Eng. 6 (2009) 012001

[2.12] M. M. Wintrobe, Blood, Pure and Eloquent: A Story of Discovery, of People, and of Ideas, McGraw-Hill. (1980) 771, ISBN 13: 978-0070711358

[2.13] J. Bauer, Advances in cell separation: recent developments in counterflow centrifugal elutriation and continuous flow cell separation, J. Chromatogr. B 722 (1999) 55–69

[2.14] M. Toner, D. Irimia, Blood-on-a-chip, Annual Rev Biomed Eng. 7 (2005) 77-103

[2.15] J. Zhang; Q. Guo; M. Liu and J. Yang. A lab-on-cd prototype for high-speed blood separation. Journal of Micromechanics and Microengineering, 18 (2008) 125025

[2.16] Y.C Fung: Biomechanics, Mechanical Properties of Living Tissues, Springer Vol. 2. (1993), ISBN-13: 978-0387979472

[2.17] R. Paul, J. Apel, S. Klaus, F. Schügner, P. Schwindke, H. Reul: Shear Stress Related Blood Damage in Laminar Couette Flow, Blackwell Publishing Inc. (2003) 517-529

[3.1] J. D. Plummer, Silicon VLSI technology, Second Ed., Prentice Hall (2000)

[3.2] S. Terry, J. H. Jerman, J. Angell, Chromatographic Air Analyzer Fabricated on a Silicon Wafer, IEEE Trans. Electron. Devices, ED-26 (1979) 1880-1886

[3.3] D. Reyes, D. Iossifidis, P-A. Auroux, A. Manz, Micro Total Analysis Systems, Anal. Chem., 74 (2002) 2623-2636

[3.4] A. Manz, N. Graber, H. Widmer, Miniaturized total chemical analysis systems: a novel concept for chemical sensing, Sens. & Act. B 1 (1990) 244-248

[3.5] D. Harrison, K. Fluri, K. Seiler, Z. Fan, C. Effenhauser, A. Manz, Micromachining a miniaturized capillary electrophoresis-based chemical analysis system on a chip, Science 261 (1993) 895-897

[3.6] D. Harrison, A. Manz, P. Glavina, Electroosmotic pumping within a chemical sensor system integrated on silicon, Transducers '91 (1991) 792-795

[3.7] B.Weigl, P. Yager, Microfluidic Diffusion-Based Separation and Detection Science 283 (1998) 346-347

[3.8] J. Knight, A. Vishwanath, J. Brody, R. Austin, Hydrodynamic focusing on a silicon chip: mixing nanoliters in microseconds, Phys. Rev. Lett. 80 (1998) 3863-3866

[3.9] P.Wilding,M. Schoffner, L. Kricka, PCR in a silicon microstructure, J. Clin. Chem. 40 (1994) 1815-1818

[3.10] M. Kopp, A. De Mello, A. Manz, Chemical amplification: continuous-flow PCR on a chip, Science 280 (1998) 1046-1048

[3.11] A.Y. Fu, C. Spence, G.H. Arnold, S.R. Quake, A microfabricated fluorescence-activated cell sorter, Nature Biotechnol. 17 (1999) 1109-1111

[3.12] A. Kamholz, B.Weighl, B. Finlayson, P. Yager, Quantitative Analysis of Molecular Interaction in a Microfluidic Channel: The T-Sensor, Anal. Chem. 71 (1999) 5340-5347

[3.13] D. Smith, S. Chu, Response of Flexible Polymers to a Sudden Elongational Flow Science 281 (1998) 1335-1340

[3.14] S. J. Lee, S.Y. Lee, Micro total analysis system (micro-TAS) in biotechnology, Appl Microbiol Biotechnol. 3 (2004) 289-99

[3.15] Method for anisotropic plasma etching of substrates, Patent US5498312 (1996)

[3.16] N. Nguyen, S. T. Wereley, Fundamentals and Applications of Microfluidics, Second Edition, Artech House (2006)

[3.17] S. Wu, J. Mai, Y. Zohar, Y. C. Tai, C. M. Ho, A Suspended Microchannel with Integrated Temperature for High-Pressure Flow Studies, Proceedings of MEMS'98 (1998) 87–92

[3.18] C. G. Keller, Hexsil tweezers for teleoperated micro-assembly, MEMS '97, Proceedings (1997) 72-77

[3.19] N. H. Talbot, A. P. Pisano, Polymolding: Two Wafer Polysilicon Micromolding of Closed-Flow Passages for Microneedles and Microfluidic Devices, Technical Digest of the IEEE Solid State Sensor and Actuator Workshop (1998) 265–268

[3.20] V. L. Spiering, J. N. Burger, A. Gert-Jan, Novel Microstructures and Technologies Applied in Chemical Analysis Techniques, Proceedings of Transducers '97 (1997) 511–514

[3.21] I. Papautsky, J. Brazzle, H. Swerdlow, R. Weiss, A. B. Frazier, Micromachined Pipette Arrays, IEEE Transaction on Biomedical Engineering 47 (2000) 812-819

[3.22] D. Sobek, S. D. Senturia, M. L. Gray, Microfabricated Fused Silica Flow Chambers for Flow Cytometry, Technical Digest of the IEEE Solid State Sensor and Actuator Workshop (1994) 260–263

[3.23] D. J. Harrison, Miniaturized Chemical Analysis Systems Based on Electrophoretic Separations and Electroosmotic Pumping, Proceedings of Transducers '93 (1993) 403–406

[3.24] S. C. Jacobson, "Electrically Driven Separations on a Microchip," Technical Digest of the IEEE Solid State Sensor and Actuator Workshop (1994) 65–68

[3.25] H. Mobius, W. Ehrfeld, V. Hessel, T. Richter, Sensors Controlled Processes in Chemical Reactors, Proceedings of Transducers '95, (1995) 775–778

[3.26] L. Jiang, M. Wong, Y. Zohar, A Micro-Channel Heat Sink with Integrated Temperature Sensors for Phase Transition Study, Proceedings of MEMS'99 (1999) 159–164

[3.27] J. Chen, K. D. Wise, A High Resolution Silicon Monolithic Nozzle Array for Inkjet Printing," IEEE Transaction on Electron Devices 44 (1997) 1401–1409

[3.28] M. J. de Boer, R. W. Tjerkstra, J. W. Berenschot, H. V. Jansen, G. J. Burger, J. G. H. Gardeniers, M. Elwenspoek , A. van den Berg, Micromachining of Buried Micro Channels in Silicon, J. Microelectromech. Syst. 9 (2000) 94-103

[3.29] A. Agarwal, N. Ranganathan, W. L. Ong, K. C. Tang, L. Yobas, Self-sealed circular channels for micro-fluidics, Sens. & Act. A 142 (2008) 80–87

[3.30] M. Dijkstra, M. J. de Boer, J. W. Berenschot, T. S. J. Lammerink, R. J. Wiegerink, M. Elwenspoek, A versatile surface channel concept for microfluidic applications, J. Micromech. Microeng. 17 (2007) 1971–1977

[3.31] S. J. Paik, S. Byuna, J. M. Lima, Y. Park, A. Lee, S. Chung, J. Changa, K. Chuna, D. Choa, In-plane single-crystal-silicon microneedles for minimally invasive microfluid systems, Sens. & Act. A 114 (2004) 276–284

[3.32] C. Rusu, R. van't Oever, M. J. de Boer, H. V. Jansen, J. W. Berenschot, M. L. Bennink, J. S. Kanger, B. G. de Grooth, M. Elwenspoek, J. Greve, J. Brugger, A. van den Berg, Direct Integration of Micromachined Pipettes in a Flow Channel for Single DNA Molecule Study by Optical Tweezers, J. Microelectromech. Syst. 10 (2001) 238-245

[4.1] D. A. Robinson, The electrical properties of metal microelectrodes. Proc. IEEE 56 (1968) 1065-1071

[4.2] J. Skrzypek, E. Keller, Manufacture of metal microelectrodes with scanning electronmicroscope, IEEE Trans. Biomed. Eng. 22 (1975) 435-437.

[4.3]   K. D. Wise, J. B. Angell, A. Starr, An integrated-circuit approach to extracellular microelectrodes. IEEE Trans. Biomed. Eng. BME-17 (1970) 238-247

[4.4]   K. D. Wise, K. Najafi, Microfabrication Techniques for Integrated Sensors and Microsystems, Science 254 (1991) 1335-1342

[4.5]   D. Banks, Neurotechnology, Eng. Sci. 7 (1998) 135-144

[4.6]   T. M. Pearce, J. C. Williams, Microtechnology: meet neurobiology, Lab Chip 7 (2007) 30-40

[4.8]   M. HajjHassan, V. Chodavarapu and S. Musallam, NeuroMEMS: Neural Probe Microtechnologies, Sensors 8 (2008) 6704-6726

[4.9]   P. J. Rousche, D. S. Pellinen, D. P. Pivin, J. C. Williams, R. J. Vetter, D. R. Kipke, Flexible polyimide-based intracortical electrode arrays with bioactive capability. IEEE Trans. Biomed. Eng. 48 (2001) 361-371

[4.10]   S. Metz, A. Bertsch, D. Bertrand, P. Renaud, Flexible polyimide probes with microelectrodes and embedded microfluidic channels for simultaneous drug delivery and multi-channel monitoring of bioelectric activity, Biosens. Bioelectron. 19 (2004) 1309-1318

[4.11]   K. Najafi, Micromachined systems for neurophysiological applications. In Handbook of Microlithography, Micromachining and Microfabrication, Volume II: Micromachining and Microfabrication, Prosenjit Rai-Choudhury (Ed.); SPIE PRESS Monograph: London, 1997.

[4.12]   K. Seidl, S. Herwik, T. Torfs, H. P. Neves, O. Paul, P. Ruther, CMOS-Based High-Density Silicon Microprobe Arrays for Electronic Depth Control in Intracortical Neural Recording, Journal of Microelectromechanical Systems 20 (2011) 1439 - 1448

[4.13]   J. Muthuswamy, M. Okandan, T. Jain, A. Gilletti, Electrostatic microactuators for precise positioning of neural microelectrodes. IEEE Trans. Biomed. Eng. 52 (2005) 1748-1755

[4.14]   Q. Bai, K. D. Wise, Single-unit neural recording with active microelectrode arrays. IEEE Trans. Biomed. Eng. 48 (2001) 911-920.

[4.15]   K. D. Wise, D. J. Anderson, J. F. Hetke, D. R. Kipke, K. Najafi, Wireless implantable, microsystems: High-density electronic interfaces to the nervous system. Proc. IEEE 92 (2004) 76-97

[4.16]   K. E. Jones, P. K. Campbell, R. A. Normann, A glass silicon composite intracortical electrode array. Ann. Biomed. Eng. 20 (1992) 423-437

[4.17]   R. C. Kelly, M. A. Smith, J. M. Samonds, A. Kohn, A. B. Bonds, J. A. Movshon, Comparison of recordings from microelectrode arrays and single electrodes in the visual cortex. J. Neurosci. 27 (2007) 261-264

[4.18]   G. Ensell, D. J. Banks, P. R. Richards, W. Balachandran, D. J. Ewins, Silicon-based microelectrodes for neurophysiology, micromachined from silicon-on-insulator wafers. Med. Biol. Eng. Comput. 38 (2000) 175-179

[4.19]   K. Cheung, L. Gun, K. Djupsund, D. Yang, L. P. Lee, A new neural probe using SOI wafers with topological interlocking mechanisms. IEEE Microtech. Med. Biol. (2000) 507-511

[4.20]   S. Kisban, S. Herwik, K. Seidl, B. Rubehn, A. Jezzini, M. A. Umiltà, L. Fogassi, T. Stieglitz, O. Paul, P. Ruther, Microprobe array with low impedance electrodes and highly flexible polyimide cables for acute neural recording, Conf Proc IEEE Eng Med Biol Soc. (2007) 175-178

[4.21]   S. Spieth, O. Brett, K. Seidl, A. A. A. Aarts, M. A. Erismis, S. Herwik, F. Trenkle, S. Tatzner, J. Auber, M. Daub, H. P. Neves, R. Puers, O. Paul, P.

Ruther and R Zengerle, A floating 3D silicon microprobe array for neural drug delivery compatible with electrical recording, J. Micromech. Microeng. 21 (2011) 125001

[4.22] M. J. de Boer, R. W. Tjerkstra, J. W. Berenschot, H. V. Jansen, G. J. Burger, J. G. H. Gardeniers, M. Elwenspoek and A. van den Berg, Micromachining of Buried Micro Channels in Silicon. J. Microelectromech. Syst. 9 (2000) 94-103

[4.23] R. Abdolvand and F. Ayazia, An advanced reactive ion etching process for very high aspect-ratio sub-micron wide trenches in silicon, Sens. and Act. A 144 (2008) 109-116

[4.24] CMOS technológiába integrálható eljárás egykristályos Si alapú, eltemetett mikrofluidikai csatornahálózattal rendelkező eszköz előállítására, a szubsztrátfelület planaritásának megőrzése mellett, Fekete Z., Pongrácz A., Szendrey Á. Fürjes P., Battistig G. (Szellemi Tulajdon Nemzeti Hivatala) 2011. 04. 30., P1100170

[4.24a] Silvaco Virtual Wafer Fab process simulation code, www.silvaco.com

[4.25] H. V. Jansen, H. Gardeniers, M. J. de Boer, M. Elwenspoek and J. Fluitman, A survey on the reactive ion etching of silicon in microtechnology, J. Micromech. Microeng. 6 (1996) 14–28

[4.26] H. V. Jansen, M. J. de Boer, S. Unnikrishnan, M. C. Louwerse and M. Elwenspoek, Black silicon method X., J. Micromech. Microeng. 19 (2009) 033001

[4.27] H. V. Jansen, M. J. de Boer, R. Wiegerink, N. Tas, E. Smulders, C. Neagu and M. Elwenspoek, RIE lag in high aspect ratio trench etching of silicon, Microelectronic Engineering 35 (1997) 45-50

[4.27a] I. Kondo, T. Yoneyama, O. Takenaka, Formation of high adhesive and pure Pt layers in TiO2, J. Vac. Sci. Technol. A 10 (1992) 3456-3459

[4.28] B. A. Ganji and B. Y. Majlis, Deep Trenches in Silicon Structure using DRIE Method with Aluminum as an Etching Mask. IEEE Int. Conf. on Semiconductor Electronics (2006) 41–47

[4.29] C. Cardinaud, M. Peignon and P. Tessier, Plasma etching: principles, mechanisms, application to micro- and nano-technologies, Applied Surface Science 164 (2000) 72-83

[4.30] N. Roxhed, P. Griss and G. Stemme, A method for tapered deep reactive ion etching using a modified Bosch process, J. Micromech. Microeng. 17 (2007) 1087–1092

[4.31] F. Gao, S. Ylinen, M. Kainlauri and M. Kapulainen, A modified Bosch process for smooth sidewall etching. Proc. 22nd Micromechanics and Microsystems Technology Europe Workshop (2011) Paper A12

[4.32] T. E. Schläpfer and B. H. Bewernick, Deep brain stimulation for psychiatric disorders--state of the art, Advances & Technical Standards In Neurosurgery 34 (2009) 37-57

[4.33] C. Chung, Geometrical pattern effect on silicon deep etching by an inductively coupled plasma system, J. Micromech. Microeng. 14 (2004) 656–662

[4.34] K. P. Larsen, D. H. Petersen, and O. Hansen, Study of the Roughness in a Photoresist Masked, Isotropic, SF6-Based ICP Silicon Etch, J. of Electroch. Soc., 153 (2006) G1051-G1058

[4.35] K. Najafi, Strength characterization of silicon microprobes in neurophysiological tissues IEEE Tr. on Biomed. Eng. 37 (1990) 474 – 481

[4.36] R. L. Rennaker, S. Street, A. M. Ruyle, A. M. Sloan, A comparison of chronic multi-channel cortical implantation techniques: manual versus mechanical insertion, Journal of Neuroscience Methods 142 (2005) 169–176

[4.37] A. Gefen, S. S. Margulies, Are in vivo and in situ brain tissues mechanically similar? Journal of Biomechanics 37 (2004) 1339–1352

[4.38] M. Welkenhuysen, A. A. Andrei, L. Ameye, W. Eberle and B. Nuttin, Effect of Insertion Speed on Tissue Response and insertion mechanics of a cronically implanted silicon-based neural probe IEEE Tr. on Biomed. Eng. 58 (2011) 3250-3259

[4.39] R. van Noort, T. R. P. Martin, M. M. Black, A. T. Barker and C. G. Montero, The mechanical properties of human dura mater and the effects of storage media Clin. Phys. Physiol. Meas. 2 (1981) 197

[4.40] A. Gefen, N. Gefen, Q. Zhu, R. Raghupathi, S. S. Margulies, Age-dependent changes in material properties of the brain and braincase of the rat, J Neurotrauma 11 (2003) 1163-77

[4.41] P. Aggarwal, C.R. Johnston, Geometrical effects in mechanical characterizing of microneedle for biomedical applications, Sensors and Actuators B 102 (2004) 226–234

[4.42] S. P. Davis, B. J. Landisa, Z. H. Adams, M. G. Allen, M. R. Prausnitz, Insertion of microneedles into skin: measurement and prediction of insertion force and needle fracture force Journal of Biomechanics 37 (2004) 1155–1163

[4.43] S. Misra, K. B. Reed, A. S. Douglas, K. T. Ramesh, and A. M. Okamura, Needle-Tissue Interaction Forces for Bevel-Tip Steerable Needles, Proceedings of the 2nd Biennial IEEE/RAS-EMBS International Conference on Biomedical Robotics and Biomechatronics Scottsdale, AZ, USA, (2008)

[4.44] N. Abolhassani, R. Patel, Mehrdad Moallema, Needle insertion into soft tissue: A survey, Medical Engineering & Physics 29 (2007) 413–431

[4.45] M. D. Johnson, O. E. Kao, D. R. Kipke, Spatiotemporal pH dynamics following insertion of neural microelectrode arrays, Journal of NeuroscienceMethods 160 (2007) 276–287

[4.46] P. J. Rousche and R. A. Normann, A method for pneumatically inserting an array of penetrating electrodes into cortical tissue, Annals of Biomedical Engineering 20 (1992) 413-422

[4.47] Q. Bai, K. D. Wise, D. J. Anderson, A high-yield microassembly structure for three-dimensional microelectrode arrays, IEEE Trans Biomed Eng 47 (2000) 281–289

[4.48] A. A. Sharp, A. M. Ortega, D. Restrepo, D. Curran-Everett, K. Gall, In Vivo Penetration Mechanics and Mechanical Properties of Mouse Brain Tissue at Micrometer Scales, Transactions on Biomedical Engineering 56 (2009) 45-53

[4.49] E. J. Boyd and D. Uttamchandani, Measurement of the anisotropy of Young's modulus in single-crystal silicon, J. of MEMS 21 (2012) 243-249

[4.50] Andilog Technologies, CENTOR Easy Digital ForceGaugemanual, http://www.andilog.com/pdf/spec-sheets/Centor-easy.pdf , May 2012

[4.51] R. J. Bridges, M. S. Stanley, M. W. Anderson, C. W. Cotman, A. R. Chambrlin, Conformationally defined neurotransmitter analogues. Selective inhibition of glutamate uptake by one pyrollidine-2,4-dicarboxylate diastereomer, J. Med. Chem. 34 (1991) 717–725.

[4.52] K. Ohta, T. Nomura, T. Kanno, K. Nagai, S. Yamamoto, Y. Yajima, T. Kondoh, E. Kohmura, N. Saito, T. Nishizakia, L-trans-PDC enhances hippocampal neuronal activity by stimulating glial glutamate release independently of

blocking transporters, Biochemical and Biophysical Research Communications 295 (2002) 376–381

[4.53] G. Paxinos and C. Watson, Rat Brain in Stereotaxic Coordinates, Academic Press 1997, ISBN-13: 978-0123741219

[4.54] K. Seidl, S. Spieth, S. Herwik, J. Steigert, R. Zengerle, O. Paul and P. Ruther, In-plane silicon probes for simultaneous neural recording and drug delivery , J. Micromech. Microeng. 20 (2010) 105006

[4.55] S. Chandrasekaran, J. D. Brazzle and A. B. Frazier, Surface micromachined metallic microneedles, J. Microelectromech. Syst. 12 (2003) 281–88

[4.56] K. C. Cheung, K. Djupsund, Y. Dan and L. P. Lee, Implantable multichannel electrode array based on SOI technology, J. Microelectromech. Syst. 12 (2003) 179–84

[4.57] L. J. Fernandez, A. Altuna, M. Tijero, G. Gabriel, R. Villa, J. Rodraguez, M. Batlle, R. Vilares, J. Berganzo and F. J. Blanco, Study of functional viability of SU-8 based microneedles for neural applications, J. Micromech. Microeng. 19 (2009) 025007

[4.58] D. Ziegler, T. Suzuki and S. Takeuchi, Fabrication of flexible neural probes with built-in microfluidic channels by thermal bonding of parylene, J. Microelectromech. Syst. 15 (2006) 1477–82

[4.59] J. D. Zahn, N. H. Talbot, D. Liepmann and A. P. Pisano, Microfabricated polysilicon microneedles for minimally invasive biomedical devices, Biomed. Microdevices 2 (2000) 295–303

[5.1] R. Fan, O. Vermesh, A. Srivastava, B. K. H. Yen, L. Qin, H. Ahmad, G. A. Kwong, C. Liu, J. Gould, L. Hood and J. R. Heath, Integrated barcode chips for rapid, multiplexed analysis of proteins in microliter quantities of blood, Nature Biotechnology 26 (2008) 1373-1378

[5.2] Curtis D Chin et. al. Microfluidics-based diagnostics of infectious diseases in the developing world, Nature Medicine 17 (2011) 1015–1019

[5.3] M. Toner, D. Irimia, Blood-on-a-chip, Annual Review of Biomedical Engineering 7 (2005) 77-103

[5.4] P. Goymer, Nanotechnology: Drawing tumour cells from blood, Nature Reviews Cancer 8 (2008) 81

[5.5] D. Heikali, D. Di Carlo, A niche for microfluidics in portable hematology analyzers, JALA 15, (2010) 319-328

[5.6] S. Haeberle; T. Brenner; R. Zengerle; J. Ducrée. Centrifugal extraction of plasma from whole blood on a rotating disk. Lab on a Chip 6 (2006) 776-781

[5.7] C. Blattert, R. Jurischka, I. Tahhan, A. Schoth and H. Reinecke. Improved plasma yield by a new design of microchannel bend structures. Proceeding on MicroTAS, 3 (2006) 146-148

[5.8] E. Sollier; H. Rostaing; P. Pouteau; Y. Fouillet; J. Achard. Passive microfluidic devices for plasma extraction from whole human blood. Sensors and Actuators B: Chemical 141 (2009) 617-624

[5.9] J. Moorthy and D. J. Beebe, In situ fabricated porous filters for microsystems. Lab on a Chip, 3 (2003) 62-66

[5.10] T. Crowley, V. Pizziconi . Isolation of plasma from whole blood using planar microfilters for lab-on-a-chip applications. Lab on a Chip 9 (2005) 922-929

[5.11] Y. Nakashima; S. Hata and T. Yasuda. Blood plasma separation and extraction from a minute amount of blood using dielectrophoretic and capillary forces. Sensors and Actuators B: Chemical, 145 (2010) 561-569

[5.12] S. Yang; A. Ündar and J. D. Zahn. A microfluidic device for continuous, real time blood plasma separation. Lab on a Chip, 6 (2006) 871-880

[5.13] M. Kersaudy-Kerhoas, D.M. Kavanagh, R.S. Dhariwal, C. Campbell. M.P.Y. Desmulliez, Validation of a blood plasma separation system by biomarker detection, Lab-on-a-Chip, 10 (2010) 1587-1595

[5.14] M. Kersaudy-Kerhoas; R. Dhariwal; M. P. Y. Desmulliez and L. Jouvet. Hydrodynamic blood plasma separation in microfluidic channels. Microfluidics and Nanofluidics, 8 (2010) 105-114

[5.15] K. Svanes, B.W. Zweifach, Variations in small blood vessel hematocrits produced in hypothermic rats by micro-occlusion. Microvascular Res 1, 210-220 (1968)

[5.16] Y.C. Fung, Stochastic flow in capillary blood vessels, Microvascular Res 5, 34-48 (1973)

[5.17] V. Doyeux, T. Podgorski, S. Peponas, M. Ismail and G. Coupier, Spheres in the vicinity of a bifurcation: elucidating the Zweifach–Fung effect, J. Fluid Mech. vol. 674 (2011) 359–388

[5.18] Laminar Boundary Layer, ed. L. Rosenhead, New York, Dover Publications Inc. (1963)

[5.19] Micronit Microfluidics, www.micronit.com

[5.20] Comsol Multiphysics 4.0, www.comsol.com

[5.21] B. W. Roberts and W. L. Olbricht, Flow-Induced Particulate Separations, AIChE Journal Vol. 49 No. 11 (2003) 2842-2849

[5.22] ENIAC project on Nanoelectronics-based biosensor technology platforms, www.cajal4eu.com

[5.23] Y. Fu, B. K. A. Ngoi, W. Zhou, T. F. Loh, Direct formation of nanopore array via focused ion beam fine milling and surface coating techniques, International Journal of Nanoscience 5 (2006) 529-534

9. List of publication

Publications related to my PhD theses:

Journal papers:

[L1**] Z. Fekete**, A. Pongrácz, P. Fürjes, G. Battistig: Improved process flow for buried channel fabrication in silicon, Microsystem Technologies 18 (2012) 353-358, IF: 0.931

[L2] **Z. Fekete**, A. Pongrácz, G. Márton, P. Fürjes: On the fabrication parameters of buried microchannels integrated in in-plane silicon microprobes, Material Science Forum 729 (2012) 210-215

[L3] **Z. Fekete**, P. Nagy, G. Huszka, F. Tolner, A. Pongrácz, P. Fürjes: Performance characterization of micromachined particle separation system based on Zweifach-Fung effect, Sensors & Actuators Chemical B 162 (2012) 89-94, IF: 3.898

Conference papers:

[K1] **Z. Fekete**, A. Pongrácz, Szendrey Á., Fürjes P.: Buried microchannels in silicon with planar surface, 22nd Micromechanics and Micro systems Europe Workshop, Toensberg (2011) Paper ID: A3

[K2] A Pongrácz, **Z Fekete**, G Marton, R Fiáth, P Fürjes, I Ulbert, G Battistig: Deep-brain silicon multielectrodes for simultaneous neural recording and drug delivery, Procedia Engineering, In Press (2012)

[K3] **Z. Fekete**, P. Nagy, A. Pongrácz, I. Bársony, P. Fürjes Efficiency test on the experimental design of micromachined blood separation system based on Zweifach-Fung effect, Procedia Engineering 25 (2011) 1241-1244

[K4] R. E. Gyurcsányi, I. Makra, Gy. Jágerszki, T. Bakk, **Z. Fekete**, G. Battistig, I. Bársony, P. Fürjes: Characterisation of solid-state gold nanopores applicable for biochemical sensing, Procedia Engineering 25 (2011) 904-907

[K5] **Z. Fekete**, G. Huszka, A. Pongrácz, Gy. Jágerszki, R. E. Gyurcsányi, E. Vrouwe, P. Fürjes: Integrated microfluidic environment for solid-state nanopore sensors, Procedia Engineering, In Press (2012)

Patent

[Sz1] **Fekete Z.**, Pongrácz A., Szendrey Á., Fürjes P., Battistig G.: CMOS technológiába integrálható eljárás egykristályos Si alapú, eltemetett mikrofluidikai csatornahálózattal rendelkező eszköz előállítására, a szubsztrát felület planaritásának megőrzése mellett, P1100170

Other publications

Journal papers:

[L4] I. Rajta, S. Z. Szilasi, P. Fürjes, **Z. Fekete**, Cs. Dücső: Si micro-turbine by proton beam writing and porous silicon micromachining, Nuclear Instruments & Methods in Physics Research Section B - Beam interactions with materials and atoms 267:(12-13) pp. 2292-2295. (2009), IF: 1.156

[L5] **Z. Fekete**, B. Sinkovics, I. Rajta, G. A. B. Gál, P. Fürjes: Characterisation of the end-of-range geometric effects in complex 3D silicon micro-components formed by proton beam writing, Journal of Micromechanics and Microengineering 20: 064015 (2010) IF: 2.276

[L6] **Z. Fekete**, P. Fürjes, T. Kárpáti, Gál G.A.B, I. Rajta: MEMS-compatible hard coating technique of moveable 3D silicon microstructures, Materials Science Forum 659: pp. 147-152. (2010)

[L7] E. Holczer, **Z. Fekete**, P. Fürjes: Surface modification of PDMS based microfluidic systems by tensides, Material Science Forum 729 (2013) 361-366

Conference papers:

[K4] I Rajta, Sz Szilasi, P Fürjes, **Z Fekete**, Cs Dücső: Si Micro-turbine by proton beam writing and porous silicon micromachining, Proceedings of 11th International Conference on Nuclear Micropobe Technology and Applications, Debrecen (2008) Paper P-28.

[K5**]** **Z Fekete**, P Fürjes, I Rajta, Cs Dücső: Characterisation of End-of-Range geometric effect in complex 3D silicon micro-components formed by Proton Beam Writing, Proceedings of Micromechanics Europe, Toulouse (2009) Paper 150

[K6] P Fürjes, **Z Fekete**, G Lövey, I Bársony: Thermally actuated valve system for multi-channel microfluidics, Proceedings of Micromechanics Europe, Toulouse (2009) Paper 124

[K7] **Z. Fekete**, D. Gubán, É. Vázsonyi, A. Pongrácz, G. Battistig, P. Fürjes: Development of 3D etching processes and subsequent layer deposition for surface modification of silicon, Proceedings of Micromechanics Europe 2010, Enschede (2010) Paper ID: A05

[K8] F. Dortu, H. Egger, K. Kolari, T. Haatainen, P. Furjes, **Z. Fekete**, D. Bernier, G.Sharp,B. Lahiri, S. Kurunczi, J.-C. Sanchez, N. Turck, P. Petrik, D. Patko, R. Horvath, S. Eiden, T. Aalto, S. Watts, N.P. Johnson, R.M. De La Rue, D. Giannone: Design and process development of a photonic crystal polymer biosensor for point of care diagnostics, Proceedings of the Conference on Clinical and Biomedical Spectroscopy and Imaging II, Prague (2011)

[K9] **Z. Fekete**, E. Holczer, E. Tóth, K. Iván, P. Fürjes: Design and realisation microfluidic stochastic mixers Integrable in bioanalytical systems, 22nd Micromechanics and Micro systems Europe Workshop, Toensberg (2011) Paper ID: D71

[K10] G. Márton, A. Pongrácz, L. Grand, É. Vázsonyi, I. Ulbert, G. Karmos, **Z. Fekete**, G. Battistig: Neural signal recordings with a novel multisite silicon probes, 8th European Biophysics Congress, Budapest (2011) Paper ID: 738

[K11] **Z. Fekete**, E. Holczer, E. Tóth, K. Iván, P. Fürjes: Stochastic mixing in microfluidics integrable in bioanalytical systems, Procedia Engineering 25 (2011) 1229-1232

[K12] P Fürjes, **Z Fekete**, E G Holczer, E Tóth, K Iván, I Bársony: Particle mixing by chaotic advection in polymer based microfluidic systems, Procedia Engineering (2012) In Press

[K13] P Fürjes, **Z Fekete**, L Illés, A L Tóth, G Battistig, R E Gyurcsányi: Effects of the Focused Ion Beam parameters on nanopore milling in solid state membranes, Procedia Engineering (2012) In Press

[K14] P Földesy, **Z Fekete**, T Pardy, D Gergelyi, Terahertz spatial light modulator with digital microfluidic array, Procedia Engineering (2012) In Press

Publication in Hungarian:

[M1] **Fekete Z.:** Szilícium alapú mikrofluidikai elemek fejlesztése protonnyalábos mikromegmunkálással és pórusos szilícium segédréteg felhasználásával, XXIX. OTDK Műszaki Szekció Tanulmányai Miskolc, Magyarország, 2009.04.14. Miskolc: MTA ; Miskolci Egyetem, pp. 28-32

[M2] **Fekete Z.**, Fürjes P.: Szilícium mikroturbina megvalósítása protonsugaras direktírással és pórusos szilícium mikromegmunkálással, Géniusz Európa: Diplomázók Nemzetközi Fóruma Budapest, Magyarország, 2009.09.09-2009.09.13. pp. 1-5. Link: http://inventor.hu/genius7/hudolgozatok/Fekete%20Z%20Genius_dolgozat.pdf

10. Acknowledgement

I would like to express my thanks to all the people whose contribution was indispensable for the completion of the work presented in this thesis.

My supervisor, Dr. Péter Fürjes for overall guiding and support, manuscript reading and corrections.

Dr. István Bársony, and Dr. Gábor Battistig for the encouragement, continuous support, and that they provided good conditions for work.

The cleanroom personnel for their precise work and persistent support during micromachining processes.

Dr. Anita Pongrácz and Gergely Márton for invaluable contribution to the development of neural microprobes in MEMS Lab of Institute for Technical Physics & Material Science.

Dr. István Ulbert for providing facilities and contribution to in vivo experiments in the Institute of Cognitive Neuroscience and Psychology.
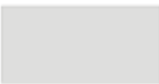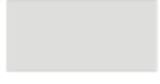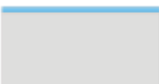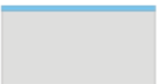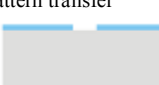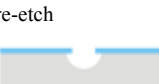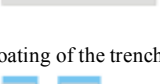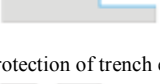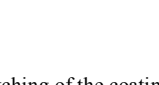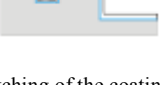
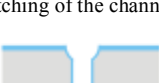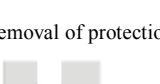Thanks to my parents, sisters, and my best friends for the appreciation, patience and their support during the hard periods.

11. List of acronyms

ARDE – Aspect Ratio Dependant Etching
BHF – Buffered Hydrogen-Fluoride
CMOS – Complementary Metal-Oxide Semiconductor
DBS – Deep Brain Stimulation
DC – Direct Current
DI – de-ionized
DNA - DeoxyriboNucleic Acid
DRIE – Deep Reactive Ion Etching
EDP - Ethylene Diamine Pyrocatechol
EDTA - Ethylene Diamine Tetraacetic Acid
FFT – Fast Fourier Transform
FIB – Focused Ion Beam
HF – Hydrogen-Fluoride
HSA – Human Serum Albumine
IC – Integrated Circuit
ICP – Inductively Coupled Plasma
KOH – Potassium Hydroxide
LPCVD – Low-Pressure Chemical Vapour Deposition
LOC – Lab-on-a-chip
MEMS - Micro-Electro-Mechanical Systems
PDC - Pyrrolidine-DiCarboxylic acid
PE – Purity Efficiency
PMMA - Poly-Methyl-MethAcrylate
PDMS – Poly-dimethylsiloxane
POCT – Point-of-care Testing
PSG - PhosphoSilicate Glass
RBC – Red Blood Cells
RIE – Reactive Ion Etching
SE – Separation Efficiency
SEM – Scanning Electron Microscopy
SOI – Silicon-On-Insulator
TAS – Total Analysis System
TBI - Traumatic Brain Injury
TEM – Transmission Electron Microscopy
WBC – White Blood Cells

12. Appendices

Appendix A

Steps	Original process	Steps	Own planar process
Substrate specification 1.	p or n type silicon resistivity not critical crystal orientation not critical	Substrate specification 1.	p or n type silicon resistivity not critical crystal orientation not critical
Mask material 2.	Thermally grown SiO_2 + Cr	Mask material 2.	Thermally grown SiO_2 (HyOx)
Pattern transfer 3.	Lithography, RIE-CHF_3	Pattern transfer 3.	Lithography, ICP-DRIE C_4F_8+O_2
Pre-etch 4.	1. Under-etch DRIE 2. Isotropic etch 3. Sacrificial layer etch	-	-
DRIE of trench 5.	Cryogenic ICP-DRIE, SF_6 chemistry, AR ~ 25	DRIE of trench 4.	Bosch-process ICP- DRIE, SF_6 chemistry, AR ~ 40
Coating of trench 6.	Thermally grown SiO_2	Coating of the trench 5.	Thermally grown SiO_2 100nm
		Protection of trench edges 6.	Al evaporation 100nm
Etching of the coating at the bottom of the trench 7.	RIE, SF_6 chemistry	Etching of the coating at the bottom of the trench 7.	ICP-DRIE, CHF_3 + Ar
Etching of the channel 8.	RIE, SF_6 chemistry	Etching of the channel 8.	ICP-DRIE, SF_6 chemistry
Stripping coating 9.	SiO_2 etch in HF, BHF	Removal of protection layers 9.	Al and SiO_2 etch in HF, BHF
Filling of the trench 10.	LPCVD, poly-Si or SiN_x	Filling of the trench 10.	LPCVD, poly-Si

Appendix B